

3D-PRINTED HIERARCHICAL RE-ENTRANT HONEYCOMBS: DESIGN, MECHANICAL  
PROPERTIES, AND DEFORMATION MECHANISMS

By

Chi Zhan

A DISSERTATION

Submitted to  
Michigan State University  
in partial fulfillment of the requirements  
for the degree of

Civil Engineering – Doctor of Philosophy

2022

## ABSTRACT

Lightweight materials and structures with extraordinary mechanical properties are desired for automotive, aerospace, and biomedical applications. Conventional lightweight materials such as foams have low density, large deformation and adjustable yield strength, and thus they are widely used in engineering applications. However, the mechanical performance is still far from satisfactory, due to the bending-dominated deformation mechanism determined by the stochastic microstructures.

Inspired by nature, a novel type of lightweight materials, namely the hierarchical re-entrant honeycombs (H-ReHs) has been developed by replacing the traditional cell walls of re-entrant honeycombs by a second-order triangular hierarchy. The H-ReHs comprise fully controllable cellular structures ranging from microscale to macroscale. In addition, the geometry and pattern of the structures are precisely controlled via the emerging additive manufacturing techniques. We hypothesize that the H-ReHs outperform conventional lightweight materials and structures due to the microstructure of the material system, the unique interaction between the structural hierarchies, and the negative Poisson's ratio effect. To test this hypothesis, H-ReHs with different geometric designs and printing materials have been manufactured. The mechanical performance of the H-ReHs has been fully characterized by quasi-static compression tests, dynamic impact tests, and quasi-static oblique tests. To reveal the deformation mechanisms of the H-ReHs, high-speed camera and 3D-digital image correlation have been utilized to analyze the internal strain field of the specimens under various loading conditions.

It has been demonstrated that the 3D-printed H-ReHs exhibit enhanced specific stiffness,

specific initial-buckling strength, structural stability, and specific energy absorption capacity in comparison to regular re-entrant honeycombs (R-ReHs). The H-ReHs exhibit stretching-dominated elastic behavior due to the second-order triangular hierarchy. The post-buckling behavior of the H-ReHs is more stable than the R-ReHs under various strain rates due to the interaction between the first and the second structural hierarchies. These findings provide insights into the design of next-generation lightweight yet mechanically robust materials and structures for future applications and mitigate energy crisis.

Copyright by  
CHI ZHAN  
2022

*Dedicated to my dearest family  
and my beloved wife*

## ACKNOWLEDGMENTS

My time in Michigan State University has been the most joyful, challenging and meaningful period of my life so far. I couldn't come along this unique journey without the support from many individuals that I am fortunate to have. First, I would like to express my deepest gratitude to my advisor, Prof. Weiyi Lu, for the unparalleled support, guidance, patience, and encouragement throughout my four years study at MSU. I am grateful for the training and resources provided by him, especially the constant supports during the COVID-19 pandemic. I am also indebted for his significant efforts in refining my presentations and manuscripts. His innovative conceptualizations, open mindedness, unique perspectives towards challenges, and enthusiasm for the science inspire me to grow and become a better researcher and engineer. I am lucky and truly thankful to have Weiyi as my advisor during my PhD journey.

I would also like to thank my great doctoral committee members I am lucky to have. I would like to thank Prof. Sara Roccabianca, for her valuable suggestions and inspirations on my research, which broaden my perspective and open up more possibility. I would like to thank Prof. Nizar Lajnef, for the constructive advice and questions, which helps me to build the grand picture of my research and expand my horizon on my ways of thinking. I would like to thank Prof. Bei Fan, for her always active and quick replies to my questions, and valuable feedback, comments, and suggestions on my research.

I am sincerely thankful to my colleagues and friends, Dr. Mingzhe Li, Fuming Yang, for helps and teamwork together. Special thanks to Dr. Mingzhe Li, for strict instructions and kind suggestions throughout my PhD study. I want to thank Brian Wright, for the awesome technical

supports on the 3D printing of testing specimens. I want to thank Prof. Shiwang Cheng, and his student, Ruikun Sun and Jie Yang, for the access to rheometers and helps. I would like to thank Prof. Guo Yang and Prof. Patrick Kwon, and their student, Jisheng Chen, Ryan Khawarizmi, and Juan Sandoval for the collaboration and helps. I would like to thank Prof. Wei Zhang and his student Jianzhou He for the training and access to the zetasizer. Besides, I also want to thank my friends, Xing Lu, Mamoon Shaafaey, Jun Guo, Yiyi Chu, Zheng Li, Lijiang Xu, Xuyang Li, Yang Chen, Hao Dong, Huan Zhang, Wenqi Li, thank for the friendship, helps, and joys on my research and life. I also want to thank my collaborators at Ford Motor Company, Dr. Robert McCoy, Linda Zhao, and Ahmad Rezaei Mojdehi, for their helps and supports.

Special thanks to the financial support from Michigan State University (start-up fund, and TSGTD grant), and Ford Motor Company (MSU-Ford Alliance program). I am also grateful for receiving the Engineering Distinguished Fellowship, summer research fellowships, and travel fellowships provided by the College of Engineering, Department of Civil and Environmental Engineering, and the Graduate School of Michigan State University.

Last but not least, I would like to thank my dearest family. To my parents, Guangkuan Zhan and Xiao Zhang, and my grandparents, Guangxin Zhang and Chisheng Zheng, thank you for everything you put to my upbringing, and for your always love, care, encouragement and support. I miss you all. I also owe my deep gratitude to my wife, Jing Zheng, I feel truly lucky to have you by my side, thank you for your unwavering support and always believe in me.

## TABLE OF CONTENTS

<b>LIST OF TABLES.....</b>	<b>x</b>
<b>LIST OF FIGURES .....</b>	<b>xi</b>
<b>CHAPTER 1. MOTIVATION.....</b>	<b>1</b>
<b>CHAPTER 2. INTRODUCTION.....</b>	<b>8</b>
2.1 Background .....	8
2.2 Research Objectives.....	25
2.3 Dissertation Outline .....	26
<b>CHAPTER 3. 3D-PRINTED HIERARCHICAL RE-ENTRANT HONEYCOMB: ENHANCED MECHANICAL PROPERTIES AND THE UNDERLYING DEFORMATION MECHANISMS.....</b>	<b>27</b>
3.1 Introduction.....	27
3.2 Materials and Methods.....	30
3.3 Results and Discussion .....	36
3.4 Conclusions.....	56
<b>CHAPTER 4. ANGLE EFFECT ON THE MECHANICAL PROPERTIES OF 3D- PRINTED HIERARCHICAL RE-ENTRANT HONEYCOMB .....</b>	<b>58</b>
4.1 Introduction.....	58
4.2 Materials and Methods.....	61
4.3 Results and Discussion .....	65
4.4 Conclusions.....	82
<b>CHAPTER 5. STRAIN RATE EFFECT ON THE MECHANICAL PROPERTIES OF 3D- PRINTED HIERARCHICAL RE-ENTRANT HONEYCOMB .....</b>	<b>84</b>
5.1 Introduction.....	85
5.2 Materials and Methods.....	87
5.3 Results and Discussion .....	91
5.4 Conclusion .....	102
<b>CHAPTER 6. OBLIQUE LOADING EFFECT ON THE CRUSHING BEHAVIORS OF HIERARCHICAL RE-ENTRANT HONEYCOMBS MADE WITH SOFT AND RIGID POLYMERS .....</b>	<b>104</b>
6.1 Introduction.....	105
6.2 Materials and Methods.....	107
6.3 Results and Discussion .....	112

6.4	Conclusions.....	127
<b>CHAPTER 7.</b>	<b>CONCLUSIONS AND FUTURE WORK.....</b>	<b>130</b>
7.1	Conclusions.....	130
7.2	Future Work .....	132
<b>BIBLIOGRAPHY</b>	<b>.....</b>	<b>135</b>
<b>APPENDIX</b>	<b>.....</b>	<b>153</b>

## LIST OF TABLES

Table 2.1. A summary of specifications of polymer 3D printing methods. ....	19
Table 3.1. The characteristics of the designed R- and H-ReH samples. ....	32
Table 3.2. The scaling law parameters of relative stiffness and relative initial-buckling strength of ReHs versus relative density. ....	56
Table 4.1. The characteristics of the designed H-ReH and R-ReH samples ( $\rho = 0.34$ ) with different angles. ....	64
Table 4.2. Theoretical and experimental elastic modulus of R-ReH with different angles. ....	74
Table 5.1. Characteristics of designed H-ReH and R-ReH with different relative densities. ....	88
Table 5.2. Dynamic elastic modulus ( $E_d$ ) and strength ( $\sigma_d$ ) of H-ReHs and R-ReHs with various relative densities. ....	93
Table 5.3. Quasi-static elastic modulus ( $E_q$ ) and strength ( $\sigma_q$ ) of H-ReHs and R-ReHs with various relative densities. ....	94
Table 5.4. Dynamic mean crushing stress ( $\sigma_{md}$ ) and quasi-static mean crushing stress ( $\sigma_{mq}$ ) at $\varepsilon = 40\%$ of H-ReHs. ....	97
Table 5.5. Elastic strain rate sensitivity ( $S_e$ ) and post-buckling strain rate sensitivity ( $S_p$ ) of H-ReHs. ....	97
Table 6.1. The characteristics of designed H-ReHs and R-ReHs with different cell-wall angles. ....	108

## LIST OF FIGURES

Figure 1.1. Lightweight materials and structures used in ground and air vehicle body structures [8, 9]. .....	2
Figure 1.2. Conventional lightweight materials with stochastic microstructures (a) Polyurethane foam [22]; (b) Microstructures of polyurethane foam [23]; (c) Aerogel monolith [24]; and (d) Syndiotactic polystyrene aerogel [25]. .....	3
Figure 1.3. Ashby map of strength versus density of the most common materials. (Reprinted from [26] with permission from John Wiley & Sons, Copyright 2018). .....	4
Figure 1.4. Hierarchical materials found in nature. (a) Humerus bone structure of mice (Reprinted from [28] with permission from Oxford University Press, Copyright 2008); (b) Wing structure of Morpho rhetenor butterfly (Reprinted from [29] with permission from Springer Nature, Copyright 2003); (c) Beak structure of hornbill bird (Reprinted from [27] with permission from Annual Reviews, Copyright 2016). .....	5
Figure 1.5. Architectures have been applied to structures to increase the structural efficiency. (a) Primitive wheel [30]; (b) Modern wheel [31]; (c) The pyramids of Giza [32]; (d) Eiffel Tower [33]. .....	6
Figure 2.1. Honeycombs and its various applications. (a) Honeycomb lattice structure. (b) 3D-printed honeycomb in a cross-section of the airplane wing. (c) Honeycomb applied in shoe insole. (d) Honeycomb structured automobile tire [41]. .....	9
Figure 2.2. (a) The scaling relationship between mechanical properties and density illustrating (b) stretching-dominated and (c) bending-dominated behavior exemplified by octet, honeycomb and metal foam. (Reprinted from [27] with permission from Annual Reviews, Copyright 2016). .....	11
Figure 2.3. Hierarchical structures of natural materials. (a) Bone (Reprinted from [49] with permission from Springer Nature, Copyright 2009); (b) Rattan wood (Reprinted from [50] with permission from Royal Society of Chemistry, Copyright 2009); (c) Moss (Sphagnum squarrosum) (Reprinted from [51] with permission from Royal Society, Copyright 2009); (d) Bamboo (Reprinted from [52] with permission from John Wiley & Sons, Copyright 2017); (e) Tendon [53]. .....	12
Figure 2.4. Examples of hierarchical architected materials simultaneously have ultralight, strong, and energy absorbing properties. (a) Hierarchical octahedra lattice (Reprinted from [59] with permission from National Academy of Sciences, Copyright 2015). (b) Ceramic octet-truss nanolattice (Reprinted from [60] with permission from The American Association for the	

Advancement of Science, Copyright 2014). (c) Metallic periodic hollow-tube microlattices (Reprinted from [61] with permission from The American Association for the Advancement of Science, Copyright 2011)..... 14

Figure 2.5. (a) 2D re-entrant honeycomb; (b) 3D re-entrant honeycomb lattice; (c) 3D re-entrant honeycomb unit cell (Reprinted from [96] with permission from Elsevier, Copyright 2015). .... 15

Figure 2.6. Hierarchical structures incorporated in the re-entrant honeycombs. (a) star-shape [104]. (b) Vertex-based (Reprinted from [102] with permission from Elsevier, Copyright 2021). (c) Bidirectional hierarchy (Reprinted from [105] with permission from Elsevier, Copyright 2022). (d) Hexagon and triangle hierarchy (Reprinted from [106] with permission from Elsevier, Copyright 2019). ..... 17

Figure 2.7. FDM 3D printing technology and samples. (a) FDM system [124]. (b) FDM printer (Makerbot replicator 5th generation) in MSU library. (c) FDM printed hierarchical honeycomb using PLA. (d) FDM printed octet using ABS..... 20

Figure 2.8. Material jetting (Polyjet) printing technology and samples. (a) Schematic of material jetting (Polyjet) system [125]. (b) Polyjet printer (Objet Connex350) in Department of ECE in MSU. (c) Polyjet printed advanced Octet lattice and hierarchical re-entrant honeycomb using Rigur (thinnest wall is 0.5 mm) [126]..... 22

Figure 2.9. (a) Aramis V8 3D-DIC system; (b) DIC system coupled with universal test machine during mechanical testing. .... 24

Figure 3.1. Design and configuration of (a) R- and (b) H-ReH representative volume elements. .... 30

Figure 3.2. 3D-printed standardized specimen and ReH samples with different relative densities. (a) Standardized dog bone specimen and cylindrical specimen for uniaxial tensile and compressive tests, respectively. (b-d) R-ReH specimens ( $\rho = 0.22, 0.32, \text{ and } 0.48$ ), and (e-g) H-ReH specimens ( $\rho = 0.23, 0.34, \text{ and } 0.44$ ). The central RVE of each sample (highlighted) represents the DIC field of view..... 32

Figure 3.3. Standardized testing results of the printing material: (a) uniaxial tensile test and (b) uniaxial compressive test. .... 35

Figure 3.4. Mesh sensitivity analyses for (a) R-ReHs and (b) H-ReHs..... 35

Figure 3.5. Quasi-static compressive response of R- and H-ReHs with different relative densities: stress-strain curves. .... 36

Figure 3.6. Quasi-static compressive response of R- and H-ReHs with different relative densities. (a-c) Normalized stress-strain curves of R- and H-ReHs: (a) $\rho = 0.23$ , (b) $\rho = 0.34$ , and (c) $\rho = 0.44$ , (d) Specific stiffness, (e) Specific initial-buckling strength, and (f) Termination strain (D and F represent the termination mode of the ReHs is either densification or fracture).....	38
Figure 3.7. (a) Specific energy absorption and (b) Mean crushing force of R- and H-ReHs. ....	39
Figure 3.8. Experimental images of (a) R-ReH ( $\rho = 0.32$ ) and (b) H-ReH ( $\rho = 0.34$ ) at $\varepsilon = 0.05$ , and (c) Poisson's ratio ( $\nu_{xy}$ ) for corresponding R-ReH and H-ReH.....	41
Figure 3.9. DIC strain fields of R-ReH ( $\rho = 0.32$ ) at $\varepsilon = 0.05$ (a-c) in $0^\circ$ , $60^\circ$ and $-60^\circ$ directions, and H-ReH ( $\rho = 0.34$ ) at $\varepsilon = 0.04$ (d-f) in $0^\circ$ , $60^\circ$ and $-60^\circ$ directions.....	42
Figure 3.10. Deformation patterns of (a) R-ReH ( $\rho = 0.32$ ), (b) R-ReH ( $\rho = 0.48$ ) and (c) H-ReH ( $\rho = 0.23$ ). DIC strain fields of central RVEs of (d) R-ReH ( $\rho = 0.32$ ) and (e) H-ReH ( $\rho = 0.23$ ). .....	44
Figure 3.11. Effect of the slenderness of the 2 <sup>nd</sup> order triangular hierarchy on (a) – (c) the local deformation mechanisms at $\varepsilon = 0.1$ , where $lh/tt = 8.64, 5.54$ , and $4.04$ ; and (d) specific energy absorption of the H-ReHs. ....	46
Figure 3.12. Deformation patterns of (a) R-ReH ( $\rho = 0.22$ ), (b) H-ReH ( $\rho = 0.34$ ) and (c) H-ReH ( $\rho = 0.44$ ).....	48
Figure 3.13. DIC strain fields of H-ReH ( $\rho = 0.23$ ) at $\varepsilon = 0.04$ (a) in $0^\circ$ , and (b) $90^\circ$ , and R-ReH ( $\rho = 0.22$ ) at $\varepsilon = 0.04$ (c) in $0^\circ$ , and (d) $90^\circ$ .....	49
Figure 3.14. DIC strain fields of H-ReH ( $\rho = 0.34$ ) at $\varepsilon = 0.04$ (a) in $0^\circ$ , and (b) $90^\circ$ , and R-ReH ( $\rho = 0.32$ ) at $\varepsilon = 0.04$ (c) in $0^\circ$ , and (d) $90^\circ$ .....	50
Figure 3.15. DIC strain fields of H-ReH ( $\rho = 0.44$ ) at $\varepsilon = 0.04$ (a) in $0^\circ$ , and (b) $90^\circ$ , and R-ReH ( $\rho = 0.48$ ) at $\varepsilon = 0.04$ (c) in $0^\circ$ , and (d) $90^\circ$ .....	51
Figure 3.16. DIC strain fields of R-ReH ( $\rho = 0.32$ ) at $\varepsilon = 0.01$ (a-c) in $0^\circ$ , $+60^\circ$ and $-60^\circ$ directions, and H-ReH ( $\rho = 0.34$ ) at $\varepsilon = 0.01$ (d-f) in $0^\circ$ , $+60^\circ$ and $-60^\circ$ directions.....	52
Figure 3.17. Numerical simulation of R- and H-ReHs. (a) Simulated constitutive behavior compared with experimental results, and simulated deformation patterns of (b) H-ReH, and (c) R-ReH.....	53

Figure 3.18. Simulated deformation patterns of H- and R-ReHs. (a) H-ReH ( $\rho = 0.34$ ), (b) H-ReH ( $\rho = 0.44$ ), (c) R-ReH ( $\rho = 0.32$ ), and (d) R-ReH ( $\rho = 0.48$ ).....	54
Figure 3.19. Scaling laws for ReHs (a) Relative stiffness, and (b) Relative initial-buckling strength.....	56
Figure 4.1. Design and configuration of (a) 45°, (b) 60° and (c) 75° H-ReH and R-ReH ( $\rho = 0.34$ ) representative volume elements. ....	62
Figure 4.2. (a) Constitutive behavior of the Rigur printing material. (b-d) 3D-printed H-ReH and R-ReH samples with different angles: (b) 45°, (c) 60°, and (d) 75°.....	64
Figure 4.3. Quasi-static compressive response of R- and H-ReHs with three different cell-wall angle designs: 75°, 60° and 45°.....	66
Figure 4.4. The negative Poisson's ratio effect of R- and H-ReHs with different cell-wall angles at $\epsilon=0.05$ . (a) Poisson's ratio ( $\nu_{xy}$ ) versus cell-wall angles. Experimental images of ReHs: (b) 45°, (c) 60°, and (d) 75°.....	68
Figure 4.5. Initial elastic behaviors of H-ReHs and R-ReHs with different angles. (a) Elastic modulus, and (b) Strength. DIC strain field in inclined members: (c) alone inclined member axial direction and (d) alone horizontal direction.....	71
Figure 4.6. (a) R-ReH structure under compressive loading, and (b) free body diagram of the inclined member in R-ReH under loading. ....	73
Figure 4.7. Post-buckling behavior of R-ReHs with different angles. (a) stress-strain curves, (b) termination strain, and (c-e) deformation pattern of R-ReHs at various compressive stages: (c) 45°, (d) 60°, and (e) 75°. ....	76
Figure 4.8. Post-buckling behavior of H-ReHs with different angles. (a) stress-strain curves, (b) termination strain, and (c-e) deformation pattern of H-ReHs at various compressive stages: (c) 45°, (d) 60°, and (e) 75°. U means undeformed stage.....	80
Figure 4.9. (a) Specific energy absorption ( $E_s$ ) of R and H-ReHs with different angles. (b) Maximum specific energy absorption ( $E_s^{max}$ ) of R and H-ReHs as a function of the cell-wall angle.....	82
Figure 5.1. Design of H-ReH and R-ReH with different relative densities. (a) $\rho = 0.17$ , (b) $\rho = 0.23$ , and (c) $\rho = 0.34$ .....	88

Figure 5.2. (a) 3D printed H-ReH and R-ReH ( $\rho = 0.23$ ). (b) Schematic of the experimental setup of the drop tower tests.....	90
Figure 5.3. Standardized uniaxial tensile testing result of the printing material. ....	91
Figure 5.4. Typical stress-strain curves of H-ReHs and R-ReHs with different relative densities under (a) dynamic impact, and (b) quasi-static compression. ....	93
Figure 5.5. Comparison of dynamic and quasi-static stress-strain curves of H-ReHs. (a) $\rho = 0.23$ , (b) $\rho = 0.17$ , and (c) $\rho = 0.34$ .....	96
Figure 5.6. The deformation patterns of H-ReH ( $\rho = 0.23$ ). (a) Stress-strain curves, (b) deformation under quasi-static compression, and (c) deformation under dynamic impact.....	99
Figure 5.7. The deformation patterns of R-ReH ( $\rho = 0.23$ ). (a) Stress-strain curves, (b) deformation under quasi-static compression, and (c) deformation under dynamic impact.....	101
Figure 5.8. SEA of H-ReHs and R-ReHs with different relative density under quasi-static and dynamic loading conditions. (Q is denoted for quasi-static condition, and D is denoted for dynamic condition). ....	102
Figure 6.1. Design and configurations of H-ReHs and R-ReHs with $\rho = 0.34$ . (a) 45° H-ReH, (b) 45° R-ReH, (c) 60° H-ReH, and (d) 60° R-ReH.....	108
Figure 6.2. (a-b) 3D printed specimens with soft (black) and rigid (white) polymers: (a) Printed 45° H-ReH and 45° R-ReH with soft and rigid polymers. (b) Printed 60° H-ReH and 60° R-ReH with soft and rigid polymers. Constitutive behavior of the printing materials: (c) soft polymer (FLX4895), and (d) rigid polymer (Rigur). ....	110
Figure 6.3. Setups for oblique compressive loading and axial loading. (a) Oblique loading with angle of 15°, and (b) axial loading with angle of 0°.....	111
Figure 6.4. Load-displacement curves of 45° ReHs under oblique (15°) and axial (0°) loadings. (a) ReHs fabricated by soft materials (b) ReHs fabricated by rigid materials. (O denoted for oblique loading, and A denoted for axial loading). ....	113
Figure 6.5. Load-displacement curves of 60° ReHs under oblique (15°) and axial (0°) loadings. (a) ReHs fabricated by soft materials (b) ReHs fabricated by rigid materials. (O denoted for oblique loading, and A denoted for axial loading). ....	114
Figure 6.6. Poisson's ratio of H-ReHs and R-ReHs with different cell-wall angles and fabricated	

with different materials. (a) ReHs with 45° cell wall angle. (b) ReHs with 60° cell wall angle..... 116

Figure 6.7. Rotation analyses of 45° R-ReH and H-ReH fabricated with soft material. (a) R-ReH and (b) H-ReH at displacement of 2.34 mm. (c) R-ReH and (d) H-ReH at displacement of 4 mm. .... 118

Figure 6.8. Rotation analyses of 45° R-ReH and H-ReH fabricated with rigid material. (a) R-ReH and (b) H-ReH at displacement of 2.34 mm. (c) R-ReH and (d) H-ReH at displacement of 4 mm. .... 118

Figure 6.9. DIC strain fields (major strain) of 45° R-ReH and H-ReH fabricated with soft material. (a) R-ReH and (b) H-ReH at displacement of 2.34 mm. (c) R-ReH and (d) H-ReH at displacement of 4 mm. .... 120

Figure 6.10. DIC strain fields (major strain) of 45° R-ReH and H-ReH fabricated with rigid material. (a) R-ReH and (b) H-ReH at displacement of 2.34 mm. (c) R-ReH and (d) H-ReH at displacement of 4 mm. .... 121

Figure 6.11. Rotation analyses of 60° R-ReH and H-ReH fabricated with soft material. (a) R-ReH and (b) H-ReH at displacement of 3.04 mm. (c) R-ReH and (d) H-ReH at displacement of 6.76 mm. .... 123

Figure 6.12. DIC strain fields (major strain) of 60° R-ReH and H-ReH fabricated with soft material. (a) R-ReH and (b) H-ReH at displacement of 3.04 mm. (c) R-ReH and (d) H-ReH at displacement of 6.76 mm. .... 125

Figure 6.13. Local deformation mechanism of 2<sup>nd</sup> order struts under the oblique loading. (a) Soft 45° H-ReH, and (b) soft 60° H-ReH. .... 125

Figure 6.14. Specific energy absorption of H-ReHs and R-ReHs under oblique and axial loading: (a) soft 45° ReHs, (b) rigid 45° ReHs, (c) soft 60° ReHs, and (d) rigid 60° ReHs. .... 127

Figure 7.1. (a) Design of multi-material H-ReH divided into outer and inner sections for different material assignment. (b) Stress-strain responses of multi-material H-ReH with hard, original, and soft outer section. .... 133

Figure 7.2. (a) Sandwich structure with H-ReH as new core material. (b) H-ReH filled tube as new thin-walled structure. .... 134

Figure A-1. 15° Wedge design for oblique loading tests..... 153

Figure A-2. Long cap design of the 15° wedge for oblique loading tests. ....	154
Figure A-3. Short cap design of the 15° wedge for oblique loading tests. ....	155
Figure A-4. 30° Wedge design for oblique loading tests. ....	156
Figure A-5. Long cap design of the 30° wedge for oblique loading tests. ....	157
Figure A-6. Short cap design of the 30° wedge for oblique loading tests. ....	158

## CHAPTER 1. MOTIVATION

To enhance the motility, lightweighting technologies are essential for the development of automotive and aerospace industries [1, 2]. As shown in Figure 1.1, the lightweight materials and structures have been widely applied in ground and air vehicle components, such as pillars, rails, chassis, and bumper systems. With these lightweight structures, the mass of vehicles is reduced, and thus the energy efficiency is significantly increased. It has been demonstrated that 10% mass reduction results in an improvement of fuel efficiency by 6-8% of ground vehicles [3] and 5-6% of aircrafts [4]. The development and application of lightweight materials and structures are an effective approach to reduce the fuel consumption and greenhouse gas emissions, which adversely contribute to the global warming, environmental pollutions and petroleum shortage [5, 6]. In addition, the lightweighting technologies endow vehicles with improved control, performance, and reduced material costs as well [7]. For the emerging vehicles with alternative energy sources, lightweight technologies are also desired, to improve the driving range.

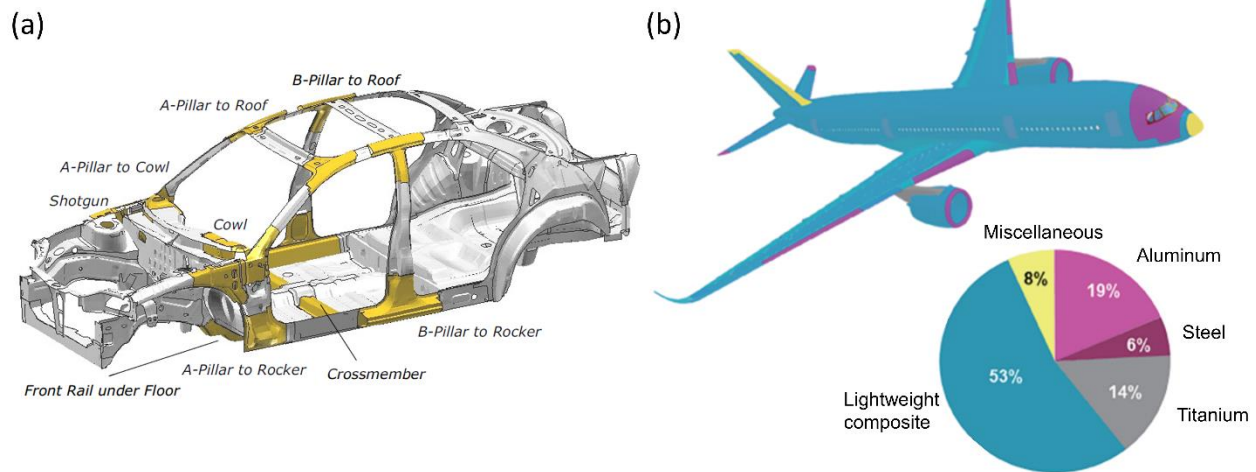


Figure 1.1. Lightweight materials and structures used in ground and air vehicle body structures [8, 9].

Several types of conventional lightweight materials and structures have been manufactured and applied in automotive and aerospace industries and many other engineering practices, such as foams [10-14] and aerogels [15-18], as shown in Figure 1.2. The highly porous microstructures with interconnected network have provided foams and aerogels with unique properties such as low density, extremely low thermal conductivity, excellent mass transfer, etc [19, 20]. However, as shown in the Ashby plot in Figure 1.3, lightweighting leads to the reduction in both absolute and specific strengths of foams. This is due to the stochastic microstructure of foams, so that the material ligaments have an inferior load bearing capacity [21]. One important aspect of automotive design is the occupant’s safety under collision, which is directly determined by the strength and energy absorption capacity of the key components of the vehicle frames. To satisfy the safety needs, ideal lightweight materials exhibiting better mechanical properties at lower densities are desired.

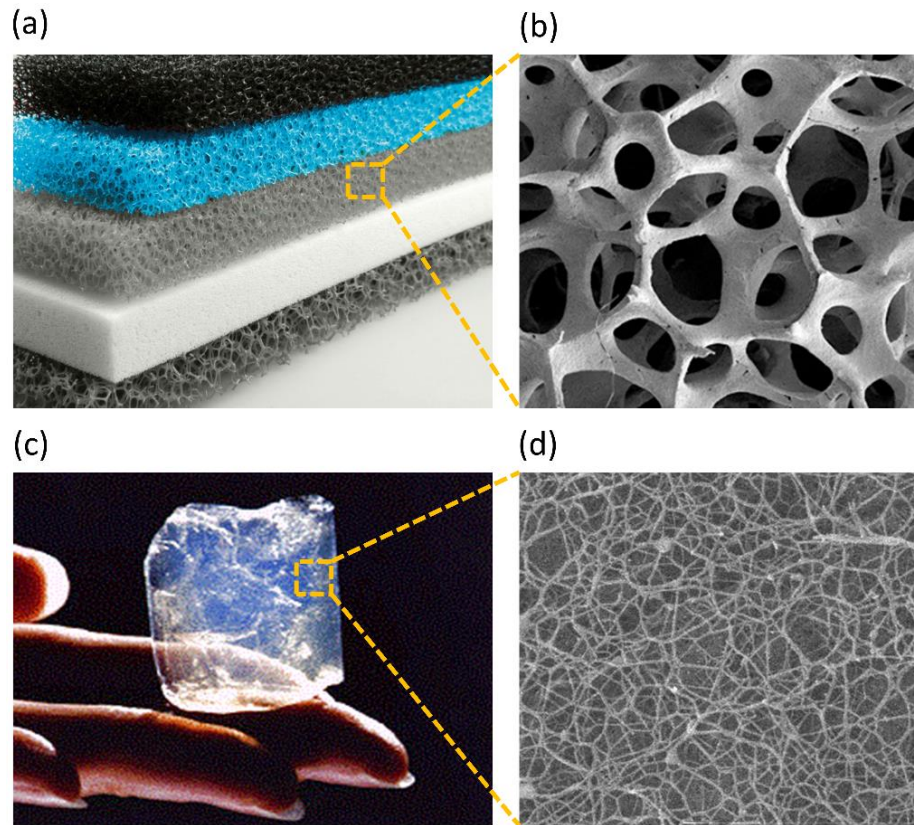


Figure 1.2. Conventional lightweight materials with stochastic microstructures (a) Polyurethane foam [22]; (b) Microstructures of polyurethane foam [23]; (c) Aerogel monolith [24]; and (d) Syndiotactic polystyrene aerogel [25].

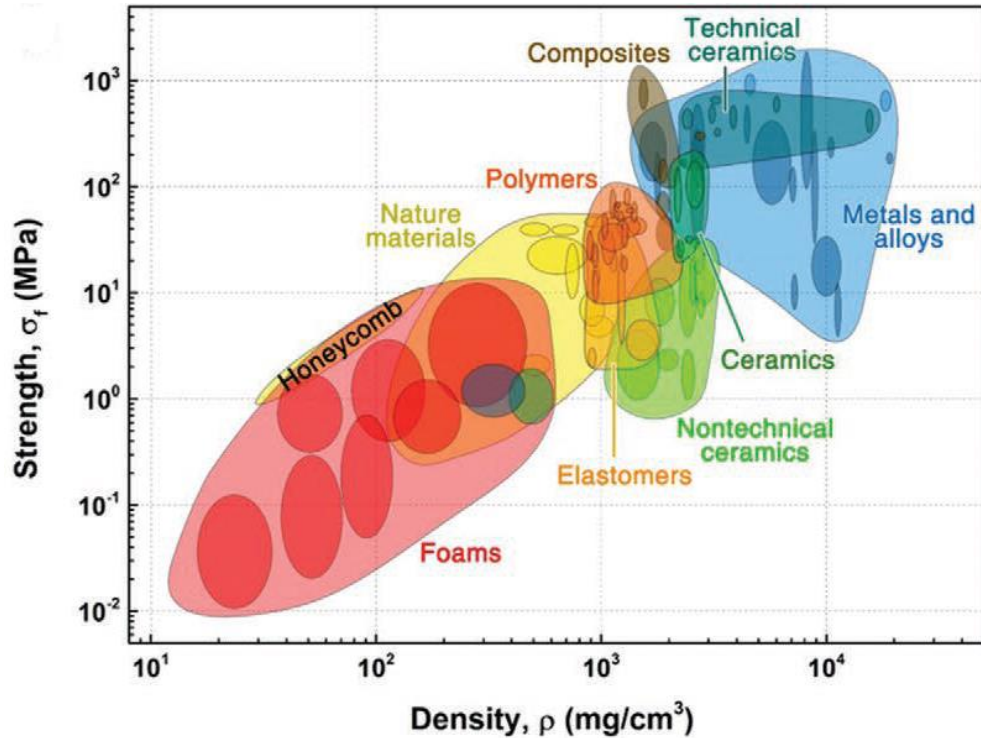


Figure 1.3. Ashby map of strength versus density of the most common materials. (Reprinted from [26] with permission from John Wiley & Sons, Copyright 2018).

Besides the matrix materials, material architectures play significant role on the development novel lightweight materials and structures. Natural architected materials with configured internal geometry exhibit exceptional high stiffness and strength as well as low density [27]. As shown in Figure 1.4, bones have efficient resistance to bending and buckling under various loading conditions and the wings of Morpho rhetenor butterfly have evolved layers of cuticle structure with great robustness for flapping. These superior mechanical properties are originated from the patterned microstructures with complex architectures. In addition, the beak of hornbill bird shown in Figure 1.4 (c) has a unique hierarchical structure, which benefits both the mobility and foraging of the hornbill bird.

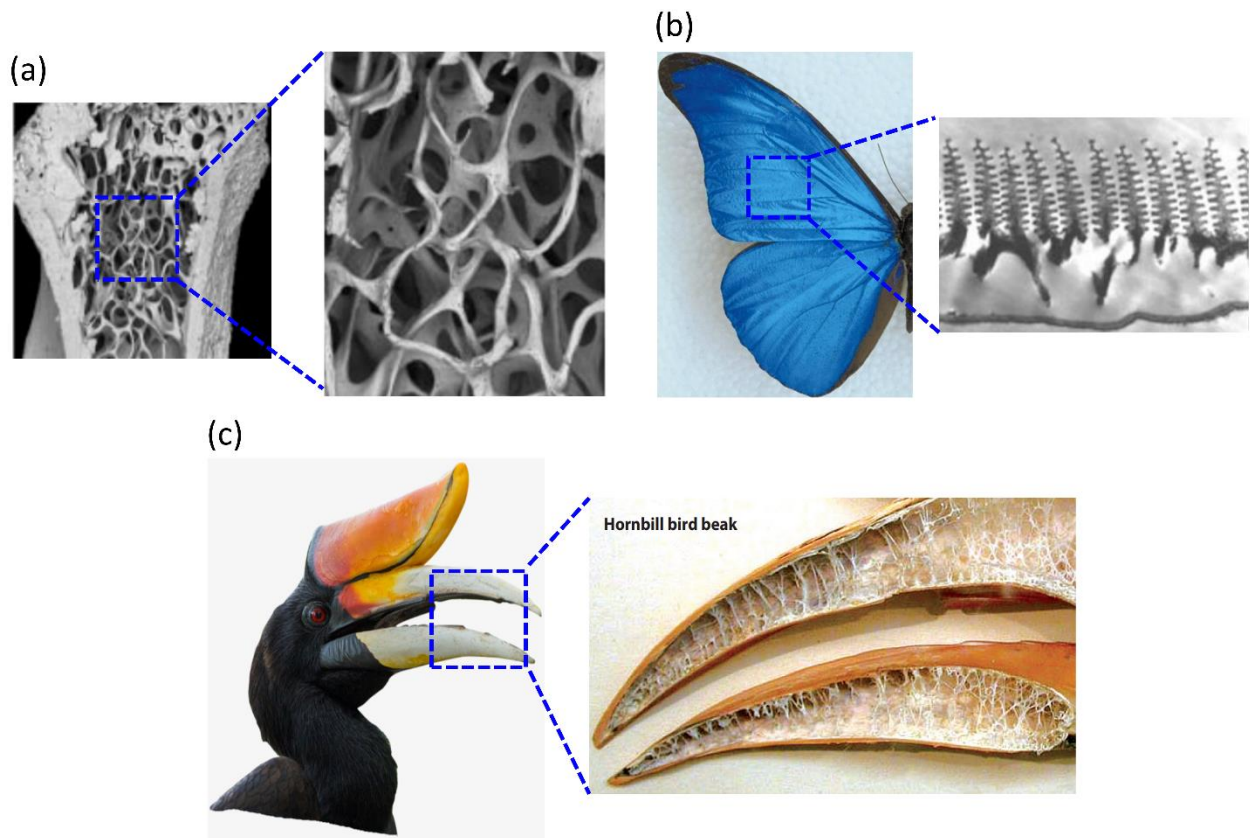


Figure 1.4. Hierarchical materials found in nature. (a) Humerus bone structure of mice (Reprinted from [28] with permission from Oxford University Press, Copyright 2008); (b) Wing structure of *Morpho rhetenor* butterfly (Reprinted from [29] with permission from Springer Nature, Copyright 2003); (c) Beak structure of hornbill bird (Reprinted from [27] with permission from Annual Reviews, Copyright 2016).

Inspired by nature, human have applied architecture design principle in large-scale structures to increase the structural efficiency [27]. As shown in Figure 1.5 (a) and (b), modern wheels constructed of equally spaced spokes have been used to replace primitive wheels at 3500 B.C. made of solid materials, which significantly enhances the mobility and reduce energy consumption of modern vehicles. Similarly in civil engineering, Eiffel Tower has employed advanced

lightweight structural design with great robustness to avoid the use of solid stone blocks for the construction of pyramid back at 2500 B.C (Figure 1.5 (c) and (d)).

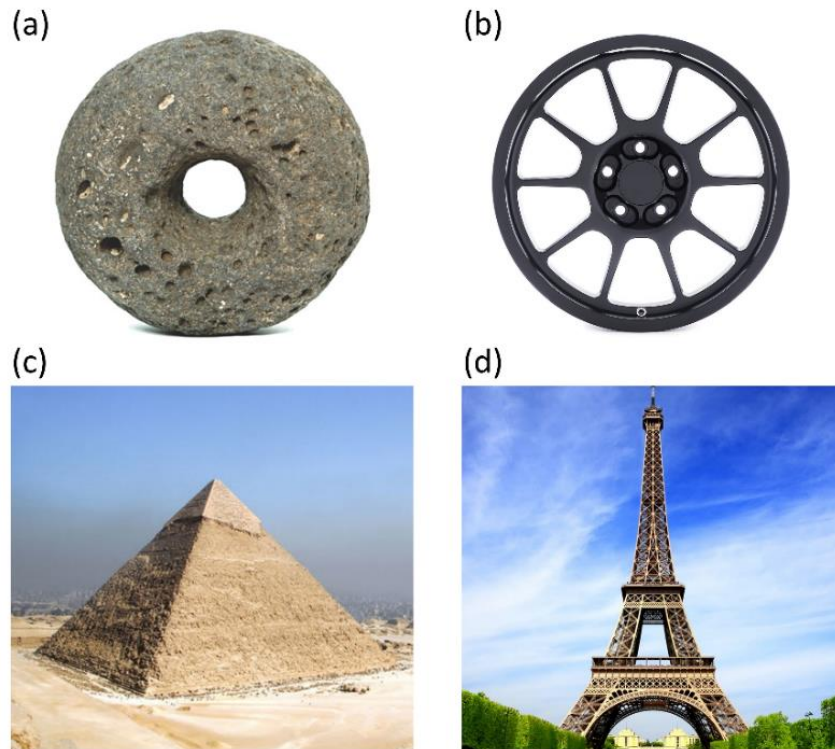


Figure 1.5. Architectures have been applied to structures to increase the structural efficiency. (a) Primitive wheel [30]; (b) Modern wheel [31]; (c) The pyramids of Giza [32]; (d) Eiffel Tower [33].

At smaller scale, similar structural design principle has been adopted to develop novel lightweight materials with superior mechanical efficiency. In the past few years, several lightweight materials with controllable cellular microstructures have been developed. As shown in Figure 1.3, the classical hexagonal honeycombs [34, 35] have much higher strength than the conventional foams. Due to the limitations of conventional fabrication methods, the initial design of architected materials only involves elementary microstructures. Advanced and complex

microstructures have the great potential to further enhance the mechanical properties as well as reduce the weight of architected materials. The recent rapid development in 3D printing technologies, also known as additive manufacturing methods, makes the fabrication of the advanced architected materials with more complex architectures possible.

In this study, we aim to design a new type of lightweight architected materials with unprecedented mechanical properties with the aid of additive manufacturing. The specific architected materials focused of this dissertation is the hierarchical re-entrant honeycombs (H-ReHs), which combine the structural hierarchy and the advanced auxetic configurations. This dissertation focuses on the effects of geometric design, strain rate, and various loading conditions on the mechanical performance and deformation mechanism of the H-ReH. The findings presented herein provide thorough understandings of the structure-property relationship and facilitate future design of lightweight but robust architected materials.

## CHAPTER 2. INTRODUCTION

### 2.1 Background

#### 2.1.1 Architected Materials

Architected materials, an emerging type of lightweight materials, have been developed based on the optimized configuration of solids and voids inside. With tunable and controllable architectures, the mechanical properties are manipulated to achieve ultralow density and high mechanical properties simultaneously. Honeycombs, one specific type of 2D architected materials with great easiness in manufacturing, have been widely used in various applications such as airplanes, vehicles, packaging, and sporting equipment [36], as shown in Figure 2.1. Honeycombs have a regular hexagonal-shape geometry (Figure 2.1 (a)), which not only minimizes the density of the material but also provide outstanding properties such as high energy absorption capacity, low thermal conductivity, excellent acoustic damping capability, and rapidness in manufacturing [34, 37, 38]. This is due to the controllable and tunable cellular structures, including the shape and size of the unit cell, and the aspect ratio and the angle of the cell walls [39, 40].

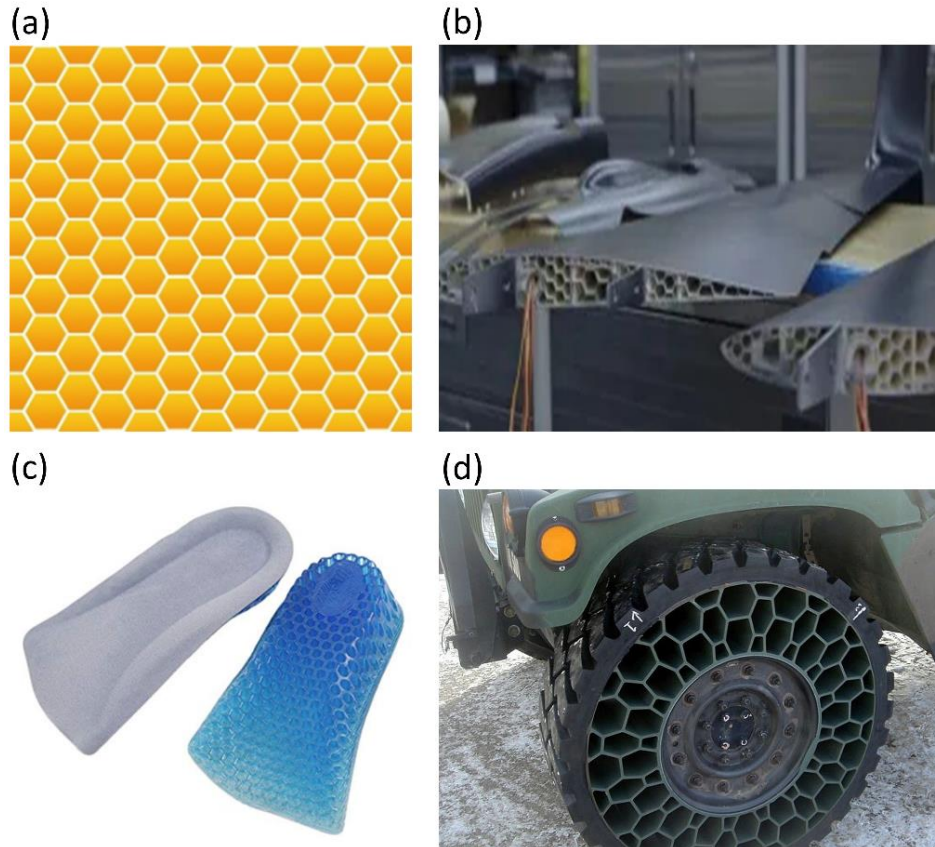


Figure 2.1. Honeycombs and its various applications. (a) Honeycomb lattice structure. (b) 3D-printed honeycomb in a cross-section of the airplane wing. (c) Honeycomb applied in shoe insole. (d) Honeycomb structured automobile tire [41].

It has been demonstrated that the mechanical properties of lightweight materials are correlated with several factors, including (i) relative density, (ii) microstructure and geometry, and (iii) intrinsic material properties. Following the equation derived by Gibson and Ashby [42, 43], the mechanical properties of lightweight materials are predicted as:

$$\frac{\text{mechanical property of the lightweight cellular material}}{\text{mechanical property of the solid material}} = C \left( \frac{\rho}{\rho_s} \right)^n \quad (2.1)$$

where  $C$  and  $n$  are geometric constants, and  $\rho$  and  $\rho_s$  are the density of the lightweight materials and the bulk solid materials, respectively. It is noted that the value of  $n$  can vary from 1 to 4,

corresponds to different deformation modes and a smaller value of  $n$  represents a better performance of the material. As shown in Figure 2.2 (b), for lightweight materials with  $n = 1$ , all members are stretched under loading and the corresponding deformation mode is stretching-dominated. In contrast, for lightweight materials with higher values of  $n$  (Figure 2.2 (c)), the structural members undergo bending or buckling and the corresponding deformation mode is bending-dominated. Foams with random pores and stochastic structures typically has  $n \approx 2$ , due to their inferior bending-dominated deformation mode [42]. Honeycombs with regular hexagonal geometry exhibit improved value of  $n$  (lower than 2) when density is relatively high. However, once reaching the lower density region, honeycombs have much increased value of  $n$ . This is due to the deformation mode shifts from yielding to cell wall buckling [27, 44]. To maintain the stretching-dominated deformation mechanism of honeycombs at lower density, advanced architecture design is needed.

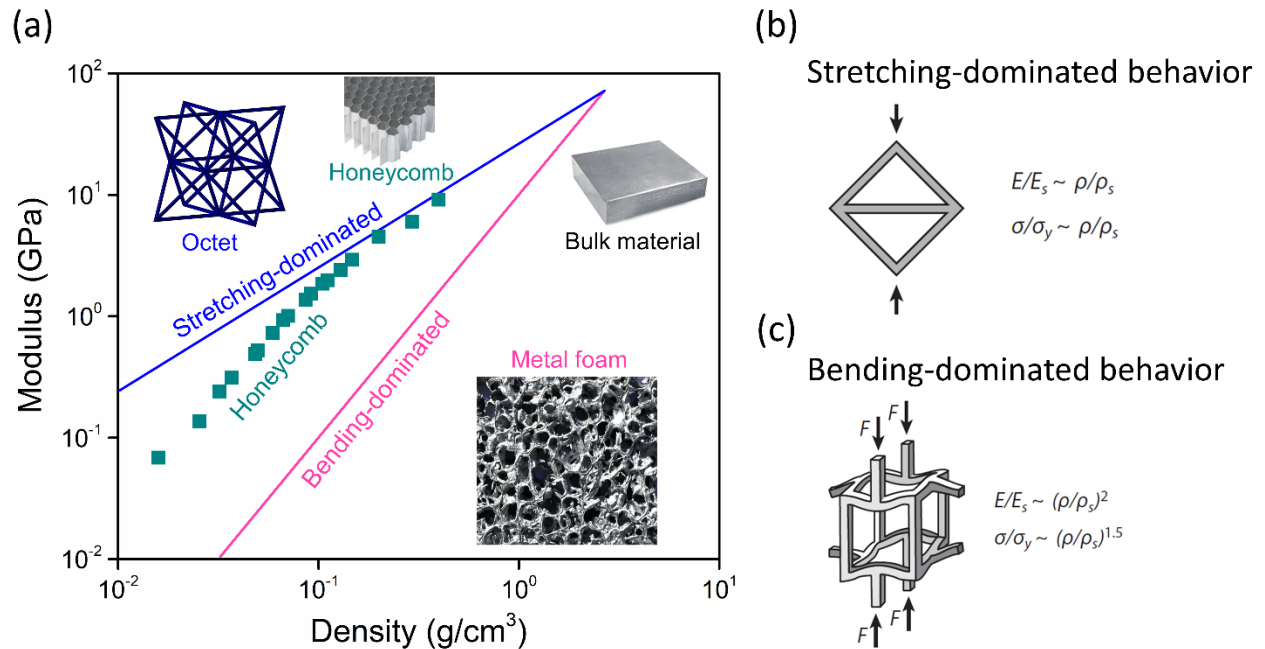


Figure 2.2. (a) The scaling relationship between mechanical properties and density illustrating (b) stretching-dominated and (c) bending-dominated behavior exemplified by octet, honeycomb and metal foam. (Reprinted from [27] with permission from Annual Reviews, Copyright 2016).

### 2.1.2 Hierarchical Architected Materials

Through a long adaptation process during the evolution, natural cellular materials, such as bones, tendons, wood, moss, and bamboo exhibit extremely high stiffness and strength and undergo stretching-dominated deformation [44-48]. This is because of the hierarchical topologies inside (Figure 2.3), which are achieved through refined spatial configuration of solids and voids inside the structure over multiple length scales.

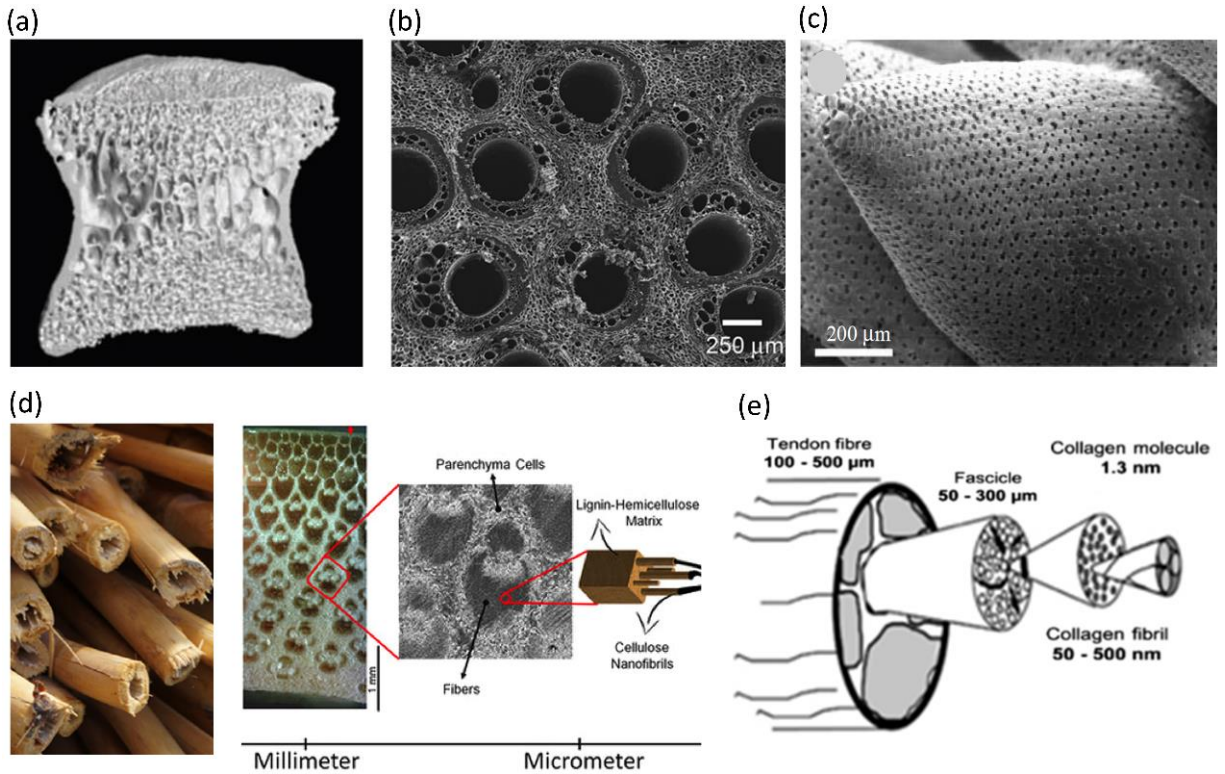


Figure 2.3. Hierarchical structures of natural materials. (a) Bone (Reprinted from [49] with permission from Springer Nature, Copyright 2009); (b) Rattan wood (Reprinted from [50] with permission from Royal Society of Chemistry, Copyright 2009); (c) Moss (*Sphagnum squarrosum*) (Reprinted from [51] with permission from Royal Society, Copyright 2009); (d) Bamboo (Reprinted from [52] with permission from John Wiley & Sons, Copyright 2017); (e) Tendon [53].

Inspired by natural hierarchical materials, hierarchical architected materials have been extensively developed by replacing conventional cell walls of architected materials with structural hierarchy [54-58]. As shown in Figure 2.4, Meza et al. developed hierarchical octahedra lattice with much improved structural strength and stiffness [59]. In addition, they also created recoverable hierarchical octet lattice with ultralight and strong properties based on nanoscale ceramics [60]. Schaedler et al. fabricated ultralight metallic microlattice with structural hierarchy spans from nanometer to millimeter, which exhibits superior recoverability and energy absorption

capacity [61]. These research works have demonstrated effectiveness of structural hierarchy in mechanical enhancement of architected materials. However, as hierarchical architected materials have feature sizes ranging over multiple length scales, the fabrication and manufacturing of these hierarchical architected materials are extremely challenging and limited by high-end processing techniques, such as projection micro-stereolithography, atomic layer deposition (ALD), two-photon lithography (TPL), and oxygen plasma etching. Thanks to the rapid development of 3D printing techniques with improved printing resolution and capability, it is now possible to fabricate hierarchical architected materials with good quality, high efficiency, and less cost.

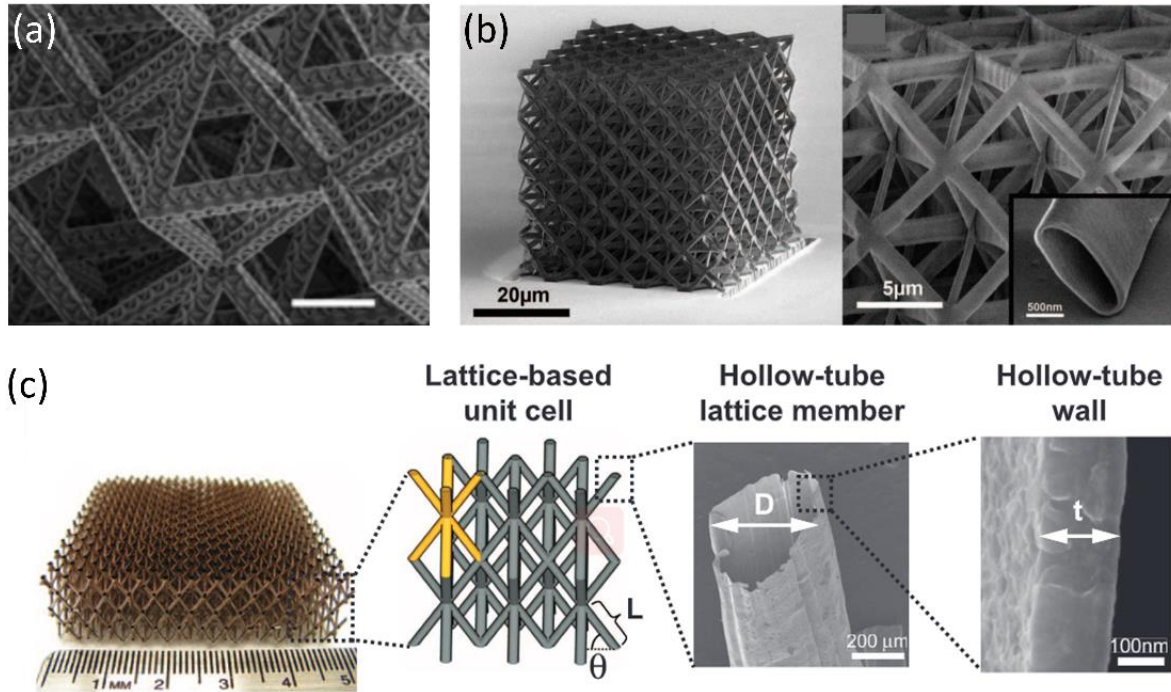


Figure 2.4. Examples of hierarchical architected materials simultaneously have ultralight, strong, and energy absorbing properties. (a) Hierarchical octahedra lattice (Reprinted from [59] with permission from National Academy of Sciences, Copyright 2015). (b) Ceramic octet-truss nanolattice (Reprinted from [60] with permission from The American Association for the Advancement of Science, Copyright 2014). (c) Metallic periodic hollow-tube microlattices (Reprinted from [61] with permission from The American Association for the Advancement of Science, Copyright 2011).

### 2.1.3 Auxetic Materials

The origin of auxetic materials can be traced back to the 1980s, since when a variety of materials have been found to exhibit the unique negative Poisson's ratio (NPR) effect, such as cubic metals [62], zeolites [63], foams [64], ceramics [65], and graphene [66]. This new type of materials contract transversally when undergoing compressive loading, and expand transversally under stretching, contrary to ordinary materials. As the auxetic behavior can potentially endow materials with enhanced mechanical properties, such as energy absorption capacity [67, 68],

indentation resistance [69], fracture toughness [70], and shear modulus [64], there are extensive interests in developing auxetic materials for various potential applications in textile [71-73], automotive [74], aerospace [75], and biomedical engineering [76, 77]. There are several advanced auxetic materials, including star-shaped [78] and V-shaped [79] honeycombs, chiral auxetic materials [80-83], origami and kirigami based materials [84-88], fractal cut metamaterials [89, 90], periodic unimode metamaterials of rigid bars and pivots [91], rotation of rigid hexamers, squares, and triangles [92-94]. Particularly, re-entrant honeycombs with inverted cells [95, 96] (Figure 2.5) have been developed and extensively studied because of their enhanced shear modulus [97, 98], indentation resistance [99], energy absorption [100], and electromagnetic properties [101]. However, the deformation mechanism of the auxetic re-entrant materials is still governed by bending-dominated behavior of ligaments, which results in suboptimal strength and stiffness of the materials compared with the linear scaling properties of bulk materials [21].

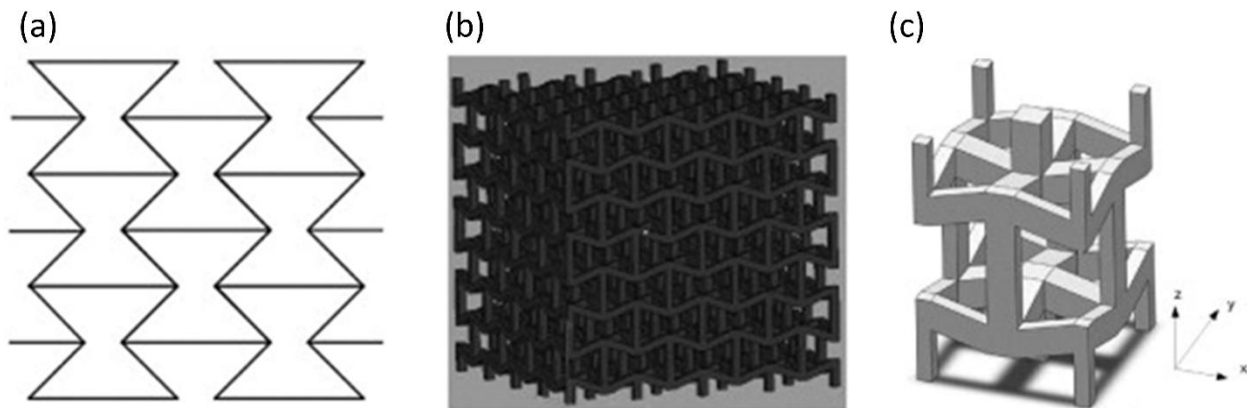


Figure 2.5. (a) 2D re-entrant honeycomb; (b) 3D re-entrant honeycomb lattice; (c) 3D re-entrant honeycomb unit cell (Reprinted from [96] with permission from Elsevier, Copyright 2015).

#### **2.1.4 Combination of Hierarchical and Auxetic Structure**

As both structural hierarchy and auxetic behaviors are effective strategies for the design of lightweight materials and structures, hierarchical auxetic structures have the great potential to possess unprecedented mechanical properties. Until now, only a few studies have attempted to apply hierarchy into the auxetic re-entrant honeycombs, as shown in Figure 2.6. For example, vertex-based hierarchy [102, 103], star shape hierarchy [104], bidirectional hierarchy [105], hexagon hierarchy [106], and triangular hierarchy [106, 107] have been introduced into the re-entrant honeycombs. These studies have preliminarily demonstrated the enhanced performances of H-ReHs. However, a more comprehensive study with further understandings on structure-property relationship of H-ReHs is lacking. In addition, existing studies mostly reside in numerical simulations with very limited experimental validations [103, 106, 108]. This is mainly due to the challenges in fabrication process of H-ReHs. Nevertheless, thanks to the improved capability of advanced 3D printing techniques, H-ReHs are able to be fabricated by seamlessly integrating hierarchical and re-entrant honeycomb topologies together with desirable printing quality. As a result, it is now possible and viable to conduct a systematic investigation of H-ReHs from both experimental and numerical perspectives, aiming to provide thorough understanding of relations between hierarchical design, deformation mechanisms and mechanical responses, to fill the scientific gaps.

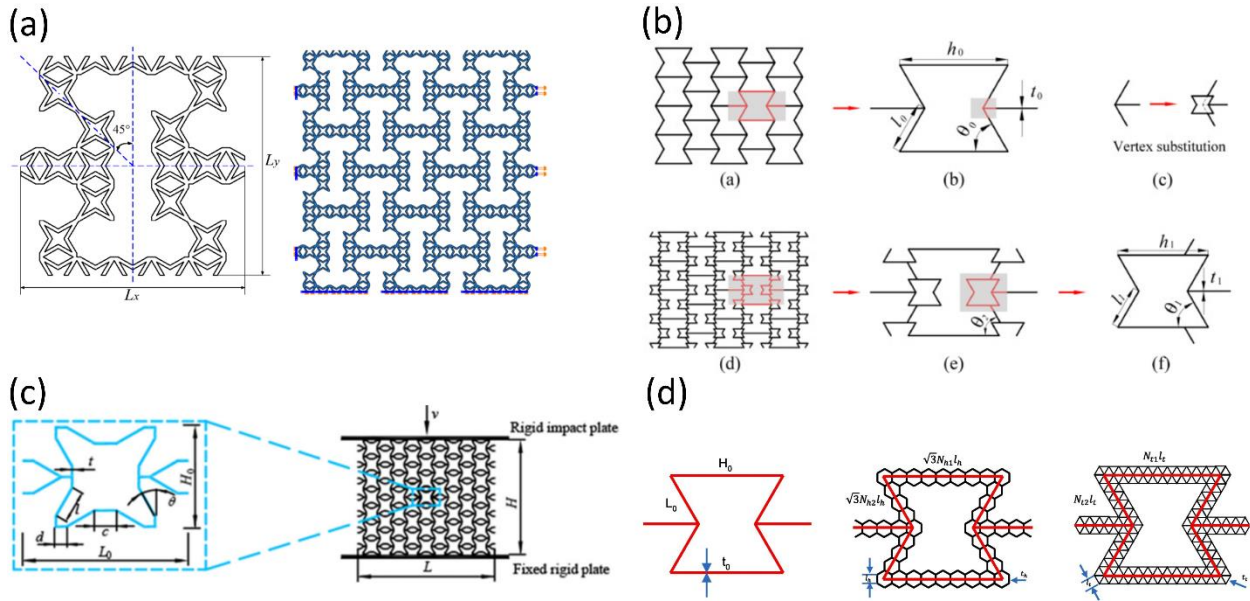


Figure 2.6. Hierarchical structures incorporated in the re-entrant honeycombs. (a) star-shape [104]. (b) Vertex-based (Reprinted from [102] with permission from Elsevier, Copyright 2021). (c) Bidirectional hierarchy (Reprinted from [105] with permission from Elsevier, Copyright 2022). (d) Hexagon and triangle hierarchy (Reprinted from [106] with permission from Elsevier, Copyright 2019).

### 2.1.5 3D Printing Techniques and Comparison

The emerging 3D printing techniques, also known as additive manufacturing, is an efficient and scalable method to fabricate various structures and complex geometries with tunable architectures based on 3D models. The fabrication process of 3D printing involves deposition of printing materials in a successful layers manner. Due to the advantages of rapidness of prototyping, freedom of design, minimization of waste, and mass customization [109], 3D printing technique has been widely applied in industries of prototyping [110, 111], construction [112], and biomedical applications [113, 114]. A wide range of printing materials are available in 3D printing process, such as polymers, metals, ceramics, and concrete [115]. As the 3D printing method is able to

precisely engineer the microstructure of the materials, it can improve and even create new properties of the materials. For example, Chen et al. fabricated hierarchical honeycombs using commercial 3D printers with size features from micrometer to centimeter, which exhibit improved energy absorption capacity and shape integrity [116]. Peng et al. utilized an ink-based 3D printing method to fabricate ultralight biomimetic hierarchical graphene material, which exhibited exceptionally high stiffness and resilience [117].

As the proposed H-ReHs are composed of triangular hierarchy from micrometer level to centimeter level, the resolution and printing properties of the 3D printing techniques are critical to the mechanical performance of the resulted structures. It is necessary to compare different 3D printing techniques in details to select the appropriate 3D printing technique for the fabrication of H-ReHs.

Among various printing materials available in 3D printing, polymers have advantages of less build time, cost, and post-processing [118]. In addition, there are many types of polymers available for 3D printing, such as polylactic acid (PLA), acrylonitrile butadiene styrene (ABS), polyethylene terephthalate (PET), and hybrid polymer materials, which provide customized material properties. Commonly used polymer 3D printing methods include fused deposition modelling (FDM), selective laser sintering (SLS), stereolithography (SLA), and material jetting (Polyjet). Each of them has specific advantages and disadvantages. For comparison, details of different polymer 3D printing characteristics are summarized in Table 2.1. Since the FDM and Polyjet 3D printing facilities are available at Michigan State University and used for prototyping in this study, these two methods are introduced and compared elaborately, as follows.

Table 2.1. A summary of specifications of polymer 3D printing methods.

	Polymer Type	Material Form	Resolution	Printing Order	Advantages	Disadvantages	References
FDM	Thermoplastic	Filament	50-200 $\mu\text{m}$	Point by point	1. Inexpensive 2. Multi-material printing	1. Limited resolution 2. Poor surface quality	[118-120]
SLS	Thermoplastic	Powder	80-250 $\mu\text{m}$	Point by point	1. High accuracy 2. Fine details 3. Powder is recyclable	1. Expensive 2. Slow	[118-120]
SLA	Thermoset	Resin	10 $\mu\text{m}$	Point by point	1. Fast printing 2. Fine resolution and high quality	1. High cost 2. Slow	[118, 119]
Material Jetting	Thermoset	Resin	16 $\mu\text{m}$	Area by area	1. Multi-material printing 2. High surface quality 3. Fine resolution	1. Liquid form materials only 2. Limited viscosity range	[121-123]

FDM is the most common polymer 3D printing method. In FDM method, thermoplastic polymer filament is used, which is heated at the nozzle of the printer to reach a flow state, and then deposited layer by layer on the platform (Figure 2.7 (a)). Afterwards, the fused filaments solidify by cooling down to room temperature. The FDM is compatible with various polymers, such as ABS and PLA. The main benefits of FDM include high speed, low cost, and simplicity of the process. However, FDM also has several drawbacks, including weak mechanical properties, poor resolution, poor surface quality of fused boundary (as shown Figure 2.7 (c-d)), and limited thermoplastic materials.

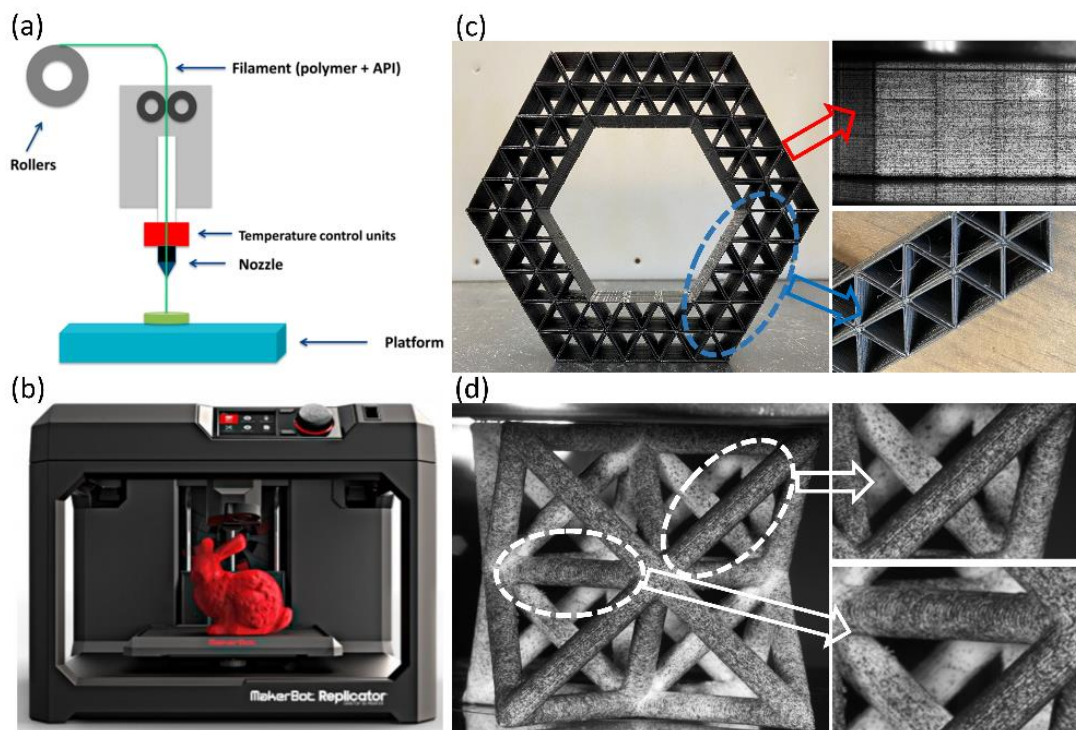


Figure 2.7. FDM 3D printing technology and samples. (a) FDM system [124]. (b) FDM printer (Makerbot replicator 5th generation) in MSU library. (c) FDM printed hierarchical honeycomb using PLA. (d) FDM printed octet using ABS.

Material jetting (Polyjet) method is developed by combining the Inkjet technology and the use of photopolymers. Unlike the inkjet used in conventional printers by jetting onto papers, the liquid photopolymers ink is jet on the platform and then undergoes hardening when expose to UV lights. Therefore, material jetting method is achieved by jetting layers of curable liquid photopolymer onto a build tray firstly, and then instantly cured using UV lights (Figure 2.8). Moreover, multi-material and multi-color options are possible as the printer head has several nozzles, which is capable of simultaneously spraying various materials. When printing small-scale complex geometries, the printer also jets removable supporting material to ensure the printing quality. The supporting material is usually removed by water or solution bath. There are wide choices of materials for material jetting method, including rigid plastic, soft rubber like material, resins, and high temperature polymer materials. In comparison to the FDM method, the Polyjet method has several advantages, such as excellent printing resolution (up to 0.016 mm), good surface quality (no layer-by-layer appearance when using FDM method), and the capability of printing multi-material and multi-color in same parts. Therefore, Polyjet printing method is selected for this study, and all specimens are printed by Polyjet Objet Connex350 3D printer (Stratasys), as shown in Figure 2.8 (b).

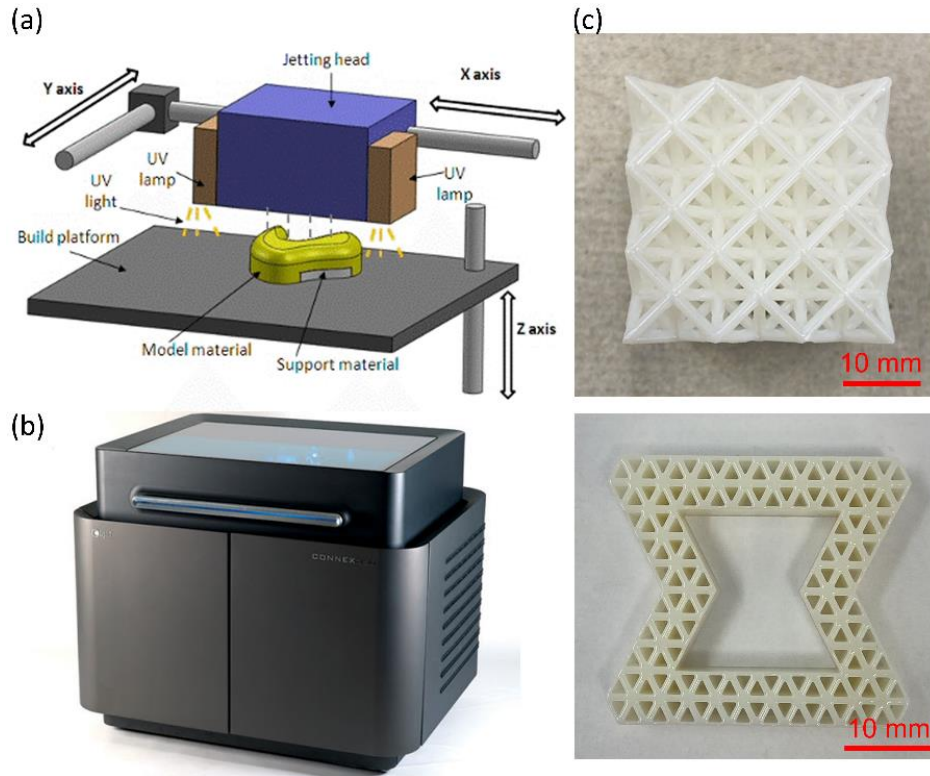


Figure 2.8. Material jetting (Polyjet) printing technology and samples. (a) Schematic of material jetting (Polyjet) system [125]. (b) Polyjet printer (Objet Connex350) in Department of ECE in MSU. (c) Polyjet printed advanced Octet lattice and hierarchical re-entrant honeycomb using Rigur (thinnest wall is 0.5 mm) [126].

### 2.1.6 Digital Image Correlation (DIC)

The digital image correlation (DIC) is a powerful and practical non-contact optical technique for the full-field deformation measurement, which has been widely used in the field of experimental mechanics [127]. The DIC is based on digital image processing and numerical computation. The working of DIC involves comparing the digital images of a test sample at different stages of deformation [128]. To be more specific, firstly a square subset with pixels is selected from the reference image. Afterwards, the deformed subset is tracked from the deformed image through predefined criterion and optimization algorithm. In order for DIC to work

effectively, the square subset must have random and unique pixels with a range of contrast and intensity levels, which requires the test sample surface to be covered with natural or artificial speckle pattern. The speckle pattern creates random gray level intensity variation on the sample surface [129]. During the deformation of the sample, the speckle pattern deforms together with the sample surface, providing reliable surface deformation information. The images for DIC can be obtained from variety of sources at various length scale, such as consumer digital cameras, high-speed cameras, macroscopes and microscopes including scanning electron microscopes (SEM) and atomic force microscopes (AFM) [128]. An Aramis V8 3D-DIC system (shown in Figure 2.9) and GOM correlate professional software have been coupled with the mechanical testing of specimens in this study. This powerful 3D-DIC has high resolution of 4096 x 3000 pixels, frame rate of 25 fps (up to 100 fps), variable measuring area from 20 x 15 mm<sup>2</sup> up to 5000 x 4000 mm<sup>2</sup>, and flexible dual LED lighting, which allows the DIC measurement on multiple length scales at various scenarios.

(a)



(b)

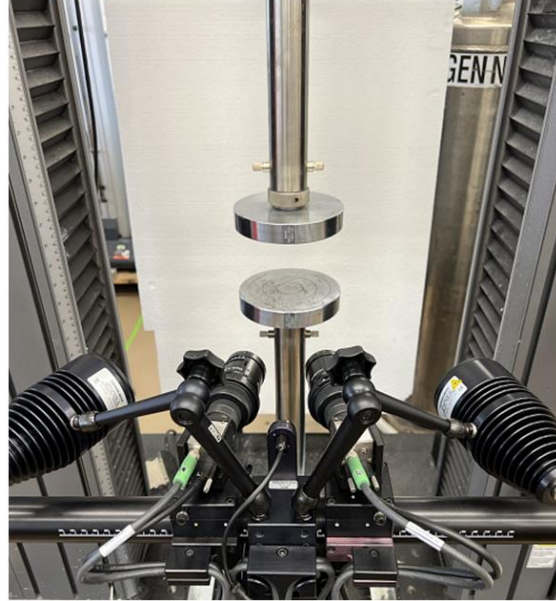


Figure 2.9. (a) Aramis V8 3D-DIC system; (b) DIC system coupled with universal test machine during mechanical testing.

## **2.2 Research Objectives**

The design of advanced lightweight structures relies on the fundamental understanding on the mechanical performance, and deformation mechanisms, which is still lacking. To fill this scientific gap, this dissertation aims to understand the relationship between geometric design, mechanical properties and the unique deformation mechanisms of H-ReHs under complex loading conditions. To this end, multiscale and multi-material H-ReH specimens have been fabricated through polymer-based high-resolution Polyjet 3D printing technique. The mechanical performance of the H-ReHs has been fully characterized by quasi-static compression tests, dynamic impact tests, and quasi-static oblique tests. To reveal the deformation mechanisms of the H-ReHs, high-speed camera and 3D-DIC have been utilized to analyze the internal strain field of the specimens under various loading conditions. The findings of this research shed light on the design of next generation ultralight but robust materials and structures.

### **2.3 Dissertation Outline**

The structure of the dissertation is as follows. Chapter 1 introduces the motivation of this research. Chapter 2 gives a comprehensive overview of existing lightweight materials and structures, including architected materials, hierarchical materials, and auxetic materials, and the detailed comparison of the current 3D printing techniques. Chapter 3 presents a strategic design of H-ReHs with 2<sup>nd</sup> order triangular hierarchy that exhibit superior mechanical properties under the quasi-static compression. The experimental results and the 3D-DIC analysis reveal the novel deformation mechanisms underpinning the superior mechanical properties of the H-ReHs. Chapter 4 elaborates the effect of cell-wall angle on the mechanical performance of H-ReHs. The research outcomes will guide the optimization of the geometric design and tunable mechanical performance of the H-ReHs. Chapter 5 investigates the crushing behavior of H-ReHs under the dynamic impact loading condition, which provides insights of the mechanical performance of the H-ReHs under the intermediate strain rates. Chapter 6 studies the mechanical behavior of H-ReHs under the quasi-static oblique loading conditions, so as to understand the governing deformation mechanism of H-ReHs under complex loading conditions. Chapter 7 summarizes the major findings of the dissertation and discusses the future directions of the research.

## **CHAPTER 3. 3D-PRINTED HIERARCHICAL RE-ENTRANT HONEYCOMB: ENHANCED MECHANICAL PROPERTIES AND THE UNDERLYING DEFORMATION MECHANISMS**

Re-entrant honeycombs are one type of lightweight cellular materials with superior energy absorption and impact resistance. Yet, the mechanical properties of re-entrant honeycombs need to be further improved due to its bending-dominated deformation mechanism. In this chapter, we design a novel stretching-dominated re-entrant honeycomb by combining the structural hierarchy and auxetic cellular configurations. Such hierarchical re-entrant honeycomb (H-ReH) is manufactured through fine-resolution 3D printing technique. The mechanical behavior and deformation mechanism of the designed H-ReH has been investigated through combined digital image correlation (DIC) and finite element simulation. The 3D-printed H-ReHs exhibit enhanced specific stiffness, specific initial-buckling strength, structural stability and specific energy absorption capacity due to the uniquely combined deformation mechanisms. A competition between the 1<sup>st</sup> order and the 2<sup>nd</sup> order hierarchy has been revealed, which governs the mechanical properties of the H-ReHs. These findings provide thorough understandings and facilitate future design of lightweight but robust cellular materials.

### **3.1 Introduction**

Over the past decades, enormous efforts have been invested in developing light-weight materials and structures with enhanced mechanical properties. These materials and structures can be applied not only as new core materials in sandwich panels [130, 131], thin-walled shell

structures [132, 133], and two-phase composites [134], but also has great potential for emerging applications such as soft robotics [135], soft electronics [136], shape morphing deployable materials [137], coronary stents [138], biomedical scaffolds [139], metamaterials [140], actuators and sensors [141], and microelectromechanical system (MEMS) [142, 143], so as to satisfy tremendous demand from rapid-advancing automotive [144], aerospace [145], defense [146], biomedical engineering [147] and energy related industries [148]. Specifically, honeycombs are of particular interests because of the combined lightweight nature, high energy absorption capacity, low thermal conductivity, excellent acoustic damping capability, and rapidness in manufacturing [27, 34, 38, 149, 150]. The superior mechanical performance of honeycombs in comparison to stochastic foams comes from the controllable cellular structures, including the shape and size of the unit cell [39, 40] and the aspect ratio and the angle of the cell walls [37]. In addition, the mechanical performance of honeycomb structures has been further improved by introducing auxetic cellular configurations, such as re-entrant, star-shape, and chiral unit cells [98-100, 105, 151-157]. However, the deformation mechanism of the auxetic honeycomb structures is still governed by bending-dominated behavior, similar to that of stochastic foams [42, 96]. It has been demonstrated that the bending-dominated cellular structures exhibit lower stiffness and strength than stretching-dominated ones, due to bending induced collapse of cell walls and lack of lateral constraints [21].

Inspired by natural cellular materials such as wood, bone and coral, hierarchical cellular structures have extremely high stiffness and strength and undergo stretching deformation [44-48, 59, 158]. The hierarchical topologies have been achieved through refining spatial configuration of

solids and voids inside the structure at multiple length scales. The manufacturing of hierarchical cellular structures is achieved but also limited by high-end processing techniques, such as projection micro-stereolithography, two-photon lithography (TPL), atomic layer deposition (ALD), and oxygen plasma etching. Nevertheless, the emerging additive manufacturing techniques enable the new design and efficient fabrication of the complex hierarchical cellular structures. By replacing conventional cell walls with structural hierarchy, hierarchical honeycombs have shown enhanced stiffness, energy dissipation and shape integrity, due to the stretching-dominated deformation mechanism [116, 159-166].

To this end, we introduce triangular hierarchy into the regular cell walls of re-entrant honeycombs. Previous studies mainly numerical simulations and analytical analyses have demonstrated the feasibility of incorporating hierarchical topology to improve the mechanical properties of the re-entrant honeycombs [102, 103, 106, 108, 167]. However, the underlying deformation mechanism and the dominated interaction between different order of hierarchies, are still elusive. In addition, experimental validation of the models is missing. In this study, through a combined experimental and numerical approach, we aim to improve the mechanical properties of the resulted structures by combining the advantages of structural hierarchy and the negative Poisson's ratio effect, and to reveal the deformation mechanisms and hierarchical interactions governing the mechanical properties of the hierarchical re-entrant honeycombs (H-ReH).

## 3.2 Materials and Methods

### 3.2.1 Design of H-ReHs

The configurations of both regular R- and H-ReH representative volume elements (RVE) are shown in Figure 3.1. The geometry of the R-ReH RVE was determined by three key geometric parameters, i.e. the width of the top horizontal member ( $W$ ), the length of tilted members ( $L$ ), and the member thickness ( $t$ ), as shown in Figure 3.1 (a). The 2<sup>nd</sup> order structural hierarchy in the H-ReH RVE were specified by the thickness ( $t_t$ ) and the length ( $l_t$ ) of the triangular cell wall, as shown in Figure 3.1 (b). For all H-ReHs with different slenderness triangular hierarchy, the length of 2<sup>nd</sup>-order structural hierarchy ( $l_h$ ) is constant. For both R- and H-ReHs, the angle between horizontal and inclined members was set as 60°. To keep the volume of the RVEs a constant, two stacks of the 2<sup>nd</sup> order triangular units with same length were used in the H-ReHs to replace the solid struts in the R-ReHs.

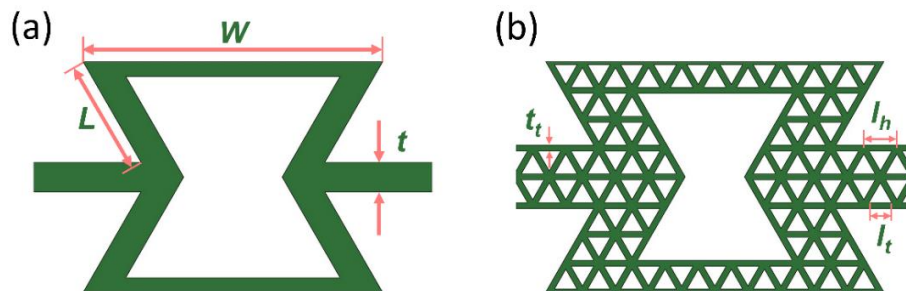


Figure 3.1. Design and configuration of (a) R- and (b) H-ReH representative volume elements.

### 3.2.2 Materials and Sample Preparation

All ReH samples were manufactured using a Polyjet 3D printer (Object Connex350, Stratasys,

Ltd.). Rigur (RGD450, Stratasys, Ltd.), an engineered polypropylene-like material, was used as the printing material. To achieve best printing resolution and shape integrity, a gel-like support material (SUP705, Stratasys, Ltd.) was used. Upon completion of the printing process, the support material was carefully and completely removed by mild waterjet. As shown in Figure 3.2, typical ReH samples were composed of  $2 \times 3$  RVEs with the overall size of  $106 \text{ mm} \times 92 \text{ mm} \times 40 \text{ mm}$  (width  $\times$  height  $\times$  thickness). The samples were thick enough to avoid out of plane buckling under quasi-static compressive tests. The details of the fabricated ReH samples were summarized in Table 3.1. The relative density of various ReH specimens,  $\bar{\rho}$ , was adjusted by the key geometric parameters by following Eqs. (3.1) and (3.2), respectively.

$$\bar{\rho}_{R-ReH} = \frac{(4\sqrt{3}L+2\sqrt{3}W-5t)t}{(2\sqrt{3}W-\sqrt{3}L-5t)(\sqrt{3}L+t)} \quad (3.1)$$

$$\bar{\rho}_{H-ReH} = \frac{38\sqrt{3}t_t^2+69l_t t_t}{18(\sqrt{3}l_t^2+6l_t t_t+3\sqrt{3}t_t^2)} \quad (3.2)$$

For each relative density, at least 3 samples were prepared and tested. After printing, all samples were kept at room temperature for nine days to allow fully cure of the printing material. In addition, three standardized dog bone specimens (ASTM D638-14) and cylindrical specimens (ASTM D695-15) were printed and cured at the same conditions for the characterization of the mechanical properties of the printing material.

Table 3.1. The characteristics of the designed R- and H-ReH samples.

	$\bar{\rho}$	$W$ (mm)	$L$ (mm)	$t$ (mm)		$\bar{\rho}$	$t_i$ (mm)	$l_i$ (mm)
R-ReH	0.48	42.660	13.950	6.391	H-ReH	0.44	1.091	2.520
	0.32	39.826	15.390	3.934		0.34	0.796	3.034
	0.22	38.381	16.115	2.679		0.23	0.511	3.528

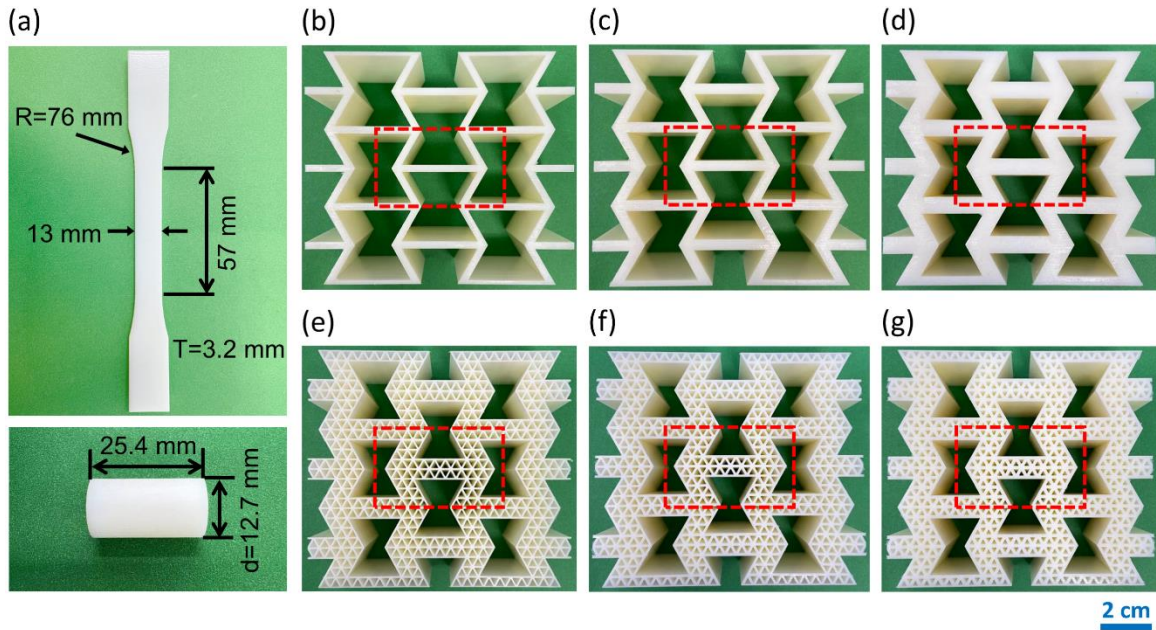


Figure 3.2. 3D-printed standardized specimen and ReH samples with different relative densities. (a) Standardized dog bone specimen and cylindrical specimen for uniaxial tensile and compressive tests, respectively. (b-d) R-ReH specimens ( $\bar{\rho} = 0.22, 0.32, \text{ and } 0.48$ ), and (e-g) H-ReH specimens ( $\bar{\rho} = 0.23, 0.34, \text{ and } 0.44$ ). The central RVE of each sample (highlighted) represents the DIC field of view.

### 3.2.3 Mechanical Testing Coupled with 3D-DIC

The mechanical properties of the Rigur material and the 3D-printed ReHs were measured by a universal testing machine (Model 5982, Instron, Corp.) by uniaxial tensile tests (ASTM D638-14) and quasi-static compressive tests (compression speed of 9 mm/min), respectively. The

Young's modulus and initial-buckling strength of the printing material were determined from the measured stress-strain curve. For ReH samples, the obtained load-displacement curves were converted into stress-strain curves. The stress and strain were calculated as  $\sigma = F / A$  and  $\varepsilon = \delta / h \times 100 \%$ , respectively, where  $F$  was the force applied by the Instron machine,  $A$  was the cross-sectional area of the sample,  $\delta$  was the displacement of Instron machine crosshead, and  $h$  was the initial height of the sample. In order to evaluate the excellence of the ReHs, the stress was further normalized by the density of the sample as

$$\sigma_n = \sigma / \rho \quad (3.3)$$

The uniaxial compressive tests were coupled with a 3D-DIC instrument (Aramis V8, Trilion Quality Systems, LLC) to measure the strain field evolution. All samples were spray painted of 3-7 pixel-sized black dots with 50% coverage to create patterns for DIC tracking. High-resolution deformation contours of the central RVE of each ReH sample was tracked and analyzed, as illustrated in Figure 3.2. Videos were captured at a rate of 1 fps and the strain fields and the deformation contours of ReH samples were computed by the GOM correlate professional software.

### 3.2.4 Finite Element Analysis

Finite element (FE) analysis of the H- and R-ReHs under uniaxial compression were performed using Abaqus/CAE 2020. The material properties of the printing material are critical input for the FE models. As the properties are determined by the processing method, it is necessary to characterize the 3D-printed specimens under the same printing condition of the ReHs. By following the ASTM D638-14 and ASTM D695-15 standards, the constitutive tensile and

compressive behaviors of the printing material were measured and shown in Figure 3.3 (a) and (b), respectively. The initial linear portion of the stress-strain curves were used to determine the modulus, and the stresses at the end of the linear-elastic range were used to determine the strength. From the tensile test, the measured Young's modulus  $E_R$  and the tensile strength  $\sigma_R$  were 734.1 MPa and 43 MPa, respectively. In compression, the values were slightly changed to 749.3 MPa and 44 MPa. The density,  $\rho_R = 1200 \text{ kg/m}^3$ , and Poisson's ratio,  $\nu_R = 0.3$ , of the printing material are obtained directly from manufacture datasheet. Since the tensile and compressive behavior of the printing material was very similar, the tensile properties of the printing material were used in the FE models. The engineering stress-strain response of the printing material was converted into the true stress-strain one which was then imported into an elastic plastic isotropic model. For all R- and H-ReHs,  $2 \times 3$  RVEs were applied for models to match the overall dimension of the 3D-printed samples. Both R- and H-ReHs were modelled using Abaqus/Standard package. For R-ReHs, the structure was finely meshed with  $\sim 110000$  tetrahedral elements using 10-node tetrahedral solid element (C3D10). For H-ReHs, triangular cell walls of the 2<sup>nd</sup> hierarchy were meshed with  $\sim 50000$  hexahedral elements using 8-node brick element (C3D8R). Convergence tests were conducted for R-ReHs and H-ReHs models to validate that the mesh size was appropriate (as shown in Figure 3.4), and the simulation results were accurate and reliable. In the FE models, the ReH was placed between two rigid plates. A general contact was defined for the boundary conditions between the ReH sample and the rigid plate, and the tangential friction coefficient was set as 0.2 [168]. The bottom plate was fixed, while the top one was movable in the vertical direction. During the compression, a uniform displacement was applied to the top plate

with a constant velocity (9 mm/min) to simulate the experimental testing condition. Both the top and bottom rigid plates were meshed with 1800 elements using 4-node bilinear quadrilateral element (R3D4).

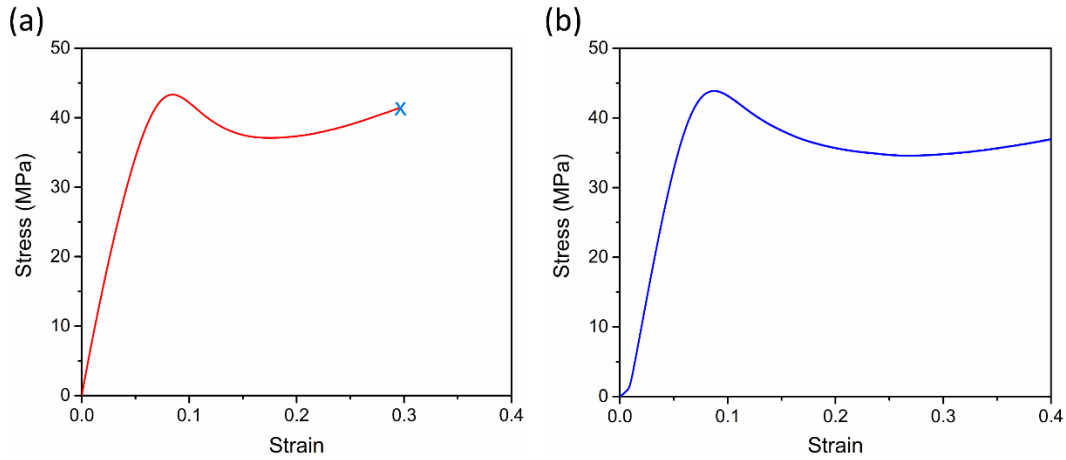


Figure 3.3. Standardized testing results of the printing material: (a) uniaxial tensile test and (b) uniaxial compressive test.

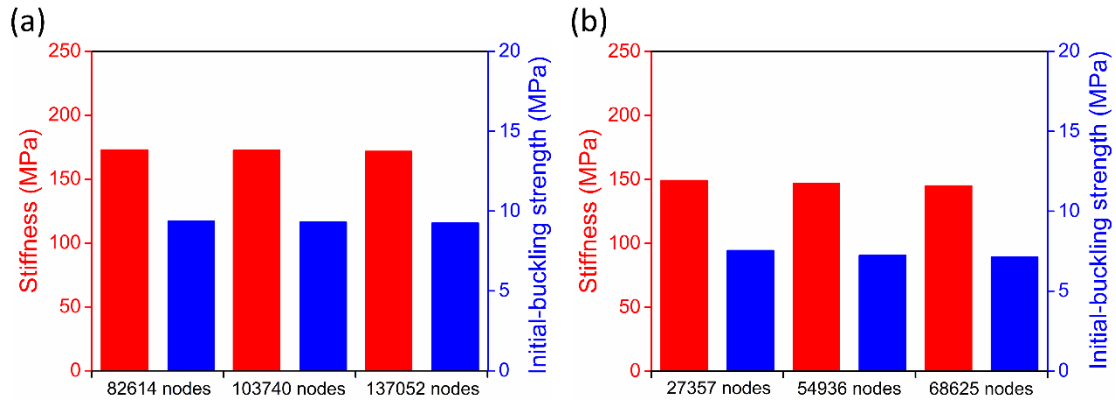


Figure 3.4. Mesh sensitivity analyses for (a) R-ReHs and (b) H-ReHs.

### 3.3 Results and Discussion

#### 3.3.1 Constitutive Behavior and Energy Absorption Performance of ReHs

The mechanical properties of ReHs have been characterized by quasi-static compressive tests, and the resulting stress-strain curves are shown in Figure 3.5. In order to evaluate the excellence of the ReHs from the lightweight perspective, the stress was further normalized by the density (Figure 3.6).

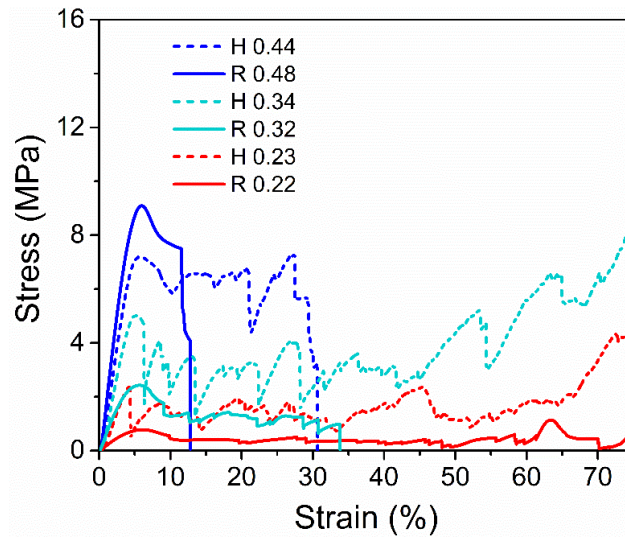


Figure 3.5. Quasi-static compressive response of R- and H-ReHs with different relative densities: stress-strain curves.

As shown in Figure 3.6 (a-c), both R- and H-ReHs initially exhibit an elastic response. In general, the normalized stress response of ReHs is lower when the relative density is smaller. Two critical criteria for the lightweight design are the specific stiffness and specific initial-buckling strength of the structure. Therefore, the specific stiffness and specific initial-buckling strength are extracted and plotted separately in Figure 3.6 (d) and (e). For H-ReHs with 0.23 relative density,

the specific stiffness and specific initial-buckling strength are significantly higher than those of the corresponding R-ReH by 250% and 170% respectively. The enhancement is attributed to the better geometrical arrangements of structural members and the stretching-dominated deformation mechanism (detailed in the section 3.3.2). When the relative density of the ReHs is larger than 0.44, the advantages of structural hierarchy are diminished. This is because the member thickness of the R-ReH is getting close to that of the H-ReH.

After reaching the initial-buckling strength, post-buckling stress plateaus are observed for both R- and H-ReHs. When the relative density is small, the H-ReHs have much higher specific post-buckling strength and larger fluctuations than the corresponding R-ReHs. The stress plateaus are terminated by either fracture or densification of the ReHs. The termination strain,  $\varepsilon_t$ , is defined as the strain at which the maximum energy absorption efficiency,  $\eta(\varepsilon)$ , is reached [169, 170]. By following Eqs (3.4) and (3.5), the termination strain is calculated and plotted in Figure. 3.6 (f).

$$\eta(\varepsilon) = \frac{1}{\sigma(\varepsilon)} \int_0^\varepsilon \sigma(\epsilon) d\epsilon \quad (3.4)$$

$$\frac{d\eta(\varepsilon)}{d\varepsilon} = 0, \text{ when } \varepsilon = \varepsilon_t \quad (3.5)$$

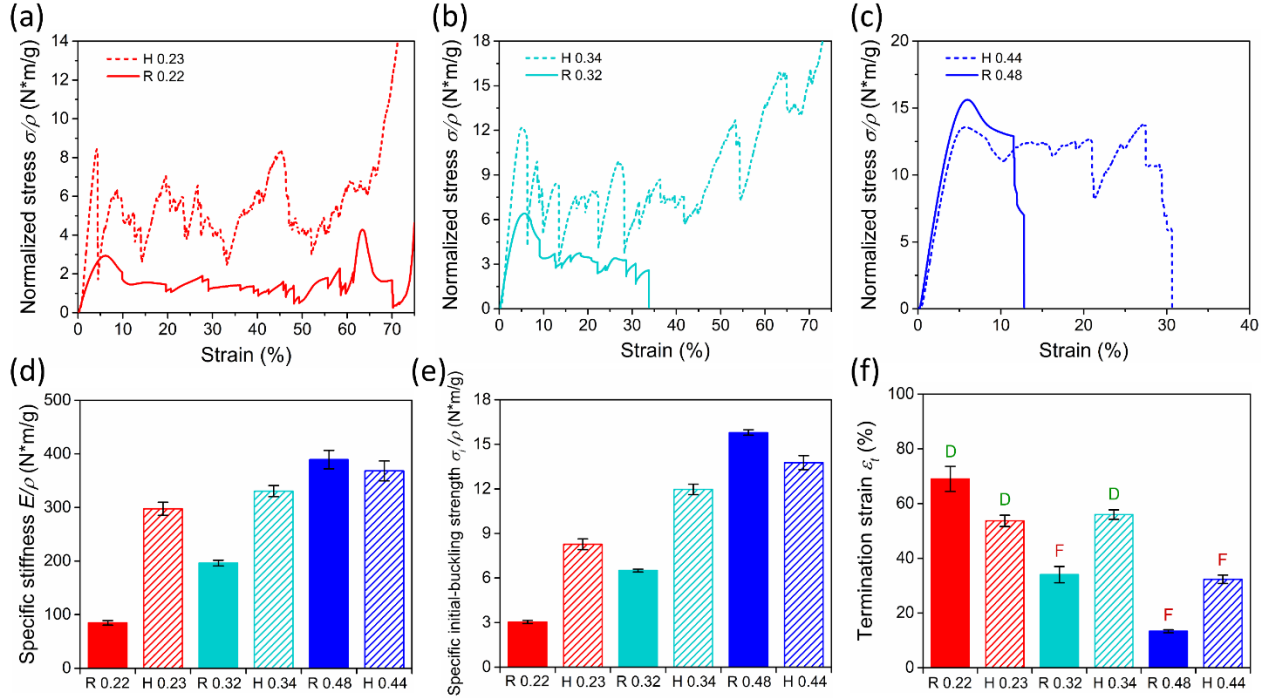


Figure 3.6. Quasi-static compressive response of R- and H-ReHs with different relative densities. (a-c) Normalized stress-strain curves of R- and H-ReHs: (a)  $\bar{\rho} = 0.23$ , (b)  $\bar{\rho} = 0.34$ , and (c)  $\bar{\rho} = 0.44$ , (d) Specific stiffness, (e) Specific initial-buckling strength, and (f) Termination strain (D and F represent the termination mode of the ReHs is either densification or fracture).

For R-ReHs,  $\varepsilon_t$  drastically decreases from 69% to 13% when the relative density increases from 0.22 to 0.48. In addition, only the R-ReH with 0.22 relative density is terminated in the densification mode, while the other two R-ReHs with larger relative densities are terminated in the fracture mode with early global failure. The ductile-to-brittle transition is triggered at a relative density in between 0.22 and 0.32. For H-ReHs, such transition takes place at a larger relative density in between 0.34 and 0.44. Moreover, when the H-ReHs are terminated in the densification mode,  $\varepsilon_t$  is independent from the relative density, as the H-ReHs with relative density of 0.23 and 0.34 have the same termination strain (~55%).

To evaluate energy absorption capacity of ReHs, the specific energy absorption capacity ( $E_s$ )

and the mean crushing force ( $F_m$ ) are calculated by Eqs (3.6) and (3.7), respectively.

$$E_s(\varepsilon) = \frac{\int \sigma d\varepsilon}{\bar{\rho} \cdot \rho_R} \quad (3.6)$$

$$F_m(\varepsilon) = \frac{A \cdot \int \sigma d\varepsilon}{\varepsilon} \quad (3.7)$$

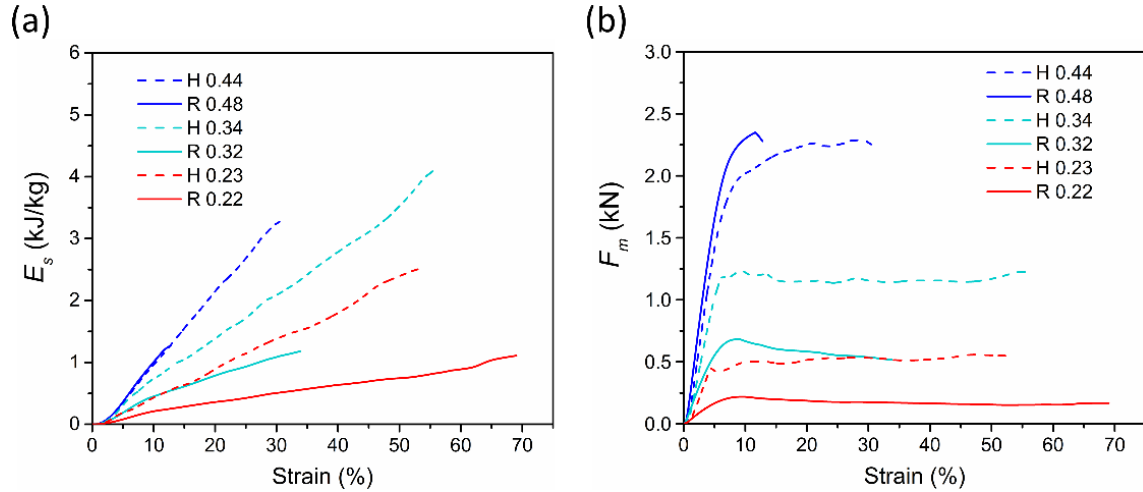


Figure 3.7. (a) Specific energy absorption and (b) Mean crushing force of R- and H-ReHs.

As shown in Figure 3.7 (a), for similar relative densities, H-ReHs have significantly higher maximum specific energy absorption capacity,  $E_s^{max}$ , than the corresponding R-ReHs. When  $\bar{\rho} \approx 0.45$ , the 157% increase in  $E_s^{max}$  is mainly due to the larger termination strain of the H-ReH. When  $\bar{\rho} \approx 0.22$ , the 130% increase in  $E_s^{max}$  is attributed to the much faster growth rate of  $E_s$ . When  $\bar{\rho} \approx 0.33$ , the increase in  $E_s^{max}$  is further promoted to 250% as both  $\varepsilon_t$  and the growth rate of  $E_s$  of the H-ReH are much larger than those of the R-ReH. The growth rate of  $E_s$  is determined by the  $F_m$ . As demonstrated in Figure 3.7 (b), the  $F_m$  for all ReHs initially increases within the elastic region. During the post-buckling process, the  $F_m$  is nearly a constant for all ReHs. When the relative density is smaller, the difference between the  $F_m$  of the R- and H-ReHs is larger.

At smaller relative density, the stiffness of the 1<sup>st</sup> and the 2<sup>nd</sup> orders of hierarchy are comparable. As the two orders of hierarchy are interconnected with each other, the deformation of both hierarchies is competing with each other. This unique interaction between the hierarchies, which does not exist in R-ReHs, enables the H-ReHs to mitigate additional amount of energy. The interaction between the hierarchies facilitates the stable propagation of local deformation sites throughout the entire structure [171]. Therefore, the specific stiffness, mean crushing force, failure strain, as well as the specific energy absorption capacity of H-ReHs are significantly improved in comparison to those of R-ReHs. In addition, this interaction varies with the relative density that determines the difference between the stiffness of the hierarchies. When the difference is large enough, one hierarchy dominates the overall performance of the overall structure and the interaction between hierarchies diminishes.

### 3.3.2 Deformation Mechanisms of H-ReHs

The improved mechanical properties of the H-ReHs are closely correlated to the unique deformation mechanisms associated with the hierarchical configuration. The negative Poisson's ratio (NPR) of the ReHs is confirmed and calculated by tracking the movements of the joints under compressive tests, as shown in Figure 3.8 (a) and (b), respectively. As illustrated in Figure 3.8 (c), the  $\nu_{xy}$  of both ReHs is negative and nearly constant in the elastic range deformation ( $\varepsilon \leq 5\%$ ). However, at same relative density, the  $\nu_{xy}$  of H-ReH is smaller than that of R-ReH. This is attributed to the different deformation mechanisms of the R- and H-ReHs.

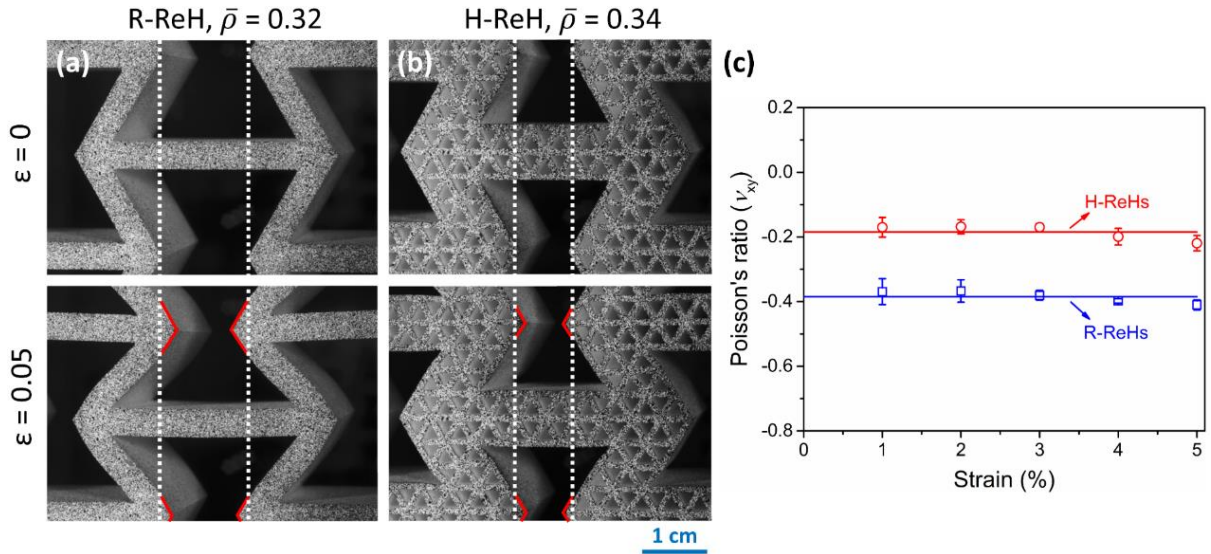


Figure 3.8. Experimental images of (a) R-ReH ( $\bar{\rho} = 0.32$ ) and (b) H-ReH ( $\bar{\rho} = 0.34$ ) at  $\varepsilon = 0.05$ , and (c) Poisson's ratio ( $\nu_{xy}$ ) for corresponding R-ReH and H-ReH.

The strain fields of the central RVEs measured by the 3D-DIC are shown in Figure 3.9. For R-ReHs, all the horizontal and inclined members are under bending. Figure 3.9 (a) illustrates the strain field in the  $0^\circ$  direction. The top section of the horizontal member is in compression, while the bottom section is in tension. The central axis along the  $0^\circ$  direction of the horizontal member is nearly stress free as the neutral axis of a beam under bending. Figure 3.9 (b) and (c) display the strain field along the axis of inclined members ( $\pm 60^\circ$ ). Similar to the horizontal member, the inclined ones are in pure bending mode, as the inner and outer sections are under compression and tension, respectively. The compression and tension zones are separated by the neutral axis at the center of the members. This bending behavior is resulted from the rotation of the struts at joints [21, 172].

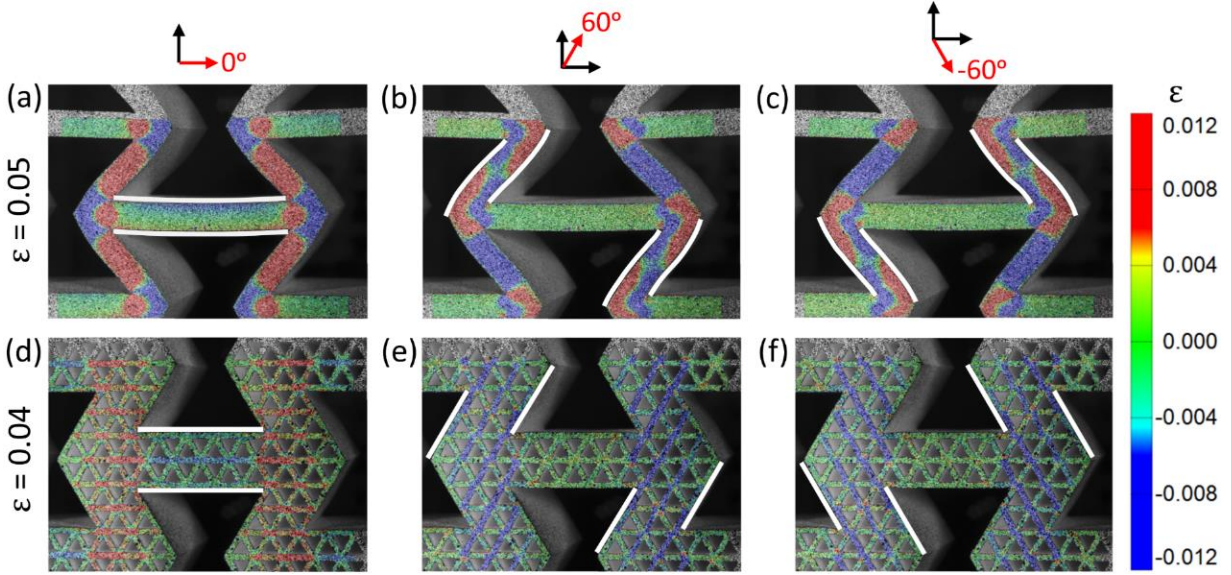


Figure 3.9. DIC strain fields of R-ReH ( $\bar{\rho} = 0.32$ ) at  $\varepsilon = 0.05$  (a-c) in  $0^\circ$ ,  $60^\circ$  and  $-60^\circ$  directions, and H-ReH ( $\bar{\rho} = 0.34$ ) at  $\varepsilon = 0.04$  (d-f) in  $0^\circ$ ,  $60^\circ$  and  $-60^\circ$  directions.

By contrast, both orders of hierarchy of H-ReHs exhibit stretching-dominated deformation. For the 2<sup>nd</sup> order of hierarchy, the triangular framework satisfies the topological criteria for stretching-dominated deformation mechanism [21], which is validated by the uniformly distributed strain fields in the struts of the 2<sup>nd</sup> order of hierarchy along the axis direction of the 1<sup>st</sup> order of hierarchy (Figure 3.9 (e) and (f)). All the struts are carrying loads axially without rotation at joints. As depicted in Figure 3.9 (d-f), the contours of all the 1<sup>st</sup> order of hierarchical members are nearly straight. All these members are composed of the stretching-dominated 2<sup>nd</sup> order triangular units. Besides, the members have enhanced bending stiffness, as the member weight is arranged further away from the neutral axis. The stretching-dominated deformation mechanism of the H-ReHs in the elastic range effectively improves the specific stiffness and initial-buckling strength than those of bending-dominated R-ReHs [108].

Once the initial-buckling strength is reached, the ReHs undergo nonlinear deformation till the termination strain. However, the post-buckling behavior of R- and H-ReHs is governed by different deformation mechanisms. The typical deformation patterns of R- and H-ReHs are presented in Figure 3.10 (a-c). For R-ReHs, due to the bending-dominated elastic behavior, severe stress concentration is developed at the joints (Figure 3.10 (a)). When the applied compressive stress is higher than  $\sigma_i$ , early fractures ( $\varepsilon < 0.1$ ) occur at vulnerable joints, as shown in Figure 3.10 (d). The fractured members neither carry the external load nor provide constraints to adjacent members, which leads reduced post-buckling strength of R-ReHs and compromised structural stability (Figure 3.10 (a-b)). With the increase of local fractures shear bands are fully developed (Figure 3.10 (b)), and thus the R-ReHs tend to fail in global fracture with a smaller termination strain.

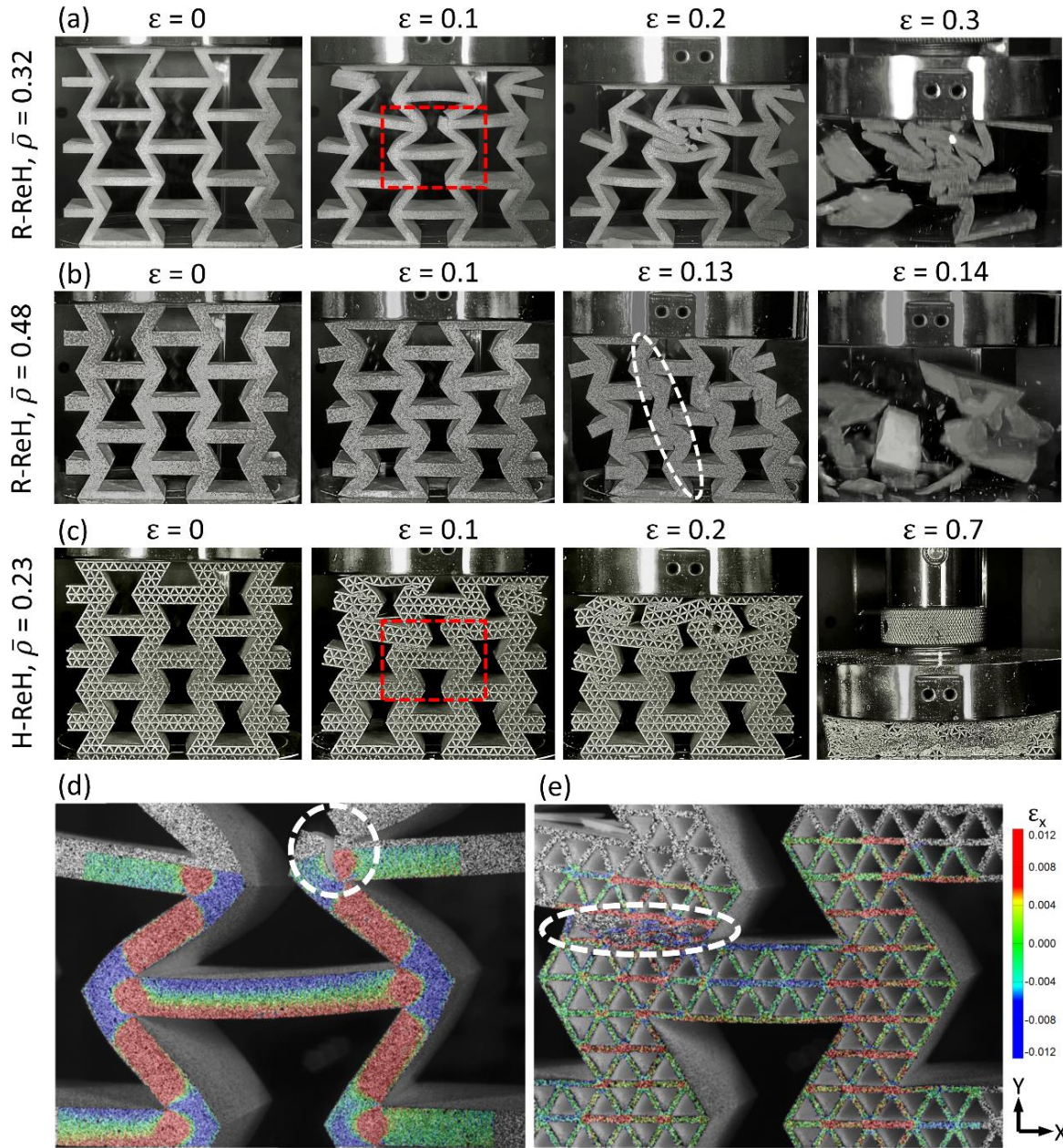


Figure 3.10. Deformation patterns of (a) R-ReH ( $\bar{\rho} = 0.32$ ), (b) R-ReH ( $\bar{\rho} = 0.48$ ) and (c) H-ReH ( $\bar{\rho} = 0.23$ ). DIC strain fields of central RVEs of (d) R-ReH ( $\bar{\rho} = 0.32$ ) and (e) H-ReH ( $\bar{\rho} = 0.23$ ).

By contrast, the post-buckling behavior of H-ReHs is dominated by the densification of the 2<sup>nd</sup> order of hierarchy instead of the fracture. As shown in Figure 3.10 (c), the stretching-dominated

triangular hierarchical struts of inclined members firstly exhibit local buckling behavior, followed by complete densification of the local 2<sup>nd</sup> order of hierarchy (Figure 3.10 (e)). As the local densification strain is small, the structural stability of H-ReHs in the nonlinear region is significantly enhanced. Consequently, the H-ReHs have higher post-buckling strength than ReHs. The local densification of the 2<sup>nd</sup> order of hierarchy is progressive from one site to another. With more and more densified 2<sup>nd</sup> hierarchy, stress concentration is built up around the joints and local fractures of the 1<sup>st</sup> hierarchy occur. The local densification of the 2<sup>nd</sup> hierarchy as well as the local fracture of the 1<sup>st</sup> hierarchy cause the fluctuation in the post-buckling stress plateau of H-ReHs. Please note that a shear band is not fully developed in the H-ReHs with small relative density as the global structural stability is enhanced and the local fracture of the 1<sup>st</sup> hierarchy is postponed by the local buckling of the 2<sup>nd</sup> hierarchy. Eventually, H-ReHs tend to be fully densified without global fracture at a larger termination strain.

The combined higher specific stiffness and specific initial-buckling, higher post-buckling strength, and larger termination strain result in the superior energy absorption performance of the H-ReHs.

It is noteworthy that the mechanical properties as well as the deformation mechanisms of H-ReHs depend on the slenderness of the 2<sup>nd</sup> triangular hierarchy,  $l_h/t_t$ . As shown in Figure 3.11 (a), the H-ReH ( $\bar{\rho} = 0.23$ ) has the slenderest triangular cell walls which tend to buckle at a lower stress. The additional spacing between the slender cell walls promotes the local densification of the 2<sup>nd</sup> hierarchy and the termination strain of the structure. The slenderness also reduces the bending stiffness and rigidity of the 1<sup>st</sup> hierarchy. Therefore, the 1<sup>st</sup> order members and joints are

more vulnerable to bending and rotation in the post-buckling region, leading to a relatively lower growth rate of specific energy absorption (Figure 3.11 (d)). On the other hand, the H-ReH ( $\bar{\rho} = 0.44$ ) with the lowest  $l_h/t_t$  has a much-enhanced resistance to local buckling, joint rotation and member bending. Therefore, this specific H-ReH exhibits the highest initial- and post-buckling strengths (Figure 3.6). However, the thicker triangular cell walls reduce the overall porosity of the structure. More importantly, as the 2<sup>nd</sup> hierarchy is stronger than the 1<sup>st</sup> one, local fracture at the joints instead of local densification of the 2<sup>nd</sup> hierarchy dominate the post-buckling behavior. Consequently, this H-ReH becomes “less hierarchical”, leading to compromised structural stability (Figure 3.11(c)), and smaller maximum specific energy absorption (Figure 3.11 (d)).

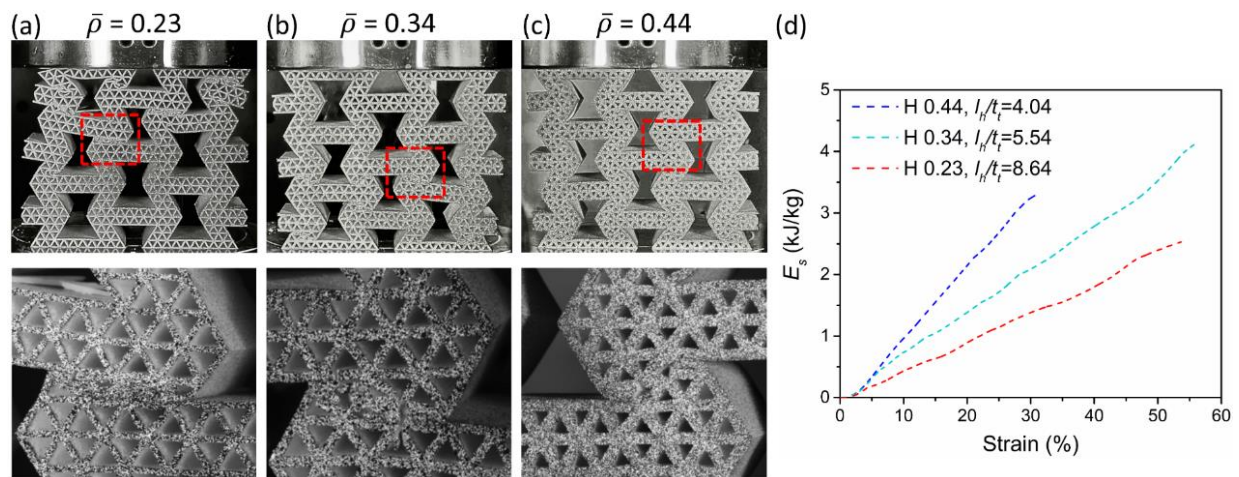


Figure 3.11. Effect of the slenderness of the 2<sup>nd</sup> order triangular hierarchy on (a) – (c) the local deformation mechanisms at  $\varepsilon = 0.1$ , where  $l_h/t_t = 8.64, 5.54$ , and  $4.04$ ; and (d) specific energy absorption of the H-ReHs.

Based on the above discussion, there is a trade-off between the buckling strength and the termination strain. H-ReHs with an optimal slenderness of the 2<sup>nd</sup> triangular hierarchy may reach

the balance between the buckling strength and the termination strain, and thus maximize the energy absorption and other mechanical performance. As suggested in Figure 3.6 and Figure 3.7 (a), the H-ReH ( $\bar{\rho} = 0.34$ ) with intermediate slenderness shows a better combination of strength and termination strain. The deformation mechanism is the combined local densification of the 2<sup>nd</sup> hierarchy and the fracture of the 1<sup>st</sup> hierarchy (Figure 3.11 (b)), which contributes to the highest maximum specific energy absorption and the largest termination strain, as shown in Figure 3.11 (d). Please note that in the current design strategy,  $l_h$  is a constant and the slenderness of the 2<sup>nd</sup> order triangular hierarchy is simply determined by  $t_t$ . Based on the fundamental understanding on the effect of slenderness on the structural performance,  $l_h$  can be extended as an additional degree of freedom for future designs.

The deformation patterns of the ReHs: (R-ReH ( $\bar{\rho} = 0.22$ ), H-ReH ( $\bar{\rho} = 0.34$ ) and ( $\bar{\rho} = 0.44$ ) are shown in Figure 3.12. DIC strain fields of H-ReHs and R-ReHs of all relative densities at  $\varepsilon = 0.04$  in various directions are shown in Figure 3.13 – 3.16.

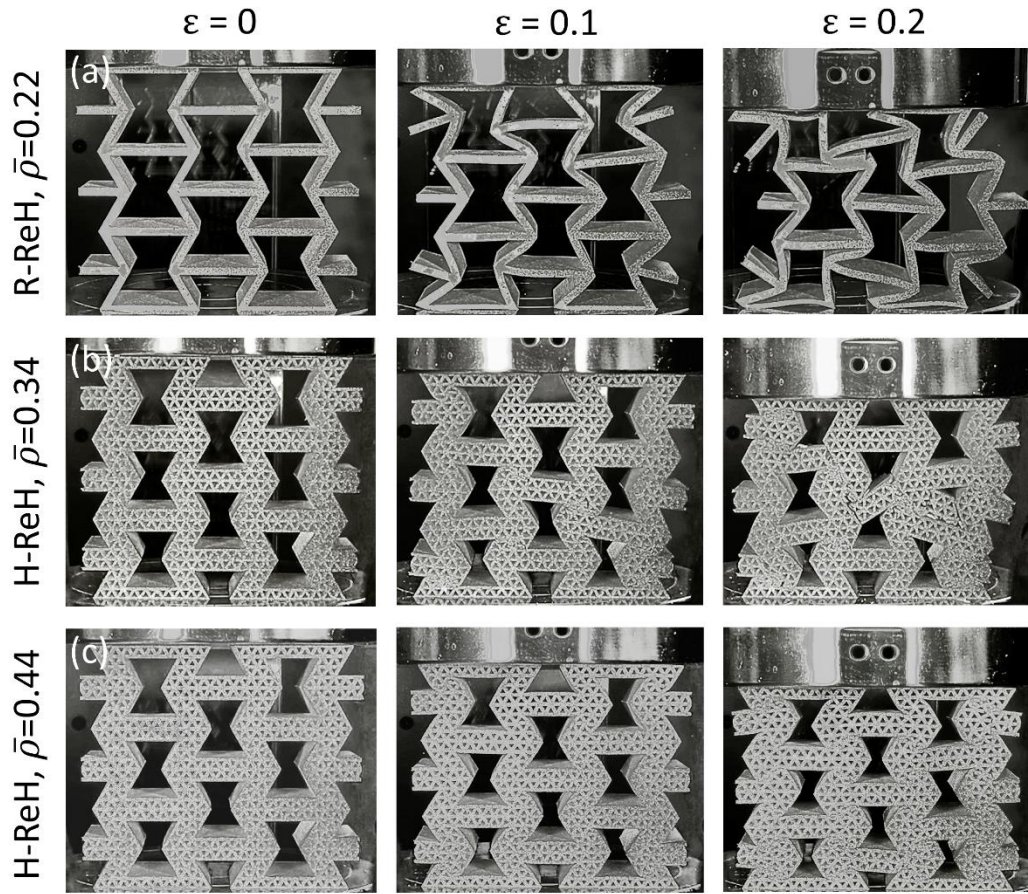


Figure 3.12. Deformation patterns of (a) R-ReH ( $\bar{\rho} = 0.22$ ), (b) H-ReH ( $\bar{\rho} = 0.34$ ) and (c) H-ReH ( $\bar{\rho} = 0.44$ ).

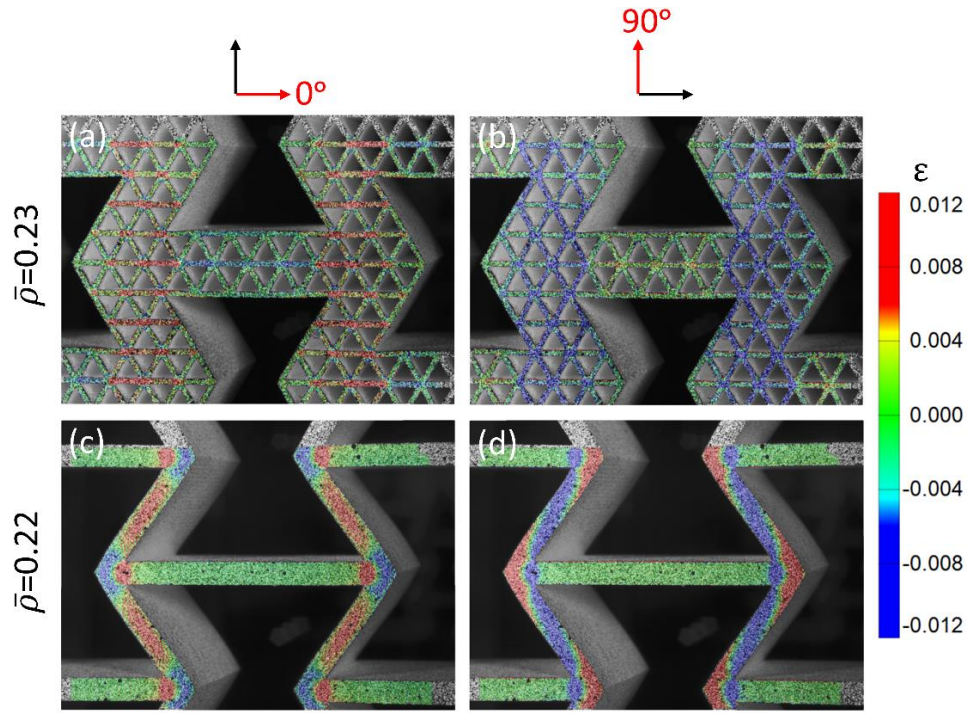


Figure 3.13. DIC strain fields of H-ReH ( $\bar{\rho} = 0.23$ ) at  $\epsilon = 0.04$  (a) in  $0^\circ$ , and (b)  $90^\circ$ , and R-ReH ( $\bar{\rho} = 0.22$ ) at  $\epsilon = 0.04$  (c) in  $0^\circ$ , and (d)  $90^\circ$ .

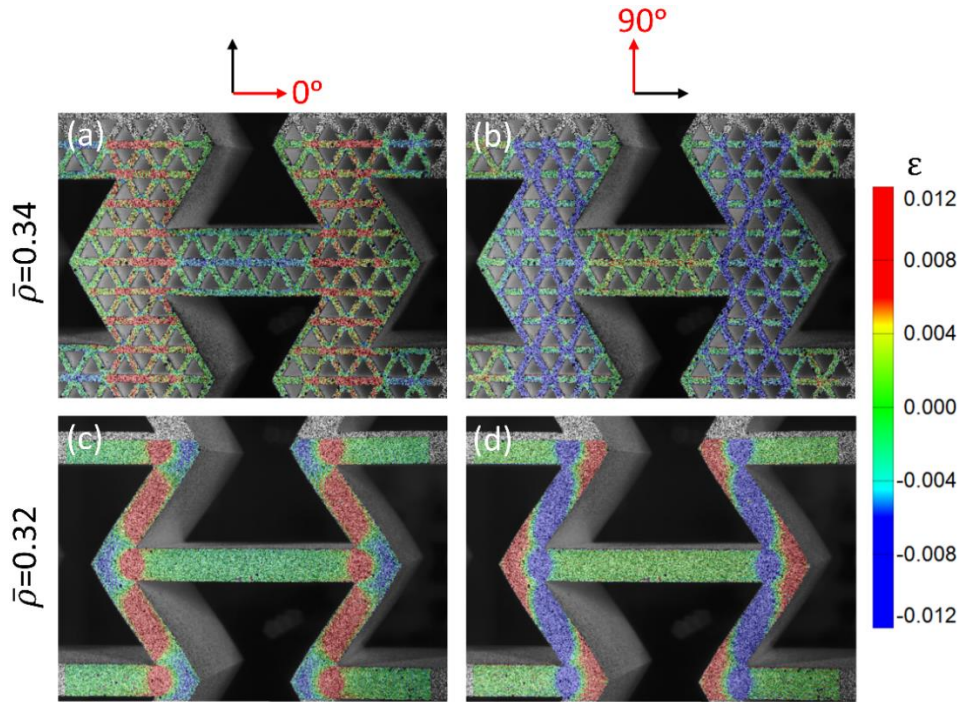


Figure 3.14. DIC strain fields of H-ReH ( $\bar{\rho} = 0.34$ ) at  $\epsilon = 0.04$  (a) in  $0^\circ$ , and (b)  $90^\circ$ , and R-ReH ( $\bar{\rho} = 0.32$ ) at  $\epsilon = 0.04$  (c) in  $0^\circ$ , and (d)  $90^\circ$ .

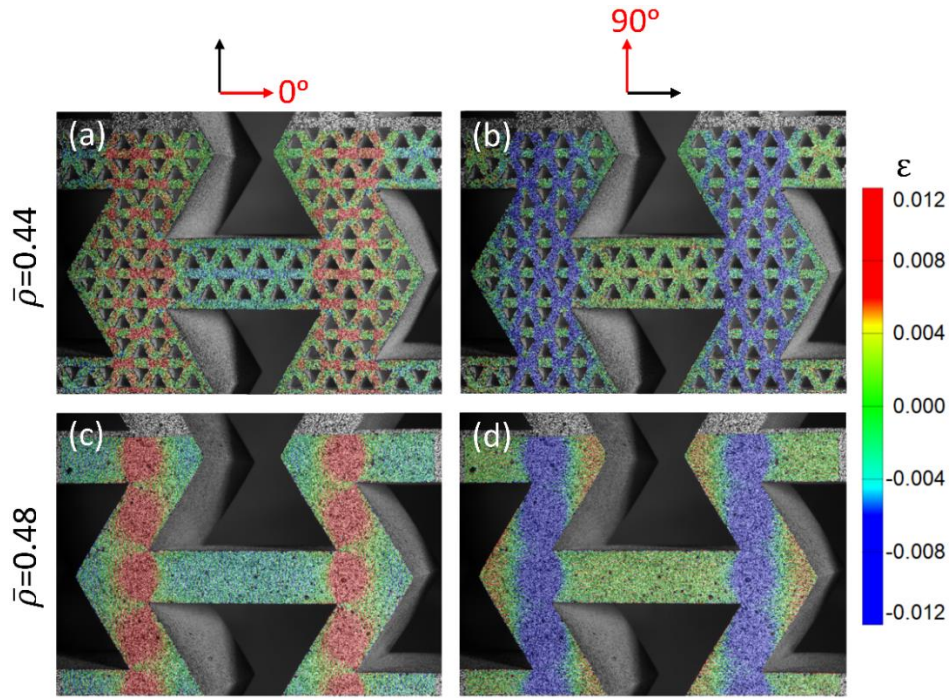


Figure 3.15. DIC strain fields of H-ReH ( $\bar{\rho} = 0.44$ ) at  $\epsilon = 0.04$  (a) in  $0^\circ$ , and (b)  $90^\circ$ , and R-ReH ( $\bar{\rho} = 0.48$ ) at  $\epsilon = 0.04$  (c) in  $0^\circ$ , and (d)  $90^\circ$ .

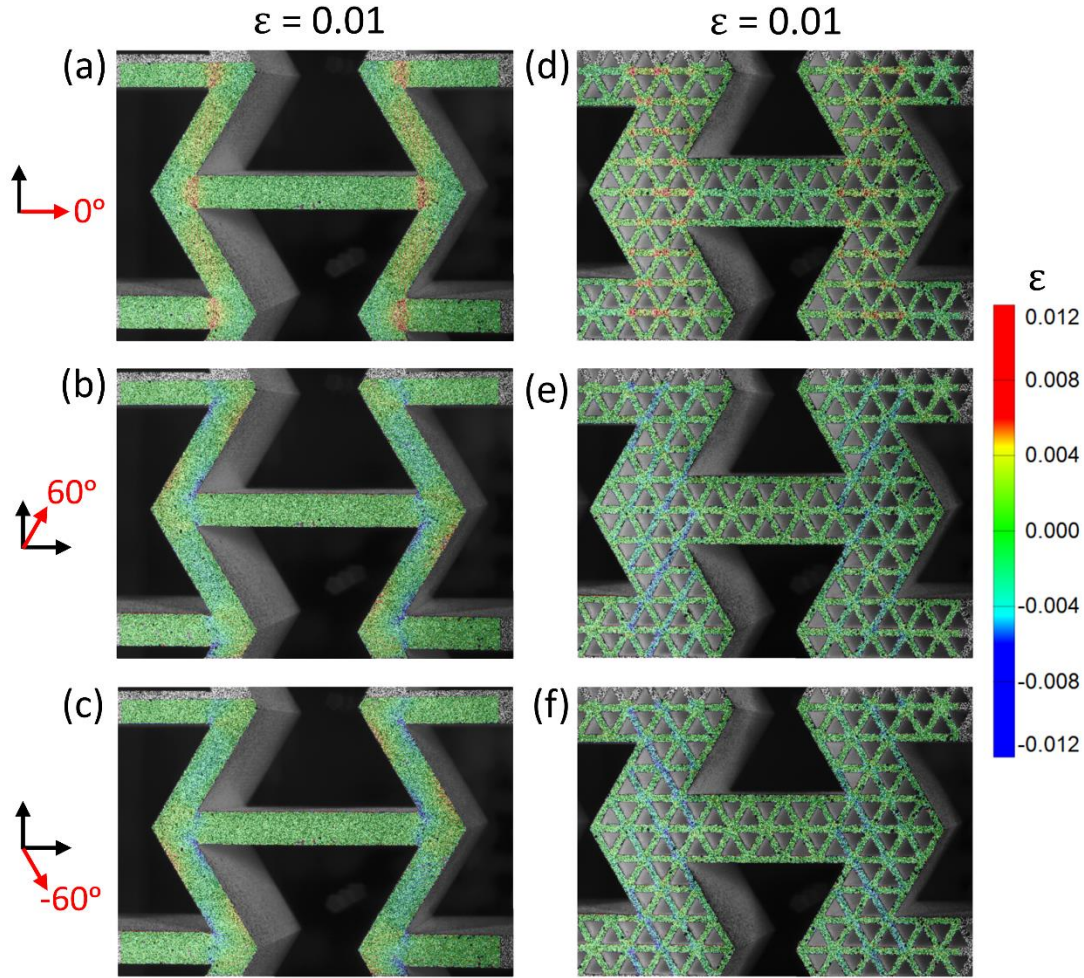


Figure 3.16. DIC strain fields of R-ReH ( $\bar{\rho} = 0.32$ ) at  $\varepsilon = 0.01$  (a-c) in  $0^\circ$ ,  $+60^\circ$  and  $-60^\circ$  directions, and H-ReH ( $\bar{\rho} = 0.34$ ) at  $\varepsilon = 0.01$  (d-f) in  $0^\circ$ ,  $+60^\circ$  and  $-60^\circ$  directions.

### 3.3.3 Numerical Simulation and Scaling Laws of ReHs

Finite element method (FEM) is employed to extract the governing structure-property relationship of the ReHs. FE models for R- and H-ReHs are firstly generated and then validated by existing experimental results. The constitutive behavior of ReHs with relative densities in the range of 0.2 – 0.5 simulated by the FE models shows great agreement with the experimental data and is presented in Figure 3.17 (a). In addition, the deformation patterns of R- (bending dominated)

and H- (stretching dominated) ReHs within elastic region are also accurately captured by the models, as shown in Figure 3.17 (b) and (c).

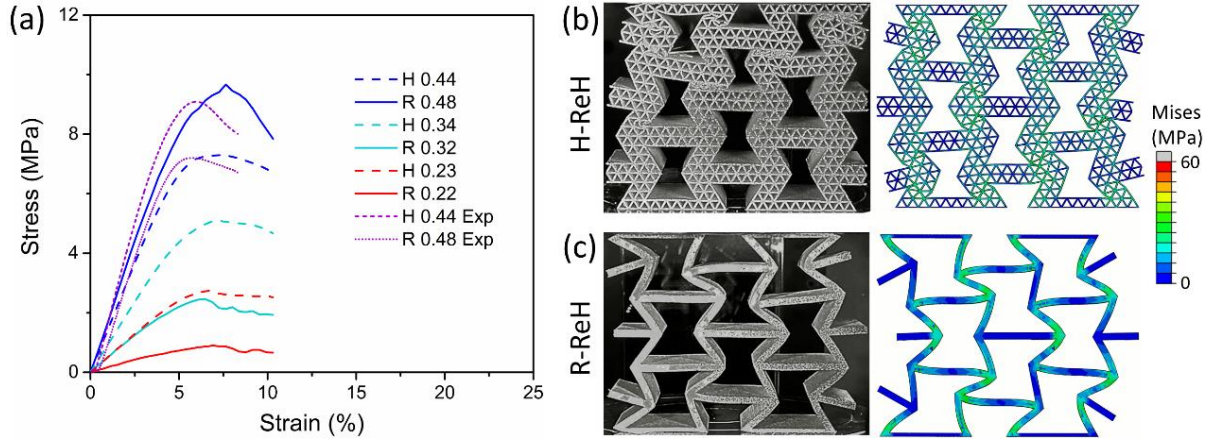


Figure 3.17. Numerical simulation of R- and H-ReHs. (a) Simulated constitutive behavior compared with experimental results, and simulated deformation patterns of (b) H-ReH, and (c) R-ReH.

The simulated deformation patterns of H- and R-ReHs are shown in Figure 3.18.

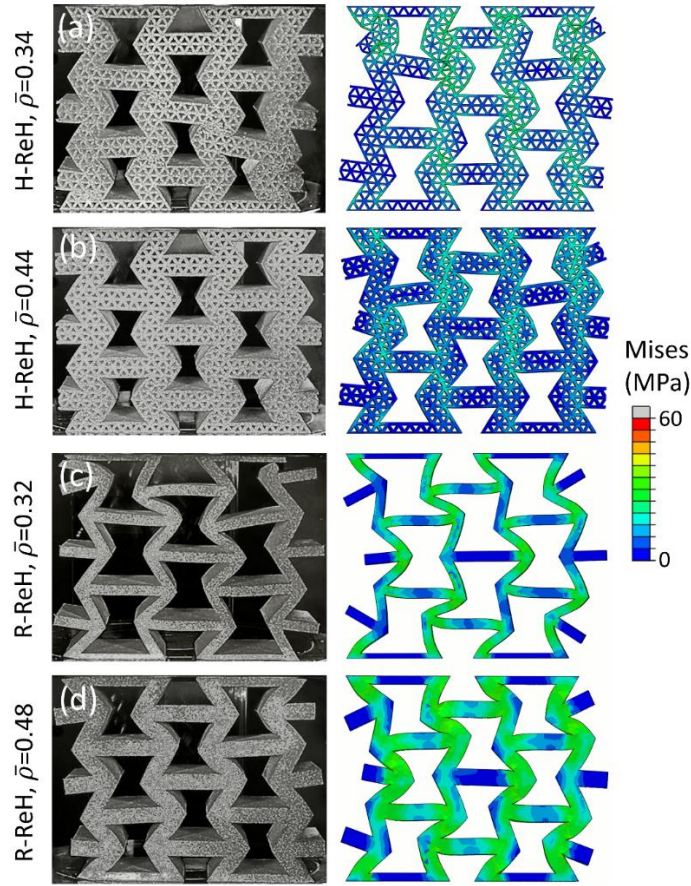


Figure 3.18. Simulated deformation patterns of H- and R-ReHs. (a) H-ReH ( $\bar{\rho} = 0.34$ ), (b) H-ReH ( $\bar{\rho} = 0.44$ ), (c) R-ReH ( $\bar{\rho} = 0.32$ ), and (d) R-ReH ( $\bar{\rho} = 0.48$ ).

It is known that the mechanical properties of cellular structures are determined by the relative density by following a scaling law [173]. To capture the scaling law for the ReHs, the validated FE models are used to predict the stiffness and initial-buckling strength of both R- and H-ReHs with wider relative densities range. The R- and H-ReHs with relative densities from 0.04 to 0.6 are developed by changing the thickness of the structural members only (as shown in Figure 3.1,  $t$  for R-ReH and  $t_t$  for H-ReH). The relative stiffness and relative initial-buckling strength are plotted as functions of relative density by following the scaling laws in the format of  $E/E_R = A(\rho/\rho_R)^m$  and

$\sigma_i/\sigma_R = B(\rho/\rho_R)^n$ , respectively, where  $A$  and  $B$  are geometry-dependent parameters, and  $m$  and  $n$  are scaling exponents. The scaling law parameters are presented in Table 3.2. All experimental and numerical data are plotted in log scale in Figure 3.19. It is observed that both relative stiffness and relative initial-buckling strength of all ReHs are following linear scaling relationships with the relative density. However, the scaling exponents for R- and H-ReHs are different. Specifically, the scaling exponents of relative stiffness of the R- and H-ReHs are 1.4 and 2.7, respectively (Figure 3.19 (a)). The  $m_H$  is closer to 1, which indicates the stretching-dominated deformation mechanism of H-ReHs in the elastic range, and outperforms stretching-dominated alumina-polymer triangular micro lattice structure [174] and MAG octet-gyroid lattice structure [175]. The R-ReHs exhibit similar behavior to that of stochastic foams with  $m_F = 3$  [42], indicating the bending-dominated deformation mechanism. These results validate that the introduction of the 2<sup>nd</sup> order triangular hierarchy convert the bending-dominated R-ReHs into stretching-dominated H-ReHs.

All the ReHs follow a similar scaling law for the relative initial-buckling strength versus relative density (Figure 3.19 (b)). The scaling exponents,  $n$ , for the R- and H-ReHs are very close, as both structures undergo local buckling when  $\sigma = \sigma_i$ . Please note that the superior post-buckling behavior of the H-ReHs over the R-ReHs cannot be captured by current model due to the complex deformation mechanisms.

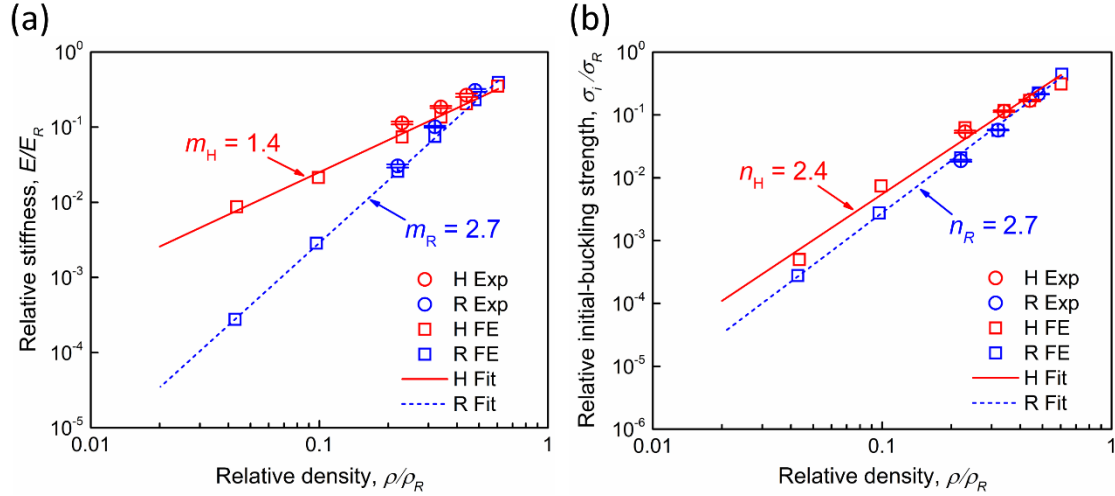


Figure 3.19. Scaling laws for ReHs (a) Relative stiffness, and (b) Relative initial-buckling strength.

Table 3.2. The scaling law parameters of relative stiffness and relative initial-buckling strength of ReHs versus relative density.

	Relative stiffness		Relative initial-buckling strength	
	$A$	$m$	$B$	$n$
R	1.21	2.7	1.18	2.7
H	0.73	1.4	1.17	2.4

### 3.4 Conclusions

In the study, we have presented a strategic design of hierarchical re-entrant honeycombs that exhibit enhanced mechanical properties under quasi-static compression. Through a combined DIC analyses and numerical approach, novel deformation mechanisms governing the mechanical properties of hierarchical re-entrant honeycombs have been revealed. Major findings can be summarized as follows:

- (1) When the relative density is small, the H-ReHs have higher stiffness, initial-buckling strength, and specific energy absorption capacity than corresponding R-ReHs. When the

relative density is large, H-ReHs exhibit better structural stability, larger termination strain and specific energy absorption capacity than corresponding R-ReHs.

- (2) The superior properties of H-ReHs are endowed by the introduction of the 2<sup>nd</sup> order triangular hierarchy into ReHs. The additional hierarchy successfully converts the deformation mechanism from bending-dominated to stretching-dominated in the elastic range. In addition, a unique combination of local-buckling, densification and fracture deformation mechanisms of the H-ReHs is revealed, which contributes to significant improvement of the mechanical properties of H-ReHs.
- (3) Among the deformation mechanisms of H-ReHs, there is a competition between the 1<sup>st</sup> and the 2<sup>nd</sup> order of hierarchy, which is governed by the slenderness of the 2<sup>nd</sup> order triangular hierarchy.
- (4) The relative stiffness and the relative initial-buckling strength of both H- and R-ReHs follow scaling laws. The scaling exponents of the relative stiffness confirm the stretching-dominated behavior of H-ReHs and bending-dominated behavior of R-ReHs.

Overall, this study provides the understanding of the structure-property relationship and the deformation mechanism of ReHs, which paves the way for the engineering design of next generation ultralight materials.

## **CHAPTER 4. ANGLE EFFECT ON THE MECHANICAL PROPERTIES OF 3D-PRINTED HIERARCHICAL RE-ENTRANT HONEYCOMB**

Hierarchical re-entrant honeycombs (H-ReHs) have demonstrated unique mechanical characteristics and superior energy absorption capacity. However, the optimized hierarchical design is yet to be explored so as to realize better mechanical properties of H-ReHs. In this chapter, we develop new H-ReHs by applying various angle designs on the 2<sup>nd</sup> order triangular hierarchy of H-ReHs. For references, regular re-entrant honeycombs (R-ReHs) with same angles without 2<sup>nd</sup> order hierarchy are characterized as well. The in-plane crushing behaviors of new H-ReHs are characterized under quasi-static compression tests. Results show that increasing the angle in H-ReHs can significantly enhance the elastic modulus, strength, structural stability, and energy absorption capacity. In addition, H-ReHs are much more sensitive toward angle designs compared to R-ReHs. By investigating the deformation mechanisms of H-ReHs, it is found that the interaction between the 1<sup>st</sup> order and 2<sup>nd</sup> order hierarchy is significantly affected by angle designs, which governs the enhancement of mechanical properties. These findings not only demonstrate great tunability of H-ReHs through angle designs, but also provide new understandings on the design of H-ReHs as lightweight safety devices.

### **4.1 Introduction**

The requirements of robust and lightweight materials have seen tremendous increase in the industries including aerospace [176], automotive [144], defense [146, 177], and biomedical sectors [147, 178]. Conventional cellular materials such as honeycombs have been widely used due to its

lightweight nature and decent mechanical properties [27, 179]. However, the in-plane crashworthiness of honeycombs is still weak [180]. In order to improve that, the auxetic re-entrant honeycombs (ReHs) have been proposed and extensively studied. With the unique deformation mechanisms, the ReHs exhibit excellent indentation resistance, fracture toughness and energy absorption capacity, which outperform the conventional honeycombs [70, 99, 100, 151]. It is noted that the mechanical characteristics of ReHs are not just determined by the base materials, but also dominated by the cell structure properties. Therefore, it is essential to explore the relationship between the cell structure design and crushing behavior of the ReHs so as to realize better architectural design of ReHs with enhanced properties for various applications [181].

There are several geometric parameters that govern the cell structure design of ReHs, such as aspect ratio, cell-wall angle, and volume fraction [182-184]. Among them, the cell-wall angle can be easily tuned to obtain new cell structures with distinct deformation modes and different auxetic properties. Recently, the cell-wall angle effect on the mechanical properties of the ReHs have been extensively researched. For example, Choudhry et al. found that cell-wall angles have significant effects on the compressive strength of the ReHs [155]. Hu et al indicated that the indentation resistance and negative Poisson's ratio effect were enhanced with increasing the cell-wall angle [185]. Zhang et al. discussed the effect of cell-wall angle on plateau stress and energy-absorbed ability of ReHs under the dynamic crushing [182]. Wu et al. developed the graded cell-wall angle design of ReHs and achieved enhanced energy absorption capacity under low-velocity impact or quasi-static loadings [186]. Gu et al. studied the cell-wall angle effect on the tensile behaviors of the ReHs and revealed that ReHs with smaller angles had more significant auxetic property under

stretching [187]. These researches have demonstrated that the cell-wall angle have significant effect on the crushing behaviors and deformation mechanisms of the ReHs. Therefore, optimizing the cell-wall angle in the ReHs can effectively improve the mechanical properties of ReHs.

In addition to the cell-wall angle, the hierarchical structures can improve the mechanical properties of ReHs as well. Natural hierarchical materials such as bone and wood, have exhibited amazingly high stiffness and strength [44, 45, 47, 188-190]. Their configurations are composed of structural hierarchy over multiple length scales. Inspired by this, hierarchical topologies have been also introduced into the ReHs as a novel design to improve their mechanical properties [107]. By substituting the solid ligaments of ReHs with the smaller, 2<sup>nd</sup> order hierarchical structures, the hierarchical re-entrant honeycombs (H-ReHs) have been developed, which exhibits a much-enhanced energy absorption capacity over regular ReHs [102, 104, 106, 107, 126, 167]. The enhancement of H-ReHs originates from unique local deformation of 2<sup>nd</sup> order hierarchy in coordination with the macro deformation of 1<sup>st</sup> order hierarchy. It is noteworthy that the geometric parameters of the H-ReHs can considerably affect the deformation mechanisms and the mechanical properties of the H-ReHs, and therefore is of great significance [102]. Since the cell-wall angle plays a prominent role on the deformation mechanisms and mechanical properties of regular ReHs, it is expected that tuning the angle design of hierarchical structures in H-ReHs has great potential to coordinate both local and macro deformation modes of H-ReHs, thus achieves distinctive mechanical properties. As the cell-wall angle can be easily adjusted, it is feasible to optimize the mechanical performance of the H-ReHs through fast prototyping. However, research exploring the effect of hierarchical angle design on the mechanical performance of H-ReHs, to the best of our

knowledge, is scarce and lack of experimental validations.

In this study, we apply three different angle designs, namely  $45^\circ$ ,  $60^\circ$ , and  $75^\circ$ , on the 2<sup>nd</sup> order triangular hierarchy in H-ReHs, then incorporate them into the 1<sup>st</sup> order hierarchy, the cell walls of the ReHs, thereby construct three hierarchical re-entrant honeycombs (H-ReHs) with different angle designs accordingly. For references, regular re-entrant honeycombs (R-ReHs) with same angles without 2<sup>nd</sup> order triangular hierarchy are characterized as well. Thanks to the advanced Polyjet 3D printing technique [191], the complex H-ReHs with various angle designs can be fabricated and experimentally characterized. Through quasi-static compression tests and strain field analyses, we aim to investigate the influences of angle designs on the mechanical properties and the deformation mechanisms of H-ReHs, reveal the underlying interaction between 1<sup>st</sup> and 2<sup>nd</sup> order hierarchy, thus ultimately shed light on the optimal angle design strategy for the H-ReHs.

## **4.2 Materials and Methods**

### **4.2.1 Design of H-ReH and R-ReH with Different Angles**

Figure 4.1. shows configurations of  $45^\circ$ ,  $60^\circ$ , and  $75^\circ$  H-ReH and R-ReH representative volume elements (RVE), respectively. For the design of H-ReH with different angles, the geometry of the H-ReH RVE was adjusted by tuning the angle between the horizontal and inclined struts of triangles as the 2<sup>nd</sup> order triangular hierarchy. After that, the angle between horizontal and inclined members of 1<sup>st</sup> order hierarchy was also adjusted accordingly to fit with 2<sup>nd</sup> order triangular hierarchy with the number of triangular hierarchy remains constant. The dimension of the H-ReH

REV was determined by two geometric parameters, i.e. the width of RVE ( $W_H$ ), and the height of RVE ( $H_H$ ). The 2<sup>nd</sup> order structural hierarchy in the H-ReH RVE was specified by the thickness ( $t_t$ ) and the length ( $l_t$ ) of the triangular cell wall, as shown in Figure 4.1 (a). By contrast, the dimension of R-ReH RVE was determined by the width ( $W_R$ ), height ( $H_R$ ), and member thickness ( $t_R$ ). The out of plane thickness ( $T$ ) of H-ReH and R-ReH samples are thick enough (15 mm) to avoid out of plane buckling under compressive tests. Please note that for straightforward comparison, all H-ReH and R-ReH are designed to have a same relative density of 0.34.

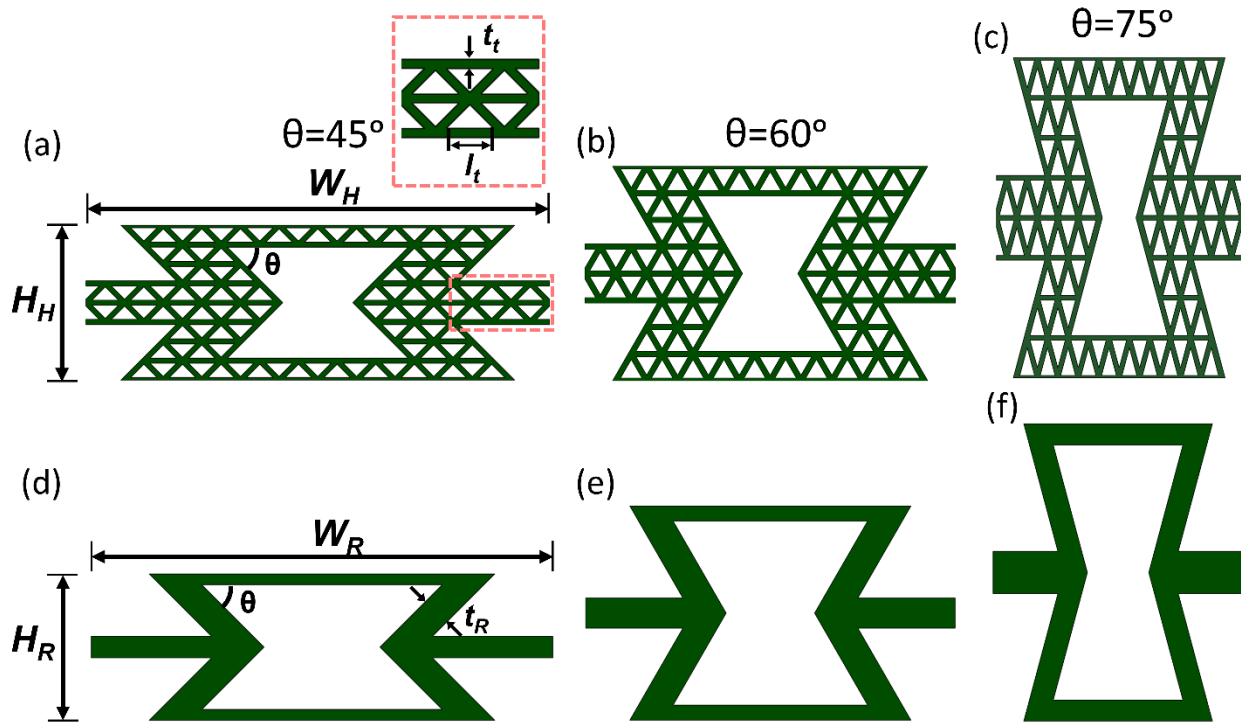


Figure 4.1. Design and configuration of (a) 45°, (b) 60° and (c) 75° H-ReH and R-ReH ( $\bar{\rho} = 0.34$ ) representative volume elements.

## 4.2.2 Materials and Sample Preparation

All ReH samples were fabricated using a Polyjet 3D printer (Objet Connex350, Stratasys, Ltd.). A durable engineered photopolymers, Rigur (RGD450, Stratasys, Ltd), was used as the printing material. The constitutive behavior of the printing material is measured by following the ASTM D638-14 tensile test and shown in Figure 4.2 (a). The Young's modulus is determined as  $E_R = 734.1$  MPa. The tensile strength is determined as  $\sigma_R = 43.0$  MPa. The density of the printing material,  $\rho_R$ , is  $1200 \text{ kg/m}^3$ , and the Poisson's ratio of the printing material is 0.3, which can be obtained from the manufacture datasheet. After jetting the printing material droplets onto the build platform, materials were cured by UV light to solidify. The temperature of printer extruder was kept at  $70 \text{ }^\circ\text{C}$  during the printing process, while the printer platform was kept at room temperature. All samples were printed under same printing parameters. The typical H-ReH and R-ReH unit cell samples printed by Rigur material are shown in Figure 4.2 (b-d). All printed samples have a compatible overall dimension for 3D DIC analyses during the mechanical testing. The geometric details of the fabricated H-ReH and R-ReH samples with different angles are summarized in Table 4.1. For each angle design, at least 3 samples were prepared and tested. After the finish of the printing, all samples were put in room temperature for 9 days to allow fully cure of the printing material before the testings.

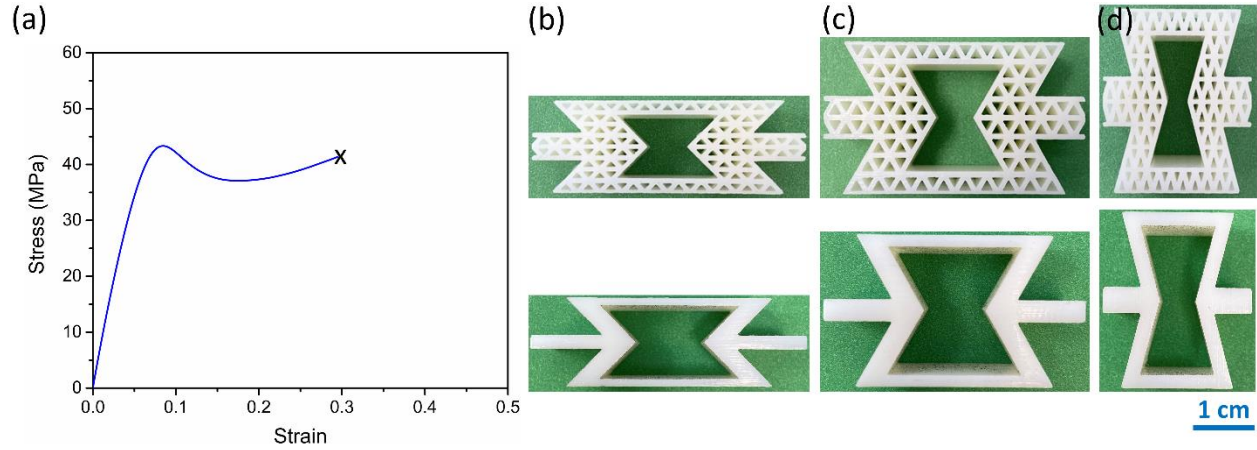


Figure 4.2. (a) Constitutive behavior of the Rigur printing material. (b-d) 3D-printed H-ReH and R-ReH samples with different angles: (b) 45°, (c) 60°, and (d) 75°.

Table 4.1. The characteristics of the designed H-ReH and R-ReH samples ( $\bar{\rho}=0.34$ ) with different angles.

	Angle	$W$ (mm)	$l$ (mm)	$T$ (mm)	$t_t$ (mm)	$l_t$ (mm)
H-ReH	45°	47.82	8.09	15	0.52	2.73
	60°	47.63	11.51	15	0.72	2.73
	75°	23.95	11.31	15	0.49	1.36
	Angle	$W$ (mm)	$l$ (mm)	$T$ (mm)	$t_R$ (mm)	
R-ReH	45°	47.64	9.10	15		3.04
	60°	47.61	13.66	15		3.87
	75°	23.83	12.57	15		2.20

### 4.2.3 Mechanical Testing Coupled with 3D-DIC

The mechanical properties of the 3D printed H-ReH and R-ReH samples with various angle

designs were characterized by quasi-static compressive tests using a universal testing machine (Model 5982, Instron, Corp.) at a constant speed of 3 mm/min. From the measured load-displacement relationships, the stress-strain relationships can be obtained following the relationship:

$$\sigma = F / A \quad (4.1)$$

$$\varepsilon = \delta / h \times 100 \% \quad (4.2)$$

where  $F$  was the external force applied by the Instron machine,  $A$  was the cross-sectional area of the ReH samples,  $\delta$  was the crosshead displacement of Instron machine, and  $h$  was the ReH sample height.

A 3D digital image correlation (3D-DIC) measuring system (Aramis V8, Trilion) was used to measure the strain field evolution of samples during the mechanical tests. Before the DIC measurement, all samples were spray painted of 3 to 7 pixel diameter dots with 50% coverage using flat black general purpose spray paint (Rust-Oleum) for DIC tracking. The high-resolution video was tracked and recorded at a rate of 1 fps. Afterwards, the high-precision deformation contours of each ReH samples during quasi-static compression were computed by the ARAMIS Professional software.

## **4.3 Results and Discussion**

### **4.3.1 Angle effect on the Elastic Behavior of ReHs**

To characterize the mechanical properties of ReHs with different cell-well angle designs, quasi-static compressive tests have been conducted and the stress-strain responses are shown in

Figure 4.3. It is observed that initially both R-ReHs and H-ReHs with different cell-wall angles exhibit an elastic response, followed by a post-buckling behavior. Afterwards, while R-ReHs are terminated early by global fracture, all H-ReHs with different cell-wall angles are terminated in densification mode.

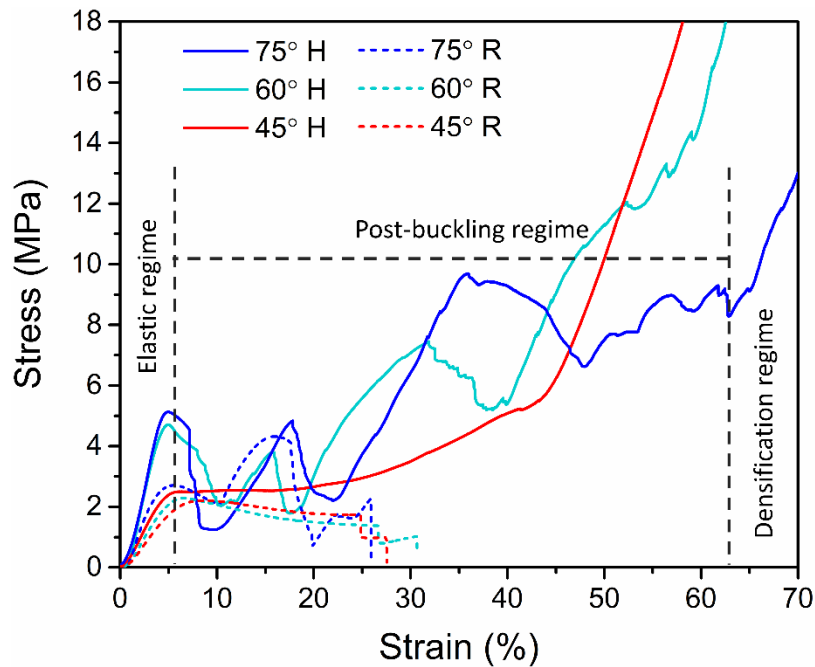


Figure 4.3. Quasi-static compressive response of R- and H-ReHs with three different cell-wall angle designs: 75°, 60° and 45°.

To investigate the initial elastic behavior of R-ReHs and H-ReHs, the negative Poisson's ratio (NPR) effect of R- and H-ReHs with various cell-wall angles are investigated and shown in Figure 4.4. The Poisson's ratios of ReHs are characterized by tracking the movement of the center tips. It is observed that increasing the cell-wall angles will increase NPR effect within elastic region for both R- and H-ReHs, as shown in Figure 4.4 (a). What's more, when increasing the angle from 60

to 75, the increment of NPR effect is more dramatically. This is associated with the angle-dependent deformation mode change, which will be discussed in the following content. For all three cell-wall angles, the NPR effect of R-ReHs is always slightly higher than the H-ReHs. This is because R-ReHs are generally governed by a bending-dominated behavior and lateral displacement is more significant while H-ReHs are governed by a more stretching-dominated behavior [107].

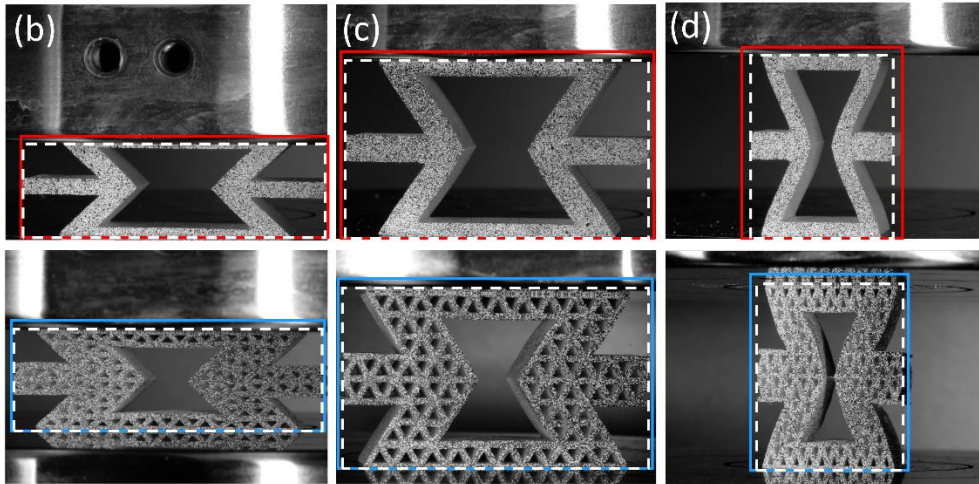
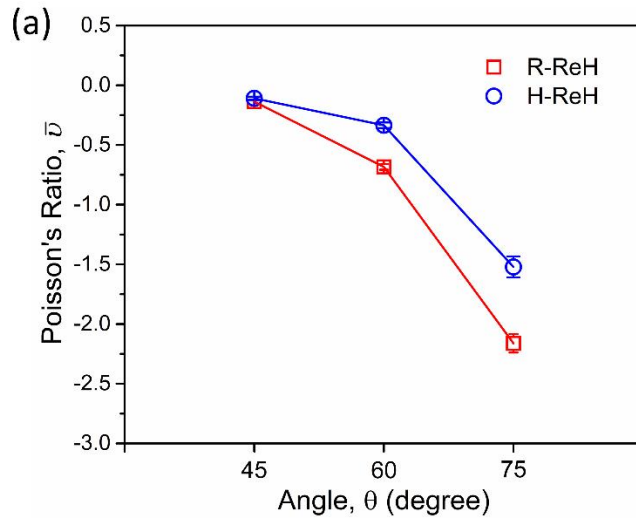


Figure 4.4. The negative Poisson's ratio effect of R- and H-ReHs with different cell-wall angles at  $\epsilon=0.05$ . (a) Poisson's ratio ( $\nu_{xy}$ ) versus cell-wall angles. Experimental images of ReHs: (b) 45°, (c) 60°, and (d) 75°.

In addition, the typical elastic modulus and strength of ReHs with different angles are shown in Figure 4.5 (a) and (b), respectively. For both H-ReHs and R-ReHs, it is evident that the elastic modulus and the strength are increased with increasing the angle. Such trends are logical as more structural components are aligned toward the vertical loading direction. However, H-ReHs exhibit a much greater angle-dependent behavior. To be more specific, H-ReH and R-ReH initially have

similar values of elastic modulus and strength at  $45^\circ$ , when increasing the angle to  $60^\circ$ , the elastic modulus and the strength of H-ReH are significantly enhanced by 120% and 90%, respectively, which is much higher than that of R-ReHs with only 38% and 4% enhancement, respectively. Such significant difference is attributed to the different interaction between the 1<sup>st</sup> order hierarchy and the 2<sup>nd</sup> order triangular hierarchy when increasing the angle of H-ReHs. As the strain fields of inclined members shown in Figure 4.5 (c), when increasing the angle, R-ReHs exhibit similar bending deformation mode on the inclined member. By contrast, the H-ReHs exhibit completely different deformation mode when increasing the angle. In  $45^\circ$  H-ReH, the 2<sup>nd</sup> order triangular hierarchy along the  $45^\circ$  axial direction shows stress concentration near the joints. In addition, the 1<sup>st</sup> order hierarchy (the inclined member) is not effectively carrying the compressive loading along the  $45^\circ$  axial direction, as the strain field only shows small area of compression. Therefore, the interaction between 1<sup>st</sup> and 2<sup>nd</sup> order hierarchy in  $45^\circ$  H-ReH is far from ideal. However, when increases the angle to  $60^\circ$ , the 2<sup>nd</sup> order hierarchy has a more continuous strain field distribution along the  $60^\circ$  axial direction (as highlighted) without stress concentration near the joints, and the 1<sup>st</sup> order hierarchy has increased area of compression. This demonstrates an enhanced interaction between 1<sup>st</sup> order and 2<sup>nd</sup> order hierarchy, and results in a significant enhancement on the elastic modulus and strength. When further increase the angle to  $75^\circ$ , further increased area of compression in 2<sup>nd</sup> order hierarchy of  $75^\circ$  H-ReH is observed, as highlighted. This is due to the increased NPR effect in  $75^\circ$  H-ReH (shown in Figure 4.4 (a)), thus leading to greater deformation of inclined member.

In addition to the inclined axial direction, the hierarchical interaction along the horizontal

direction also exhibits enhancement. The strain fields of these H-ReHs along the horizontal direction are shown in Figure 4.5 (d). Due to the NPR effect, the tip joints tend to move inwards horizontally, and the 2<sup>nd</sup> order triangular hierarchy along horizontal direction is under stretching deformation naturally. Particularly, such stretching deformation exhibits an angle-dependent behavior as well. When the angle is 45°, the stretching is localized near the joints of horizontal struts and severe stress concentration can be observed. Once increasing the angle to 60° and 75°, the deformation is more uniformly distributed to the entire part of the horizontal struts. In general, both inclined and horizontal direction strain fields have demonstrated that increasing the angle can increase the interaction between 1<sup>st</sup> order and 2<sup>nd</sup> order hierarchy, which benefits the elastic modulus and strength comparing of the H-ReH.

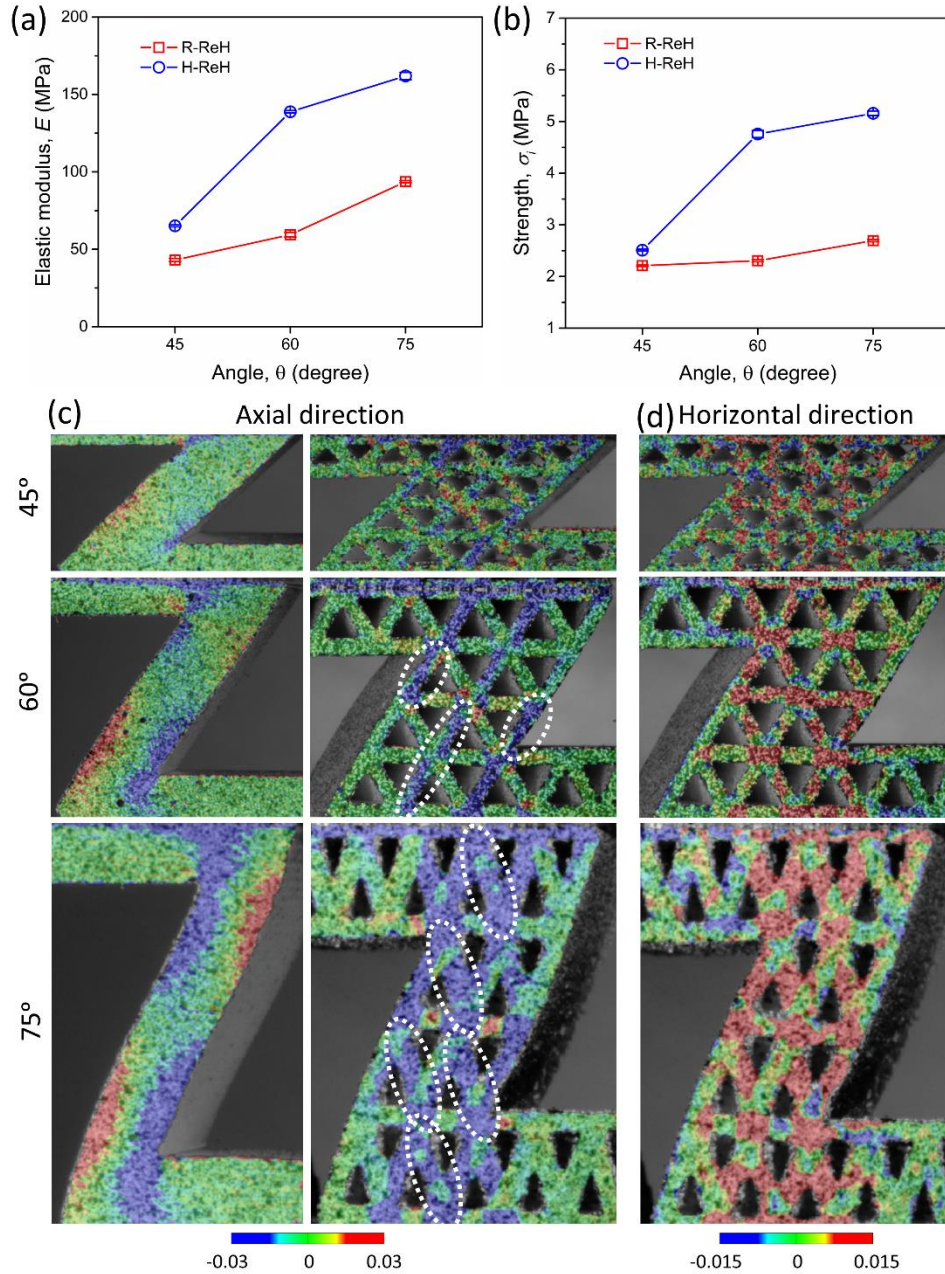


Figure 4.5. Initial elastic behaviors of H-ReHs and R-ReHs with different angles. (a) Elastic modulus, and (b) Strength. DIC strain field in inclined members: (c) alone inclined member axial direction and (d) alone horizontal direction.

For R-ReHs, the elastic collapse of the structure can be analyzed following the Euler–Bernoulli beam theory [155]. Figure 4.6 (a) shows the R-ReH structure under compressive stress

( $\sigma$ ) along  $y$ -direction. Due to the compressive stress, the inclined member of R-ReH exhibit a bending deformation, as shown in Figure 4.6 (b). The force applied in the inclined member ( $F$ ) due to the compressive stress ( $\sigma$ ) can be calculated as:

$$F = \frac{\sigma w T}{2} \quad (4.3)$$

where  $w$  is the width of the horizontal member,  $T$  is the out-of-plane thickness of the R-ReH sample. Since the inclined member is in equilibrium, the force along  $y$ -direction is zero. Therefore, a moment ( $M$ ) will be generated in the inclined member and can be calculated as:

$$M = \frac{F l \cos \theta}{2} \quad (4.4)$$

where  $\theta$  is the angle between horizontal and inclined members,  $l$  is the length of the inclined member. The deflection of the inclined member ( $\delta$ ) can be expressed by:

$$\delta = \frac{M l^2}{6 E_R I} \quad (4.5)$$

where  $E_R$  is the Young's modulus of the printing material, and  $I$  is the second moment of inertia of the inclined member and equals to  $\frac{T \cdot t_R^3}{12}$ , where  $t_R$  is the thickness of the inclined member. Afterwards, the strain of the R-ReH along  $y$ -direction can be calculated as:

$$\varepsilon = \frac{2 \delta \cos \theta}{2 l \sin \theta} \quad (4.6)$$

Since the elastic modulus ( $E$ ) of R-ReH structure is:

$$E = \frac{\sigma}{\varepsilon} \quad (4.7)$$

therefore, by substituting Eqs (4.3-4.6) into the elastic modulus Eqs (4.7) and rearranging, the final expression of elastic modulus ( $E$ ) of R-ReH can be obtained as:

$$E = \frac{2 E_R \cdot t_R^3 \sin \theta}{w l^2 \cos^2 \theta} \quad (4.8)$$

From this elastic modulus expression, it is evident that as  $\theta$  increases,  $E$  will increase. Such

trend is consistent with the result shown in Figure 4.5 (a). Following the expression, the theoretical values of  $E$  are calculated and summarized in Table 4.2. Generally, the theoretical values of  $E$  are in good agreement to the experimental results, although  $45^\circ$  R-ReH has a slight discrepancy. The difference could be because part of vertical deformation applied by the compressive loading is carried by the horizontal member in  $45^\circ$  R-ReH, as  $45^\circ$  R-ReH has the longest horizontal member, which results in a relatively smaller vertical deformation and thus a greater value of experimental  $E$ . Nevertheless, the theoretical result here is a useful tool for the prediction of elastic modulus variation of R-ReHs when angle changes.

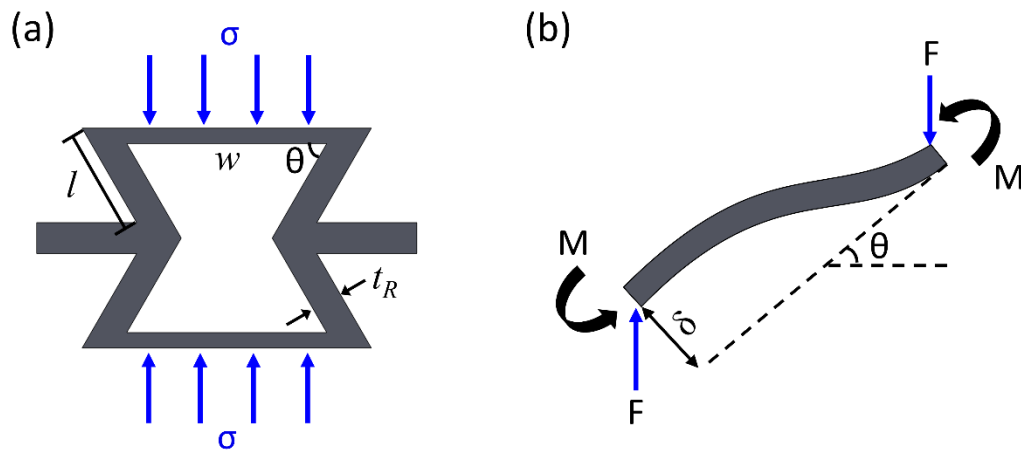


Figure 4.6. (a) R-ReH structure under compressive loading, and (b) free body diagram of the inclined member in R-ReH under loading.

Table 4.2. Theoretical and experimental elastic modulus of R-ReH with different angles.

Angle	$l$ (mm)	$w$ (mm)	$t_R$ (mm)	Theoretical $E$ (MPa)	Experimental $E$ (MPa)
75°	12.57	15.71	2.20	90.82	93.66
60°	13.66	31.75	3.87	50.00	59.4
45°	9.10	24.84	3.04	28.4	43.07

### 4.3.2 Angle effect on the post-buckling behavior of ReHs

After the initial elastic region, it is found that the cell wall angle variations also have effects on the post-buckling behavior of R-ReHs and H-ReHs, respectively. As shown in Figure 4.7 (a), for R-ReHs, both 45° and 60° sample exhibit a stress plateau after the elastic region, while the 75° sample shows a sudden jump. The stress plateaus of 45° and 60° R-ReHs are associated with the bending and rotation of the inclined members in the structure, as shown in the stage 2 of Figure 4.7 (c), and stage b of Figure 4.7 (d), respectively. It is also observed that 45° sample has a slightly higher stress plateau with less stress drop over the 60° sample, this is because the 45° ReH has less rotation on the inclined members comparing with the 60° ReH. As highlighted in the red circles in Figure 4.7 (c), increasing the angle from 45° to 60° will increase the shear force around the joints between horizontal and inclined members, leading to the rotation of the red highlighted tips as well. On the other hand, unlike 45° and 60° samples, the 75° sample shows a sudden stress jump starting from stage II on the stress-strain curves. This is associated with the contact of center tips of the 75° ReH (highlighted in Figure 4.7 (e) stage II). Due to the NPR effect, the inclined members

tend to rotate and bend inwards under the compressive loading. Specifically, the 75° sample has the most significant rotation around the tips comparing to 45° and 60° samples, as highlighted in red circle in the Figure 4.7 (e), which results in the contact of the center tips. The contact provides additional support for the structure and leads to the stress jump. In general, the degree of bending and rotation on inclined members are increased when increase the angle of R-ReHs.

After that, it is observed that the post-buckling behavior of R-ReHs are all terminated by the fracture of the inclined members, as shown in the last stage of Figure 4.7 (c-e), respectively. For 45° and 60° sample, they exhibit identical fracture mode with only one fracture point on each member, which is near the center tips of the inclined members due to the bending. Different from that, 75° sample have two fracture points on one inclined member, which leads to complete drop off of the inclined member and poor structural stability. To investigate the relationship between structural stability and cell-wall angles, the termination strain,  $\varepsilon_t$ , is calculated and plotted, as shown in Figure 4.7 (b). It is observed that 45° and 60° R-ReHs have a similar termination strain, while 75° sample have a reduced termination strain due to the severe bending.

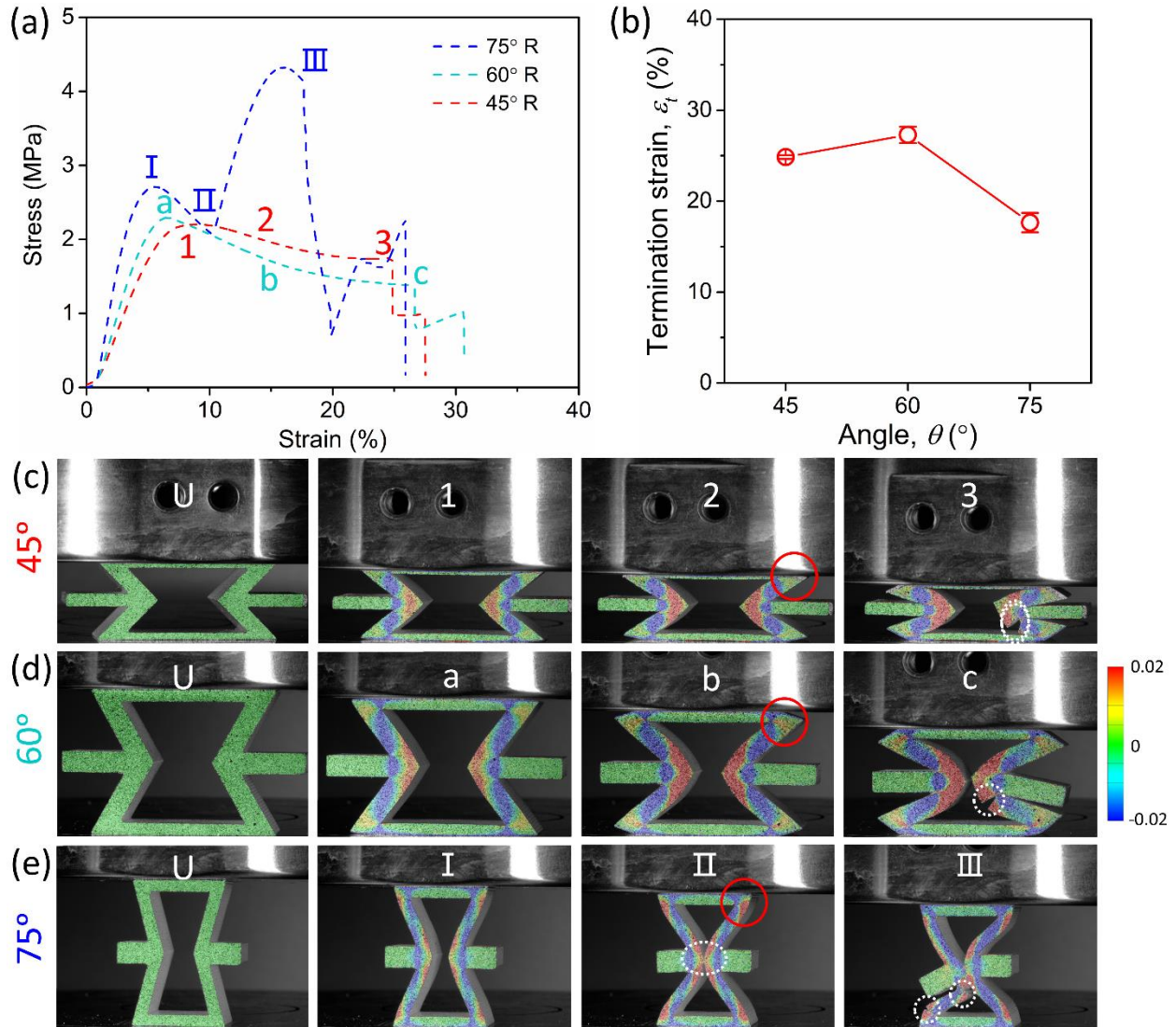


Figure 4.7. Post-buckling behavior of R-ReHs with different angles. (a) stress-strain curves, (b) termination strain, and (c-e) deformation pattern of R-ReHs at various compressive stages: (c) 45°, (d) 60°, and (e) 75°.

For H-ReHs, the post-buckling behavior are completely different from R-ReHs. As shown in Figure 4.8 (a), when the angle value of H-ReHs is relatively high (i.e. 60° and 75°), there are large fluctuations on the post-buckling stress plateaus, while for the lower angle of 45°, a lower stress plateau without fluctuations is observed. These are associated with the deformation mode change

when adjusting the angle of H-ReHs. As shown in Figure 4.8 (c), for 45° H-ReH, the 2<sup>nd</sup> order triangular hierarchy of four inclined members deformed simultaneously, exhibiting a collective deformation process: from the local fracture near the stress-concentrated joints (Figure 4.5 (c)), rotation, to the densification of 2<sup>nd</sup> order struts. However, since the length of inclined member in 45° H-ReH is short, there is barely the deformation of the 1<sup>st</sup> order hierarchy (the whole inclined member), and the densification of inclined members finishes rapidly (shown in stage 2 of Figure 4.8 (c)). Finally, once all of the 2<sup>nd</sup> order triangular hierarchy in inclined members are densified, 45° H-ReH reach its densification region (stage 3).

By contrast, when increasing the angle to 60°, the H-ReH exhibits a localized, stepwise deformation mode. As shown in Figure 4.8 (d), initially at stage *a*, the 2<sup>nd</sup> order triangular hierarchy on the top two inclined members (highlighted) exhibits a progressive process of local buckling, fracture and densification behavior. In the meantime, the 1<sup>st</sup> order hierarchy, the inclined member as a whole, exhibit a first fracture and then contact with the horizontal members in the meantime. This is associated with first stress fluctuation around the position *a* on the stress-strain curve. Once contact, additional support helps the stress to go up again. Afterwards, the 2<sup>nd</sup> step of deformation mode is coming, as shown in stage *b*. The 2<sup>nd</sup> order triangular hierarchy on bottom two inclined members (highlighted) as well as the 1<sup>st</sup> order hierarchy itself exhibit a same local and global deformation behavior respectively. This is associated with second stress fluctuation on the position *b* of the stress-strain curve. As a result, the 60° H-ReH forms a symmetric pattern overall and the structural stability is retained. Please note this is different from 45° H-ReH where 1<sup>st</sup> order hierarchy barely deformed. Thanks to the effective deformation of the 1<sup>st</sup> order hierarchy, the 60°

H-ReH obtains a higher stress plateau from additional support and an extended stress plateau by avoiding global catastrophic failure of R-ReHs. Finally, the 3<sup>rd</sup> step of deformation mode is shown in stage *c*. It is observed that there are four shear bands formed along the previously crashed 2<sup>nd</sup> order triangular hierarchy (highlighted), after which the rest of 2<sup>nd</sup> order triangular hierarchy starts to be crashed and densified. These deformation modes are responsible for the 3<sup>rd</sup> stress trough on the position *c* of the stress-strain curve. Lastly, 60° H-ReH reaches the densification region once all the 2<sup>nd</sup> order hierarchy is compacted.

Similarly, 75° H-ReH also exhibits a stepwise deformation mode and a similar fluctuated stress-strain curves with 60° H-ReH. However, the fracture of 75° H-ReH exhibits an asymmetric pattern. As shown in Figure 4.8 (e), firstly the local buckling, fracture and densification of the 2<sup>nd</sup> order triangular hierarchy, together with fracture and contact of 1<sup>st</sup> order hierarchy, are observed on the top-left and bottom-right region of the inclined members, as shown in stage *I*. Such deformation mode is associated with the stress trough on the position *I* of the stress-strain curve. Afterwards, the same process happens on the top-right and bottom-left region of inclined members, which is associated with the stress trough on the position *II* of the stress-strain curve. Different from 60° H-ReH, the asymmetric deformation pattern in 75° H-ReH is induced by the slight contact of center tips due to the NPR effect. However, thanks to the excellent structural stability, the 75° H-ReH shrinks transversely into a compacted rectangular shape, and exhibits an overall symmetric deformation pattern after the first two steps of deformation, as shown in the stage *II* of Figure 4.8 (e). Following that, there are shear bands formed similar to 60° H-ReH (highlighted in stage *III* in Figure 4.8 (e)), which corresponds to the third stress trough at position *III* on the stress-

strain curve. At last, the rest of uncrashed 2<sup>nd</sup> order triangular hierarchy undergoes compression and an overall densification is reached. It is noted that the degree of fluctuation for 75° H-ReH is slightly larger than the 60° H-ReH. This is because the geometrical components are aligned closer to the vertical loading direction, and the period between fracture to contact is longer in 75° H-ReH.

It is observed that the stress plateaus of all H-ReHs are terminated by densification, instead of global fracture of R-ReHs. The termination strain,  $\varepsilon_t$ , is calculated at the strain with the maximum absorption efficiency of the structure by following Eqs (4.9) and (4.10):

$$\eta(\varepsilon) = \frac{1}{\sigma(\varepsilon)} \int_0^\varepsilon \sigma(\varepsilon) d\varepsilon \quad (4.9)$$

$$\frac{d\eta(\varepsilon)}{d\varepsilon} = 0, \text{ when } \varepsilon = \varepsilon_t \quad (4.10)$$

Different from R-ReHs, the  $\varepsilon_t$  of H-ReHs exhibit a clear angle-dependent behavior. As shown in Figure 4.8 (b), the  $\varepsilon_t$  increases from 40% to 65% when the angle increases from 45° to 75°. This is because there are more available interspaces between the 2<sup>nd</sup> order hierarchy along the loading direction when increasing the angle, which allows more vertical deformation, thus promotes the termination strain of the structure. This demonstrate that a brittle-to-ductile transition can be achieved by tuning the angle of the H-ReH. What's more, the termination strains of H-ReHs are much greater than that of R-ReHs, i.e. when the cell-wall angle is 75°, there is 275% enhancement on the  $\varepsilon_t$ . This is due to the improved structural stability and the unique deformations of 2<sup>nd</sup> order triangular hierarchy.

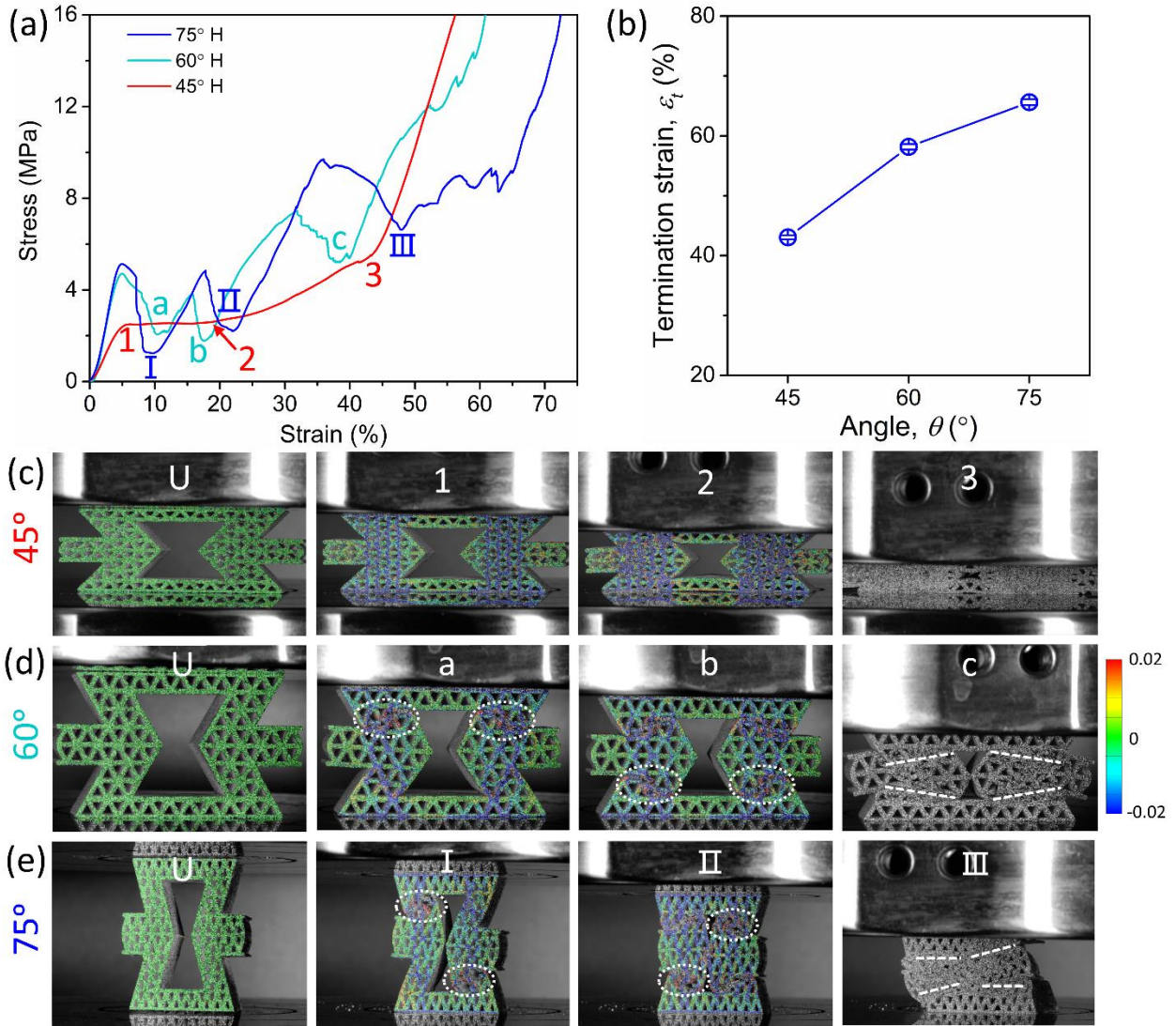


Figure 4.8. Post-buckling behavior of H-ReHs with different angles. (a) stress-strain curves, (b) termination strain, and (c-e) deformation pattern of H-ReHs at various compressive stages: (c) 45°, (d) 60°, and (e) 75°. U means undeformed stage.

### 4.3.3 Angle Effect on Energy Absorption Capacity of ReHs

To evaluate the angle effect on energy absorption capacity of H-ReHs, the specific energy absorption capacity ( $E_s$ ) is calculated by Eqs (4.11):

$$E_s(\varepsilon) = \frac{\int \sigma d\varepsilon}{\rho_R \bar{\rho}} \quad (4.11)$$

where  $\bar{\rho}$  is the relative density of the ReHs structure. As shown in Figure 4.9 (a), for R-ReHs, 45° and 60° sample has a very close growth rate of  $E_s$ . When further increase the angle to 75°, the growth rate of  $E_s$  is effectively enhanced. By contrast, for H-ReHs, the growth rate of  $E_s$  is significantly enhanced when angle is increased from 45° to 60°. Further increase of the angle to 75° will lead to a very similar growth rate of  $E_s$  with 60° H-ReH. It is also observed that with same angle, the H-ReH can always absorb more energy than R-ReH at all strain level. The maximum  $E_s$  of the structure before its failure,  $E_s^{max}$ , is calculated and shown in Figure 4.9 (b). For H-ReHs, when the cell-wall angle is higher (i.e. 60° and 75°), the  $E_s^{max}$  can be significantly enhanced (290% increase) compared to the 45° H-ReH. This is due to the combination of larger termination strain and higher post-buckling stress of the H-ReH at the higher angle. It is also found that the  $E_s^{max}$  of 60° and 75° H-ReHs is close. On the other hand, for R-ReHs, all three angles exhibit a similar  $E_s^{max}$ , which means that changing angle will not have significant effect on the  $E_s^{max}$  of R-ReHs. This is because of the trade-off between increment of stress levels and the reduction of termination strain of the R-ReHs when increases the angle. For higher cell-wall angle, it is noted that H-ReHs will have much higher enhancement on the  $E_s^{max}$  compared with R-ReHs, as of 75°, the  $E_s^{max}$  enhancement can reach 520%. This demonstrates great potential to improve the energy absorption capacity of H-ReHs by tuning the cell-wall angles.

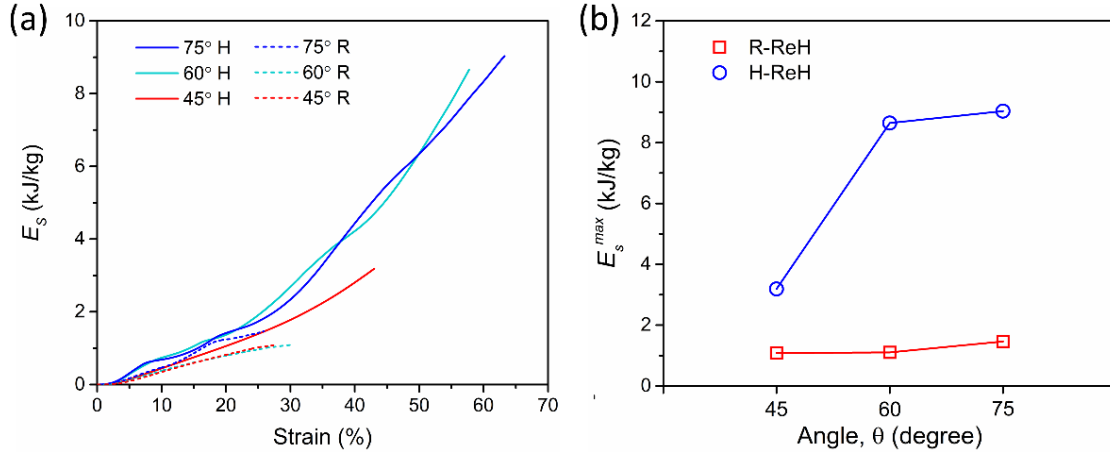


Figure 4.9. (a) Specific energy absorption ( $E_s$ ) of R and H-ReHs with different angles. (b) Maximum specific energy absorption ( $E_s^{max}$ ) of R and H-ReHs as a function of the cell-wall angle.

#### 4.4 Conclusions

The mechanical properties of hierarchical re-entrant honeycombs (H-ReH) with tunable cell-wall angle of 2<sup>nd</sup> order triangular hierarchy are yet to be explored. In this study, a series of H-ReHs and regular re-entrant honeycombs (R-ReHs) with three cell-wall angle designs and same relative density are fabricated and characterized. The effect of cell-wall angles on the compressive behavior of H-ReHs and R-ReHs under quasi-static compression tests have been investigated and compared. In addition, 3D-DIC analyses have been conducted to investigate the deformation mechanism of H-ReHs and R-ReHs with various angles. Finally, the specific energy absorption of ReHs with different angles have been compared. Major findings can be summarized as follows:

- Within the elastic region, for both H-ReHs and R-ReHs, the elastic modulus and the strength are increased with increasing the angle. Interestingly, H-ReHs exhibit a much more angle-dependent behavior on the elastic modulus and the strength than R-ReHs. Such enhancement is found to be associated to the better combined deformation on both 1<sup>st</sup> order

and 2<sup>nd</sup> order hierarchy when increasing the angle. By contrast, R-ReHs have a similar bending deformation regardless of angle changes, and the elastic modulus of R-ReHs follows the prediction of standard beam theory.

- In the post-buckling region, for R-ReHs, increase the angle will adversely result in an earlier termination strain. This is associated with the increased bending and rotation of inclined members and reduced structural stability when increase the angle of R-ReHs. By contrast, H-ReHs exhibit an beneficial angle-dependent post-buckling behavior. When increasing the angle, a transition from a low plateau into a higher fluctuated stress plateau is observed. This is associated with the enhanced effectiveness of both 1<sup>st</sup> order and 2<sup>nd</sup> order hierarchy. What's more, increase the angle significantly enhances the termination strain of H-ReHs. It is noted that H-ReHs with various angles are all terminated by densification instead of fracture.
- The maximum energy absorption capacity for H-ReHs is significantly increased with increasing the angle, while that for R-ReHs is almost inert to the angle change.

Overall, cell-wall angle designs are found to have significant effects on H-ReHs due to the tunable and changeable deformation mode between different hierarchies, while R-ReHs are generally insensitive to angle variations and always dominated by a bending behavior. These findings demonstrate great tunability of H-ReHs through the cell-wall angle design, which shed light on the design of future lightweight hierarchical materials with favorable mechanical performance for targeted applications.

## **CHAPTER 5. STRAIN RATE EFFECT ON THE MECHANICAL PROPERTIES OF 3D-PRINTED HIERARCHICAL RE-ENTRANT HONEYCOMB**

Hierarchical re-entrant honeycombs (H-ReHs) with a 2<sup>nd</sup> order triangular hierarchy, an emerging type of lightweight yet robust materials, have exhibited prominent energy absorption performance under quasi-static compression. However, due to the structural strain rate effect as well as the viscoelastic nature of the printing material, the crushing behavior of H-ReHs under the dynamic loading condition could be completely different from the quasi-static scenario. Therefore, it is necessary to investigate the crushing behavior of H-ReHs under dynamic impacts, the real loading condition in crashworthiness applications. In this chapter, the dynamic responses of H-ReHs are characterized by a drop tower apparatus and compared with the quasi-static responses. For reference, regular re-entrant honeycombs (R-ReHs) are characterized as well. The results show that while R-ReHs exhibit similar post-buckling plateaus under different strain rate, H-ReHs exhibit a unique, two-step post-buckling plateau under dynamic impact, which is different from the quasi-static counterpart. What's more, the linear elastic and the nonlinear post-buckling behaviors of the H-ReHs exhibit different levels of strain rate sensitivity. The strain rate-dependent behaviors are attributed to the micro-inertia effect and the localized deformation modes of the 2<sup>nd</sup> order triangular hierarchy. By contrast, R-ReHs without 2<sup>nd</sup> order hierarchy exhibit no deformation pattern change under different strain rates. Thanks to the combined material strain rate effect and the structural micro-inertia effect, the specific energy absorption capacity of H-ReHs under dynamic impacts can reach one orders of magnitude higher than that of the quasi-static one, and significantly outperforms the R-ReHs. These findings revealed the relationship between the

dynamic crushing behaviors of H-ReHs and the structural heterogeneity of the triangular hierarchy, which provides insights for the design of future lightweight but robust structures for crashworthiness applications.

## 5.1 Introduction

During the past few decades, cellular materials such as foams and honeycombs have been proposed for energy absorption and shock mitigation applications, in order to satisfy the increasing demand on the impact protection in automotive, aerospace, and defense industries [27, 144-146, 192]. Since then, considerable researches have been conducted to investigate the mechanical responses of cellular materials under the quasi-static and dynamic loading conditions [42, 193, 194]. It has been demonstrated that the crushing of cellular materials under dynamic loading conditions is distinctive from the quasi-static one, mainly due to the dominated material strain rate effect and the structural inertia effect [195]. Under the dynamic loading condition, the stress required to crush the cellular materials is much higher than the quasi-static cases, and thus the energy absorption capacity of the cellular materials is significantly enhanced [196, 197]. In addition, the deformation patterns of the cellular materials are completely different under the dynamic loading condition, e.g. significant deformation localization than the quasi-static counterpart has been observed [198-200]. Therefore, it is necessary to investigate and compare both dynamic and quasi-static crushing behaviors of the cellular materials, and reveal the corresponding strain-rate dependent deformation mechanisms.

Recently, auxetic re-entrant honeycombs (ReHs) with inverted cell walls have been

extensively investigated. Due to the unique negative Poisson's ratio effect, ReHs have exhibited superior impact resistance over the conventional honeycombs [99, 153]. However, the mechanical properties of re-entrant honeycomb have not been optimized yet, due to its bending dominated behavior of the ligaments [96]. It has been demonstrated that the hierarchical structure topologies not only have great potential to convert the bending-dominated behavior of cellular materials into the stretching-dominated one, but also exhibit a combination of lightweight and excellent mechanical properties [47, 48, 59]. In light of this, the hierarchical structures have been introduced into the conventional cell walls, and the resulted hierarchical re-entrant honeycombs (H-ReHs) have demonstrated extraordinary mechanical properties [107, 126].

In the previous chapters, we have fabricated H-ReHs with triangular hierarchical substructures through 3D printing technique, and investigated their crushing behavior under the quasi-static compression. The 2<sup>nd</sup> order triangular hierarchy has a unique deformation behavior of elastic stretching, buckling, fracture and densification, which results in a much-enhanced energy absorption capacity over the regular re-entrant honeycombs. On the other hand, the crushing behavior of H-ReHs under the dynamic loading conditions, are yet to be investigated. As the dynamic loading conditions are the real loading conditions for crashworthiness applications, it is necessary to investigate the crushing behaviors of H-ReHs under the dynamic loading conditions. In this chapter, the mechanical responses of H-ReHs under the dynamic impact are investigated and compared with the quasi-static counterpart. It is found that while the stress levels are significantly enhanced for H-ReHs under the dynamic loading condition, the strain rate sensitivity of H-ReHs is different in linear elastic and the nonlinear post-buckling regions, respectively. In

addition, the energy absorption capacity for H-ReHs under the dynamic loading condition is significantly enhanced. These are associated with the micro-inertia effect and the deformation localization of the 2<sup>nd</sup> order triangular hierarchy in H-ReHs under the dynamic impact.

## 5.2 Materials and Methods

The hierarchical re-entrant honeycomb (H-ReH) and regular re-entrant honeycomb (R-ReH) unit cells with three groups of relative densities: 0.17, 0.23 and 0.34 were designed and fabricated in this study, as shown in Figure 5.1 (a-c) respectively. The relative density was adjusted by changing the thickness of the hierarchical struts, namely  $t_l$  of H-ReH and  $t_R$  of R-ReH. The characteristics of H-ReH and R-ReH designs are shown in Table 5.1. The overall dimensions of all H-ReH and R-ReH specimens are the same: width ( $W$ ) 60.4 mm, height ( $h$ ) 35.5 mm, and out of plane thickness 18 mm.

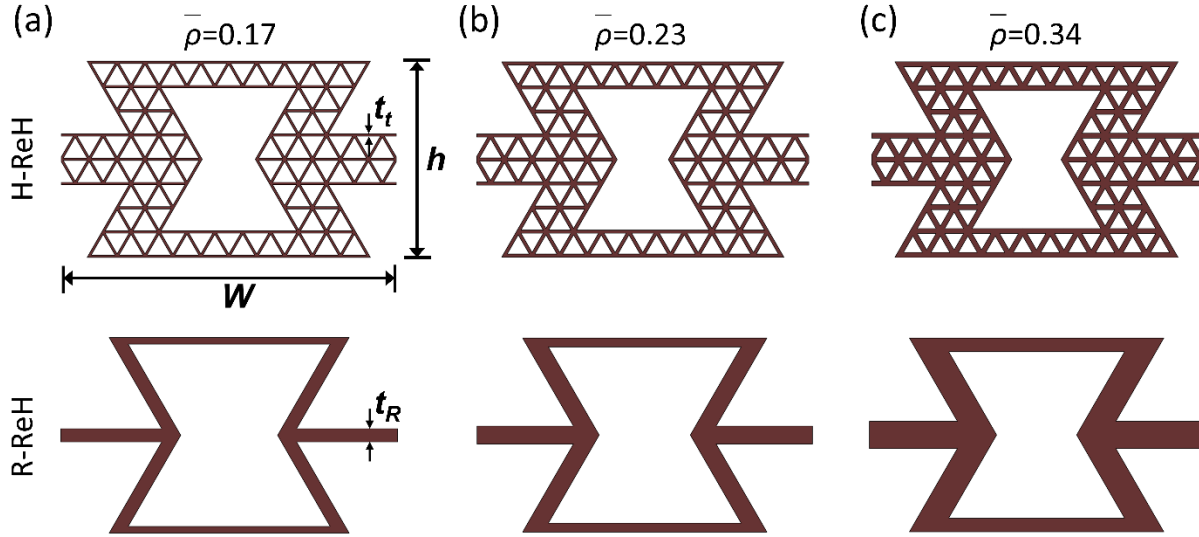


Figure 5.1. Design of H-ReH and R-ReH with different relative densities. (a)  $\bar{\rho} = 0.17$ , (b)  $\bar{\rho} = 0.23$ , and (c)  $\bar{\rho} = 0.34$ .

Table 5.1. Characteristics of designed H-ReH and R-ReH with different relative densities.

	$\bar{\rho}$	$t_t$ (mm)		$\bar{\rho}$	$t_R$ (mm)
	0.17	0.42		0.17	2.4
H-ReH	0.23	0.58	R-ReH	0.23	3.2
	0.34	0.91		0.34	4.9

The H-ReH and R-ReH specimens were fabricated by the Polyject 3D printer (Objet Connex 350, Stratasys). The printing material was mixture of Tangoblack and Verowhite (FLX9870-DM, Stratasys), which was a rubber-like polymer material. The typical printed H-ReH and R-ReH specimens are shown in Figure 5.2 (a). The constitutive behavior of the printing material was first characterized by uniaxial tensile test (ASTM D638-14). The typical constitutive behavior of the printing material is shown in Figure 5.3. The tensile strength was 5.0 MPa, and the elongation at

break was 164%. The mechanical properties of 3D printed H-ReHs were characterized by the quasi-static compression and the dynamic impact tests. For the quasi-static compression tests, a universal test machine (Model 5982, Instron) was used with a constant loading rate of 9 mm/min. The applied stress was calculated as  $\sigma = F / A$ , where  $F$  was the force applied by the Instron crosshead and  $A$  was the cross-sectional area of the 3D-printed H-ReH. The nominal strain was calculated as  $\varepsilon = \delta / h \times 100 \%$ , where  $\delta$  was the Instron machine crosshead displacement, and  $h$  was the initial height of the sample. Specific energy absorption (SEA) of H-ReHs was calculated as  $SEA = \frac{\int F d\delta}{m}$ , where  $m$  was the mass of the H-ReH specimen. For the dynamic impact tests, a customized drop tower apparatus at the Ford Motor Company was used. Figure. 5.2 (b) shows the schematic of the drop tower setup. The incident speed of the dynamic tests was 2.5 m/s and the corresponding free drop height was set as 0.32 m. The drop weight was 8.8 kg. The deceleration time-history was collected by an accelerometer attached to the drop weight, and then recorded by an oscilloscope (PXIe-5105, National Instruments) at a sampling rate of  $10^6$  Hz. The stress applied to the H-ReH specimen was calculated as  $\sigma = m_d \cdot a / A$ , where  $m_d$  was the drop weight and  $a$  was the deceleration of the drop weight. The displacement was calculated as  $\delta = \iint a(t) dt^2$ , where  $t$  was the time [201]. The displacement was then converted to the strain of H-ReH by using the sample height.

During the dynamic impact tests, a high-speed camera (Chronos 1.4, Kron Technologies Inc.) was used to capture the local deformation of the H-ReHs at a frame rate of 5903 fps and a resolution of  $640 \times 360$ . To analyze the local deformation of H-ReHs under the dynamic impact, digital image correlation technique was employed. All 3D printed H-ReH specimens were firstly spray

Painted with white 3-7 pixel size surface patterns (flat white, Rust-Oleum) for tracking [107]. After that, the high-speed videos recording the deformation process of H-ReHs during the dynamic impact were collected for the DIC analyses. By importing the high-speed videos into the DIC processing software (Aramis Professional 2019, GOM Company), the deformation contours of the H-ReHs under the dynamic impact were obtained and analyzed.

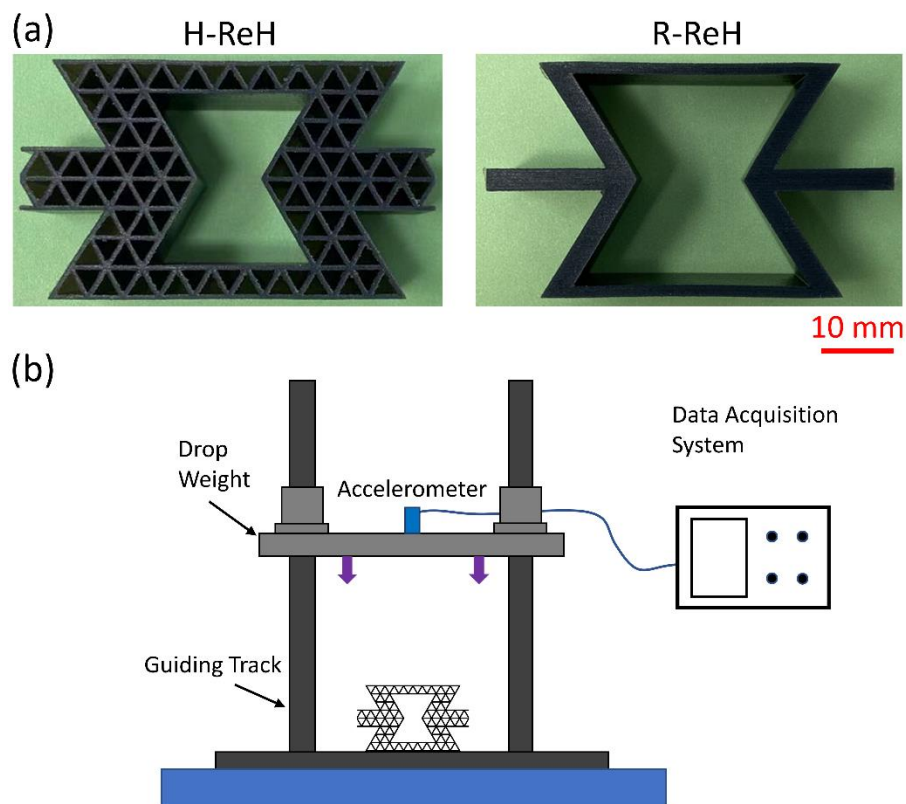


Figure 5.2. (a) 3D printed H-ReH and R-ReH ( $\bar{\rho} = 0.23$ ). (b) Schematic of the experimental set-up of the drop tower tests.

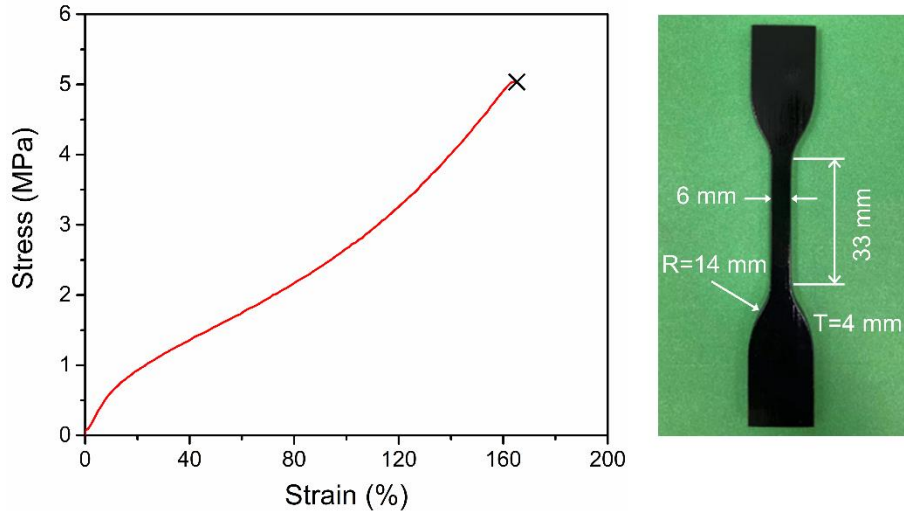


Figure 5.3. Standardized uniaxial tensile testing result of the printing material.

## 5.3 Results and Discussion

### 5.3.1 Dynamic and Quasi-static Responses of H-ReHs

The dynamic responses of H-ReHs and R-ReHs with different relative density are shown in Figure 5.4 (a). It is observed that both H-ReHs and R-ReHs exhibit an elastic response initially. The elastic modulus and the strength of H-ReHs and R-ReHs under the dynamic impact are summarized in Table 5.1. With all the relative densities, it is observed that both the elastic modulus and the strength of the H-ReHs are significantly higher than the R-ReHs. For example, when  $\bar{\rho} = 0.23$ , the strength of H-ReH can reach 5 times of the R-ReH under the dynamic impact conditions. This is associated with the unique deformation mode of H-ReH endowed by the 2<sup>nd</sup> order hierarchy, which outperforms the bending behavior of R-ReH [107].

After the elastic response of the structure, post-buckling plateaus are observed for both H-ReHs and R-ReHs. While for R-ReHs the post-buckling behavior is a one-step plateau with lower

stress level, the post-buckling behavior for H-ReHs exhibit a much higher, two-step plateau, which is associated with the localized progressive deformation of the 2<sup>nd</sup> order triangular hierarchy. The stress level of the post-buckling plateau is increased with increasing the relative density. Finally, all H-ReHs and R-ReHs exhibit a densification behavior. It is observed that the densification strain of R-ReHs is much lower than the H-ReH. For example, when  $\bar{\rho} = 0.34$ , the densification strain is 30% higher for H-ReH. This is associated with the unique local deformation of the 2<sup>nd</sup> order hierarchy in H-ReH, which promotes the overall deformation of H-ReH.

For comparison, the typical stress-strain curves of H-ReHs and R-ReHs under quasi-static compression are shown in Figure 5.4 (b). Generally, all H-ReHs and R-ReHs exhibit a series of linear elastic, nonlinear post-buckling, and densification behaviors. For R-ReHs, the quasi-static responses are similar to that under the dynamic impact, exhibiting a flat post-buckling plateau. By contrast, the post-buckling stress plateaus of H-ReHs under quasi-static compression has significant difference compared with the dynamic impact one. It is observed that while the post-buckling behavior of H-ReH under dynamic impact has a two-step plateau in Figure 5.4 (a), in quasi-static scenario it switches to a one-step increment instead. Therefore, the dynamic impact effectively modify the mechanical responses of H-ReH. In addition, it is noted that the stress level of the dynamic responses is much higher than the quasi-static ones. As shown in Table 5.1 and Table 5.2, the dynamic elastic strength ( $\sigma_d$ ) of H-ReHs are increased significantly by ~5000% compared with the quasi-static elastic strength ( $\sigma_q$ ), with all relative densities from 0.17 to 0.34. Such increment is associated with the strain rate effect and deformation modes change of the H-ReHs under different loading rates.

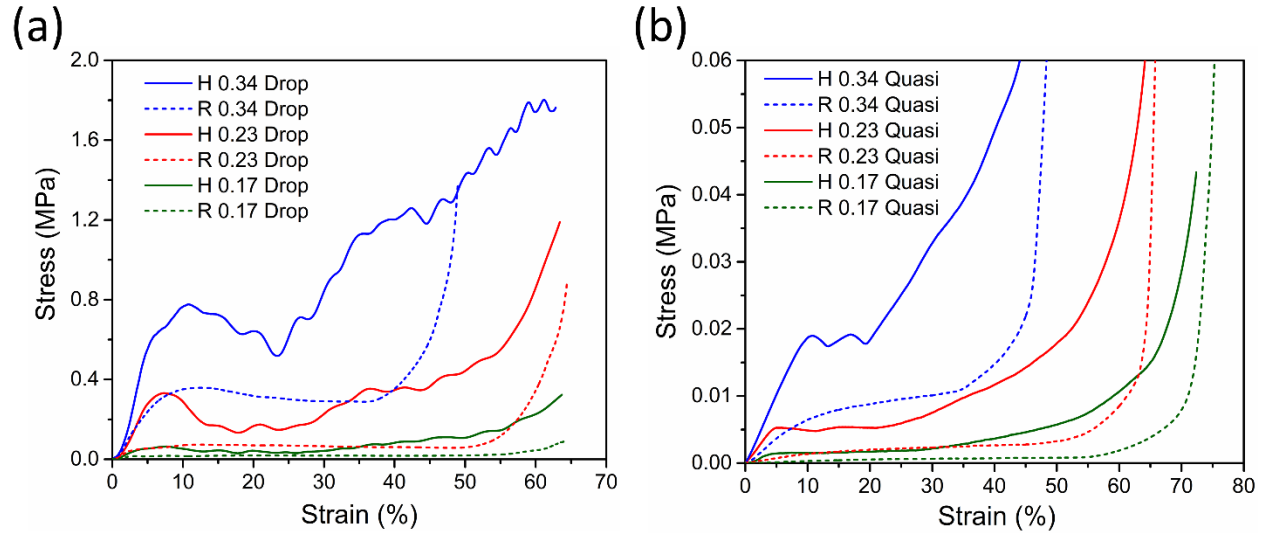


Figure 5.4. Typical stress-strain curves of H-ReHs and R-ReHs with different relative densities under (a) dynamic impact, and (b) quasi-static compression.

Table 5.2. Dynamic elastic modulus ( $E_d$ ) and strength ( $\sigma_d$ ) of H-ReHs and R-ReHs with various relative densities.

	$E_d$ (MPa)	$\sigma_d$ (MPa)
H 0.17	1.78	0.063
R 0.17	0.56	0.016
H 0.23	7.52	0.33
R 0.23	1.67	0.073
H 0.34	16.03	0.78
R 0.34	4.00	0.36

Table 5.3. Quasi-static elastic modulus ( $E_q$ ) and strength ( $\sigma_q$ ) of H-ReHs and R-ReHs with various relative densities.

	$E_q$ (MPa)	$\sigma_q$ (MPa)
H 0.17	0.067	0.0015
R 0.17	0.0030	0.0068
H 0.23	0.13	0.0053
R 0.23	0.015	0.0013
H 0.34	0.21	0.019
R 0.34	0.064	0.00032

In order to directly characterize the strain rate effect of H-ReHs with various relative densities, the dynamic and the quasi-static stress-strain curves for each relative density of H-ReH are plotted together, as shown in Figure 5.5 (a-c). To directly characterize the post-buckling behavior of H-ReHs, the mean crushing stresses are calculated as  $\sigma_m(\varepsilon) = \frac{\int \sigma d\varepsilon}{\varepsilon}$  and plotted in Figure 5.5 as well. The dynamic stress range is 20 times of the quasi-static one for all these figures. As shown in Figure 5.5 (a), for the H-ReH with  $\bar{\rho} = 0.23$ , the dynamic stress-strain curve initially shows a much higher strength in the elastic region compared to the quasi-static curve. Afterwards, a stress drop on the beginning of the post-buckling region is observed. As the strain increases, the dynamic post-buckling plateau is getting closer with the quasi-static one, until reaching the final densification behavior. These results indicates that the linear elastic and the nonlinear post-buckling behaviors of the H-ReHs exhibit different levels of strain rate sensitivity. Similar

behaviors are also observed when the relative density of H-ReHs is  $\bar{\rho} = 0.17$  and  $\bar{\rho} = 0.34$ , respectively, as shown in Figure 5.5 (b) and (c). It is observed that strain rate sensitivity in elastic region are always higher than the post-buckling ones.

To further investigate the strain rate sensitivity of H-ReHs in elastic and post-buckling region, respectively, the elastic strain rate sensitivity ( $S_e$ ) and post-buckling strain rate sensitivity ( $S_p$ ) are calculated, based on the ratios between the dynamic mechanical properties and the quasi-static ones. Firstly, the  $S_e$  of H-ReHs are calculated as Eq (5.1):

$$S_e = E_d / E_q \quad (5.1)$$

where  $E_d$  is the dynamic elastic modulus, and  $E_q$  is the quasi-static elastic modulus of H-ReHs.

Similarly, the  $S_p$  of H-ReHs are calculated as Eq (5.2):

$$S_p = \sigma_{md} / \sigma_{mq} \quad (5.2)$$

where  $\sigma_{md}$  is the dynamic mean stress at 40% strain, and  $\sigma_{mq}$  is the quasi-static mean stress 40% strain (Table 5.3). The resulted  $S_e$  and  $S_p$  are summarized and shown in Table 5.4. It is observed that the value of  $S_e$  is significantly increased with increasing relative density. This demonstrates that the elastic strain rate sensitivity of H-ReHs is strongly dependent on the relative density. By contrast, the  $S_p$  of H-ReHs almost remains constant ( $\sim 30$ ) with increasing relative density of the H-ReHs, as shown in Table 5.4. This, on the other hand, shows that the post-buckling strain rate sensitivity of H-ReHs is much less sensitive to the relative density. Furthermore, by comparing the values of  $S_e$  and  $S_p$  within the same relative density of H-ReHs, it is found that the elastic strain rate sensitivity of H-ReHs is higher than the post-buckling one, which becomes increasingly significant when the relative density is higher. These are associated with the unique dynamic

deformation mechanisms of H-ReHs, which will be discussed in the next section.

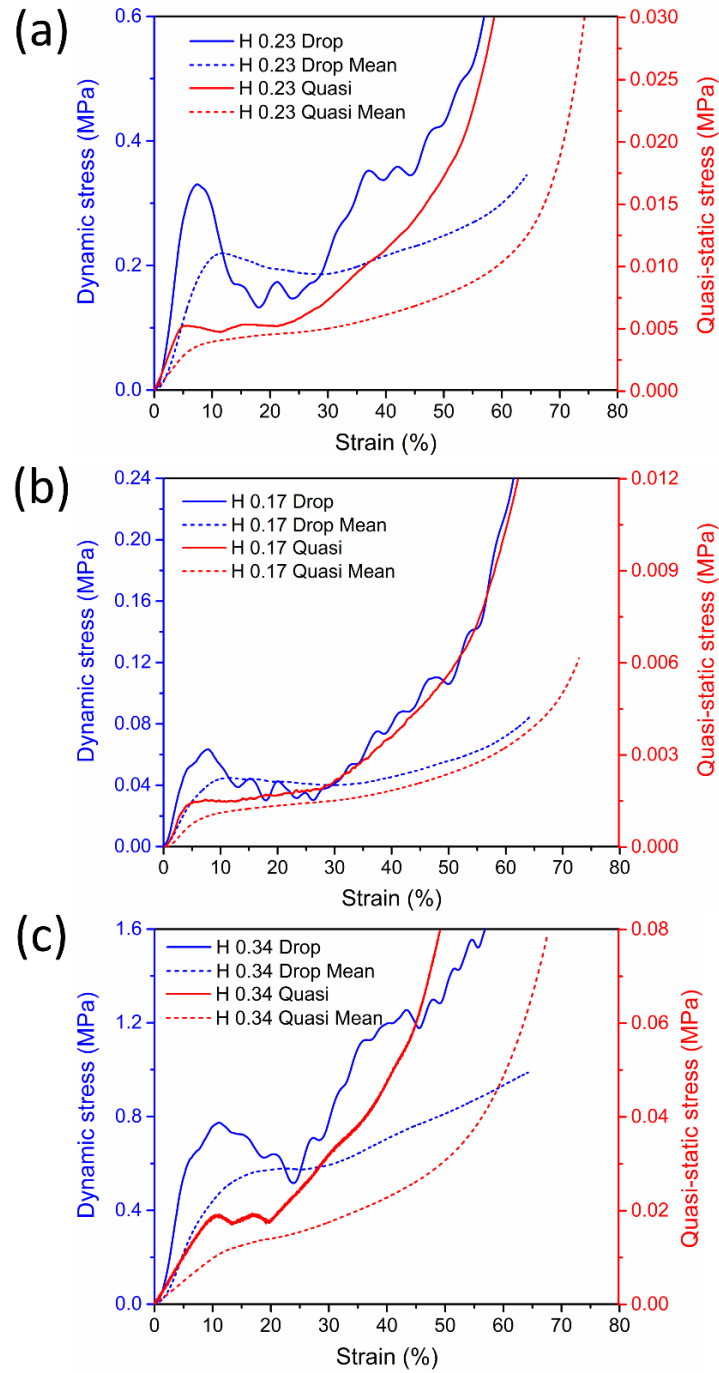


Figure 5.5. Comparison of dynamic and quasi-static stress-strain curves of H-ReHs. (a)  $\bar{\rho} = 0.23$ , (b)  $\bar{\rho} = 0.17$ , and (c)  $\bar{\rho} = 0.34$ .

Table 5.4. Dynamic mean crushing stress ( $\sigma_{md}$ ) and quasi-static mean crushing stress ( $\sigma_{mq}$ ) at  $\varepsilon=40\%$  of H-ReHs.

	$\sigma_{md}$ (MPa)	$\sigma_{mq}$ (MPa)
H 0.17	0.045	0.0018
H 0.23	0.22	0.0061
H 0.34	0.71	0.023

Table 5.5. Elastic strain rate sensitivity ( $S_e$ ) and post-buckling strain rate sensitivity ( $S_p$ ) of H-ReHs.

	$S_e$	$S_p$
H 0.17	26.61	24.67
H 0.23	59.18	35.25
H 0.34	75.63	31.06

### 5.3.2 Dynamic Deformation Mechanisms of H-ReHs

The deformation patterns of H-ReHs under quasi-static and dynamic loading conditions are compared and shown in Figure 5.6. The deformation patterns correspond to four points on the stress-strain curves shown in Figure 5.6 (a). It is observed that at small strain near the end of the elastic region ( $\varepsilon = 7.7\%$ ), the joints and struts of H-ReHs start to deform collectively under the quasi-static compression. By contrast, under the dynamic impact, most of joints and struts are

much less deformed at the same strain level. What's more, localized joints and struts in the corner of H-ReHs are heavily deformed, as highlighted. This unique deformation mode is associated with the micro-inertia effect of the 2<sup>nd</sup> order triangular hierarchy under the dynamic impact, which resists the buckling and rotation of the local struts. Such micro-inertia effect suppresses the compliant buckling of struts under the quasi-static condition [202], thus not only leading to a higher yield strain of H-ReH under the dynamic impact (7.2%) comparing with the quasi-static one (4.9%), but also a much-enhanced strain rate sensitivity of H-ReHs in elastic region compared to the post-buckling one, as shown in Tables 5.3 and 5.4. When the strain further increases to  $\varepsilon = 20\%$ , H-ReH under both quasi-static and dynamic impact exhibit a post-buckling plateau. This is associated with the struts in inclined members are heavily deformed, as shown in Figure 5.6 (b-c). However, the nearby struts in horizontal member (as highlighted) exhibits a much less compression under the dynamic impact. This is also associated with the micro-inertia effect inherited from the linear elastic region. As further increases the strain to 37.3%, the stress responses of H-ReH in both quasi-static and dynamic impact are increased. This is associated with the full compression of struts in inclined members, and the initiation of compression of struts highlighted in the central region. However, differences are observed between quasi-static and dynamic impact deformation patterns. While a compliant buckling mode of struts is observed under the quasi-static condition, an irregular buckling mode with counterrotation behaviors of certain struts is observed under the dynamic impact. These accounts for the unique two-step post-buckling behavior of H-ReHs under the dynamic impact, which is different from one-step post-buckling behavior under the quasi-static loading, as shown in Figure 5.6 (a). Lastly, both H-ReHs reach densification with local struts

compacted together when  $\varepsilon = 54\%$ . Therefore, the strain rate has significant effect on the deformation modes of H-ReHs.

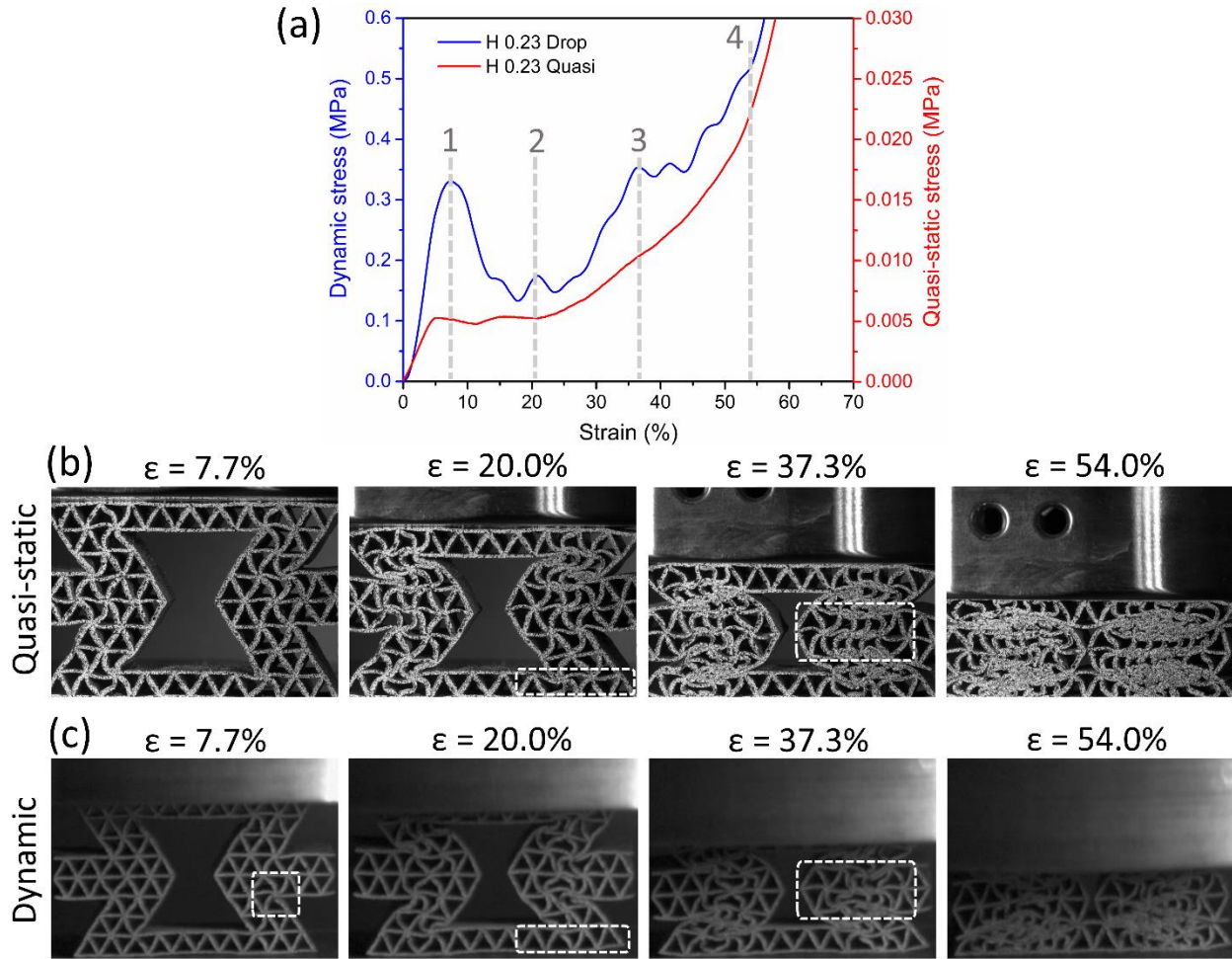


Figure 5.6. The deformation patterns of H-ReH ( $\bar{\rho} = 0.23$ ). (a) Stress-strain curves, (b) deformation under quasi-static compression, and (c) deformation under dynamic impact.

By contrast, for R-ReH the strain rate barely has effects on the deformation patterns. The deformation patterns of R-ReHs under quasi-static and dynamic loading conditions are compared and shown in Figure 5.7. It is observed that R-ReH has very similar deformation patterns when

increasing the strain rate from quasi-static one to dynamic impact one. Initially in elastic region, the R-ReH has center tips moving inwardly due to the NPR effect. As the compression proceeds, the joints connecting horizontal members and inclined members start to rotate, and inclined members exhibit an obvious bending behavior compatible with the further inward movement of center tips. Lastly, when  $\varepsilon = 50\%$ , the inclined members of R-ReH completely contact with the horizontal members, exhibiting a densification behavior. In general, the deformation patterns of R-ReH are independent with the strain rate.

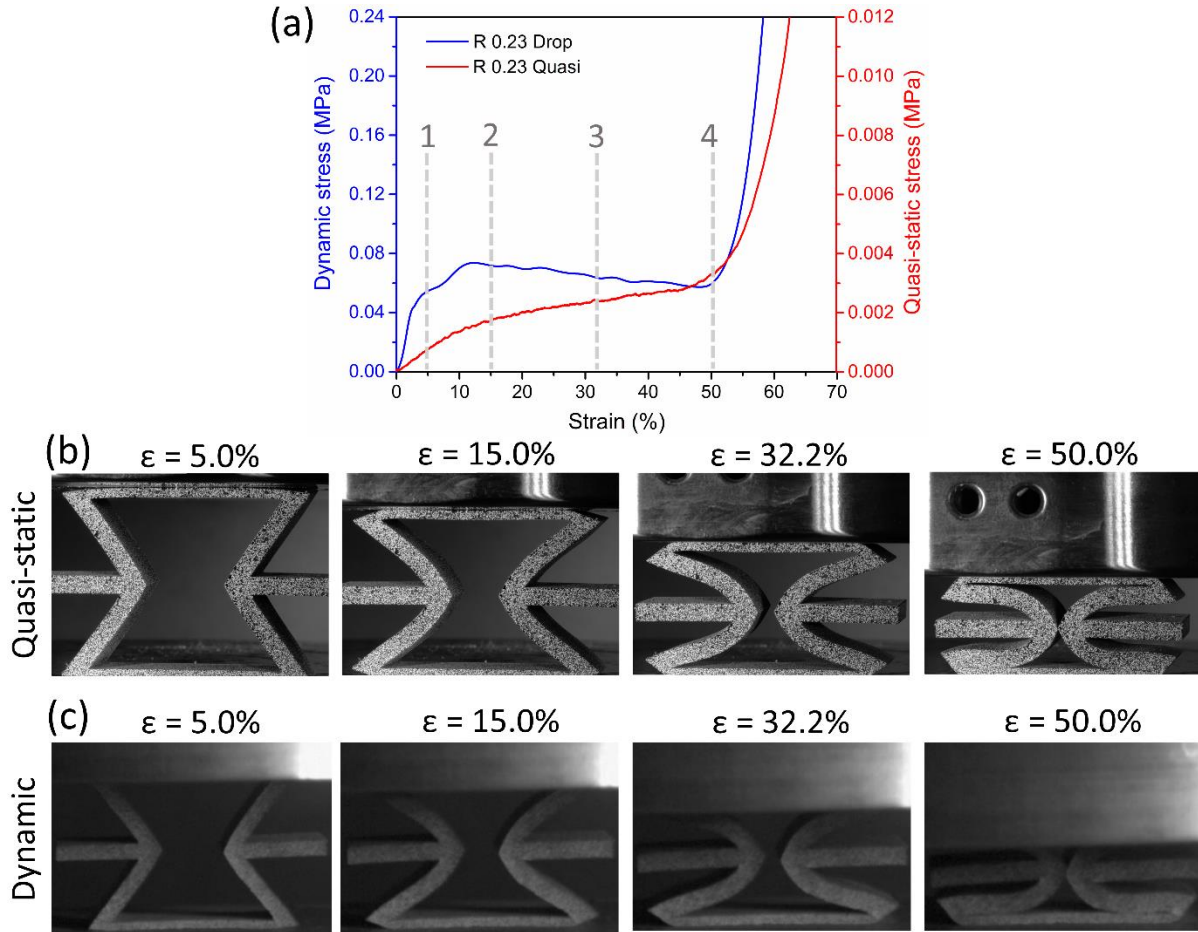


Figure 5.7. The deformation patterns of R-ReH ( $\bar{\rho} = 0.23$ ). (a) Stress-strain curves, (b) deformation under quasi-static compression, and (c) deformation under dynamic impact.

### 5.3.3 Specific Energy Absorption of H-ReHs

The specific energy absorption (SEA) of H-ReHs and R-ReHs under dynamic and quasi-static loading conditions are calculated and shown in Figure 5.8. The SEA values are obtained at the densification strain of each sample. Generally, with increasing the relative density, the SEA of both H-ReHs and R-ReHs are increased. Specifically, under the dynamic loading conditions, it is observed that the SEA of the H-ReHs are always higher than the R-ReHs with same relative density under the dynamic loading conditions, i.e. when  $\bar{\rho} = 0.23$ , H-ReH can have significant 350%

increment of SEA over R-ReH. This is due to the unique local deformation modes and micro-inertia effect endowed by the 2<sup>nd</sup> order hierarchy in H-ReH, which doesn't exist in R-ReHs without the 2<sup>nd</sup> order hierarchy. In addition, under the quasi-static condition, the superior SEA of H-ReHs over R-ReHs are observed for all relative densities as well. These demonstrate that the 2<sup>nd</sup> order triangular hierarchy can effectively enhance the SEA of H-ReH in both dynamic and quasi-static loading conditions. What's more, under the dynamic impact, it is found that H-ReH can absorb an order of magnitude higher mechanical energy over the quasi-static one. Such enhancement is attributed to the additional material strain rate effect together with the micro-inertia effect.

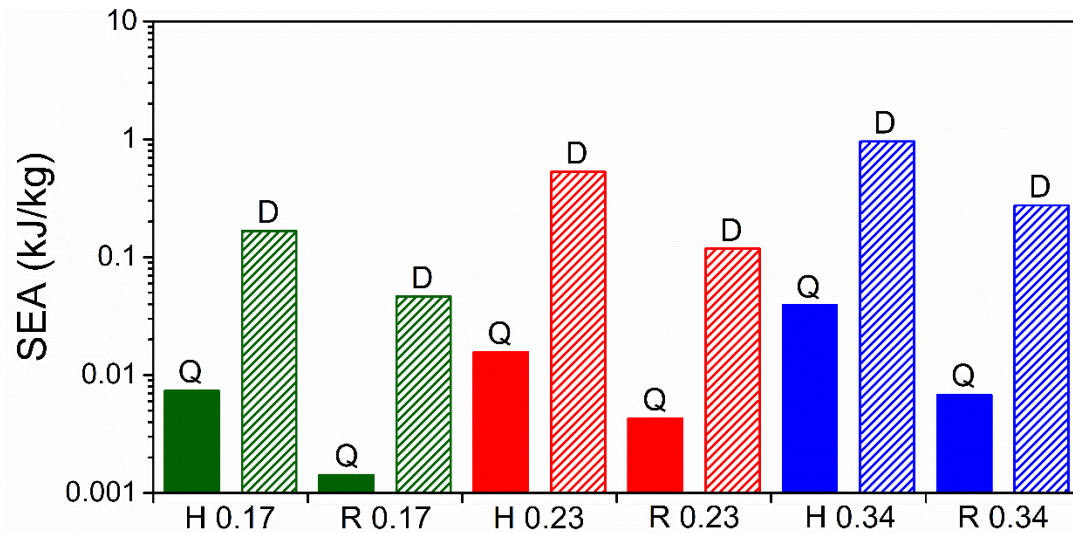


Figure 5.8. SEA of H-ReHs and R-ReHs with different relative density under quasi-static and dynamic loading conditions. (Q is denoted for quasi-static condition, and D is denoted for dynamic condition).

## 5.4 Conclusion

In this study, the mechanical performance of hierarchical re-entrant honeycombs (H-ReHs)

and R-ReHs under both dynamic and quasi-static loading conditions are investigated. Generally, the stress levels are significantly enhanced for both R-ReHs and H-ReHs under the dynamic loading conditions. However, H-ReH exhibit a unique strain rate-dependent post-buckling behavior compared with R-ReH. While R-ReHs exhibit similar one-step post-buckling plateaus under both loading conditions, H-ReHs under dynamic impacts evolves into a unique two-step post-buckling plateau, which is associated with the progressive localized deformation of the 2<sup>nd</sup> order triangular hierarchy. Furthermore, it is found that when the relative density is high, the H-ReHs exhibit a different strain rate sensitivity in linear elastic and the nonlinear post-buckling region respectively. Such difference is due to the micro-inertia effect of 2<sup>nd</sup> order triangular hierarchy in H-ReHs, which results in a localized deformation patterns of H-ReHs under the dynamic impact. By contrast, R-ReHs without 2<sup>nd</sup> order hierarchy exhibit no change on the deformation mode under different strain rates. With the combination of material strain rate effect and the structural micro-inertia effect, the H-ReHs under dynamic impact reach one orders of magnitude higher specific energy absorption (SEA) than the quasi-static one. In addition, the SEA of H-ReHs are significantly outperform the R-ReHs, confirming the effectiveness of the 2<sup>nd</sup> order triangular hierarchy under both dynamic impact and quasi-static loading conditions. These findings can shed light on the design of future lightweight but robust materials for crashworthiness applications.

## **CHAPTER 6. OBLIQUE LOADING EFFECT ON THE CRUSHING BEHAVIORS OF HIERARCHICAL RE-ENTRANT HONEYCOMBS MADE WITH SOFT AND RIGID POLYMERS**

Hierarchical re-entrant honeycombs (H-ReHs) with a stretching-dominated 2<sup>nd</sup> order hierarchy have demonstrated superior energy absorption capacity over regular re-entrant honeycombs (R-ReHs) under the axial loading conditions. However, in real crashing applications, the lightweight energy-absorbing materials not just experience a pure axial or transverse loading. Instead, an off-axial loading with a combination of axial and transverse loading cases, namely the oblique loading, is often the case. Different from the axial loading condition, the oblique loading conditions could strongly affect the mechanical responses of H-ReH. Therefore, it is important to understand the crushing behavior of H-ReHs under oblique loading condition. In this chapter, the quasi-static responses as well as the deformation mechanisms of H-ReHs and R-ReHs subjected to oblique loading have been experimentally investigated. The angle for oblique loading is 15°. The H-ReHs and R-ReHs with different cell-wall angles (45° and 60°) were characterized to investigate the effect of structural design on the oblique crushing behaviors. In addition, two printing materials with different rigidity, i.e. a soft polymer and a rigid polymer, were used to fabricate the H-ReHs and R-ReHs in order to explore the material effect on the crushing behavior under the oblique loading. The results show that the cell-wall angle design strongly affect the oblique crushing behaviors of H-ReHs. 45° H-ReH exhibit a unique enhanced mechanical response under oblique loading comparing with axial loading, while 60° H-ReH exhibit a reduced mechanical response under oblique loading, due to different deformation mechanisms. What's

more, it is found that the oblique crushing behavior and deformation modes of H-ReHs strongly dependent on the rigidity of the constitutive material as well. When fabricated with rigid polymer, 45° H-ReHs has mild rotation with local shear band formation, which outperforms 45° R-ReH that has large rotation due to the plastic hinge formation. This demonstrates a hierarchical structure dominated behavior with rigid matrix material. By contrast, with soft polymer, 45° R-ReH reversely outperforms 45° H-ReH with less rotations due to softer and higher deformability of the matrix material. This, on the other hand, demonstrates hierarchical structure no longer dominates with soft matrix material. These findings provide valuable guidelines for design and material selection of lightweight energy-absorbing materials under complex loading conditions.

## **6.1 Introduction**

Over the past years, cellular materials such as foams and honeycombs have been widely used as energy absorber materials in automotive [144, 203], aerospace [145], packaging [204], and other industries, due to their lightweight nature and excellent energy absorption capacity during the crushing process [146, 205, 206]. The recently developed hierarchical re-entrant honeycombs (H-ReHs), an emerging type of cellular materials with the combination of hierarchical topologies and auxetic behaviors, have shown great potential to replace the conventional cellular materials [107]. It has been demonstrated that under the axial loading condition, H-ReHs exhibit much-enhanced mechanical properties, including specific stiffness, strength, energy absorption, and structural stability over the regular re-entrant honeycombs (R-ReHs), due to the unique deformation mechanism [102, 106, 107].

For a well-designed energy-absorber material, it should be able to absorb maximum energy under various loading cases. Among which, the axial loading condition is only an ideal case. Actually, during a crash process in real complex engineering applications, the energy-absorber materials are not just undergoing net axial loading condition, but more likely subjected to the oblique loading condition at a loading angle, which is a combination of axial compression and shear loading [207]. For example, it is established that in automotive industry, the energy-absorbing bumper system should meet the requirement to be capable of bearing oblique load, as the non-ideal oblique loading condition is an unavoidable common situation [208, 209]. Therefore, it is critical to investigate the behavior of cellular materials under the oblique loading. It is known that the oblique loading can cause significant differences on the crushing behaviors of conventional honeycombs, including loss of energy-absorption capacity [210], and new deformation modes [211]. As for the H-ReHs, with the 2<sup>nd</sup> order hierarchy, both the geometric and constitutive properties should influence the oblique loading behaviors as well. However, existing studies mostly reside in the oblique behaviors of conventional honeycombs [211-214] and R-ReHs [215, 216], while the studies investigating the oblique behaviors of H-ReHs, to the best of our knowledge, is still limited.

In this chapter, the quasi-static oblique responses of H-ReHs and R-ReHs are investigated at a loading angle of 15° and compared with the axial loading case. ReHs with different cell-wall angles design (45° and 60°) were characterized to investigate the effect of structural design. In addition, two printing materials with different constitutive behaviors were used to fabricate the ReHs to explore the material effect. The load-displacement performance and deformation

mechanisms of H-ReHs and R-ReHs are characterized and analyzed in detail.

## 6.2 Materials and Methods

### 6.2.1 Materials and Specimens Preparation

The H-ReHs and R-ReHs with 45° and 60° cell-wall angle designs were investigated for the axial and oblique loading conditions. The design of H-ReHs and R-ReHs with different cell-wall angles are shown in Figure 6.1. The cell-wall angle was determined by the angle between horizontal and inclined structural components ( $\theta$ ). The overall dimension of H-ReHs and R-ReHs were determined by the width ( $W_H$  and  $W_R$ ) the height ( $H_H$  and  $H_R$ ), respectively. Specifically, the triangular hierarchy in H-ReHs were determined by two geometric parameters: length ( $l_i$ ) and thickness ( $t_i$ ), as shown in Figure 6.1 (a). While for R-ReHs, the member dimension was controlled by thickness ( $t_R$ ). For all H-ReHs and R-ReHs, the out of plane thickness was set as 15 mm to avoid out of plane buckling during the testing. All the geometric parameters are summarized in Table 6.1. The relative density of all specimens were maintained constant as 0.34.

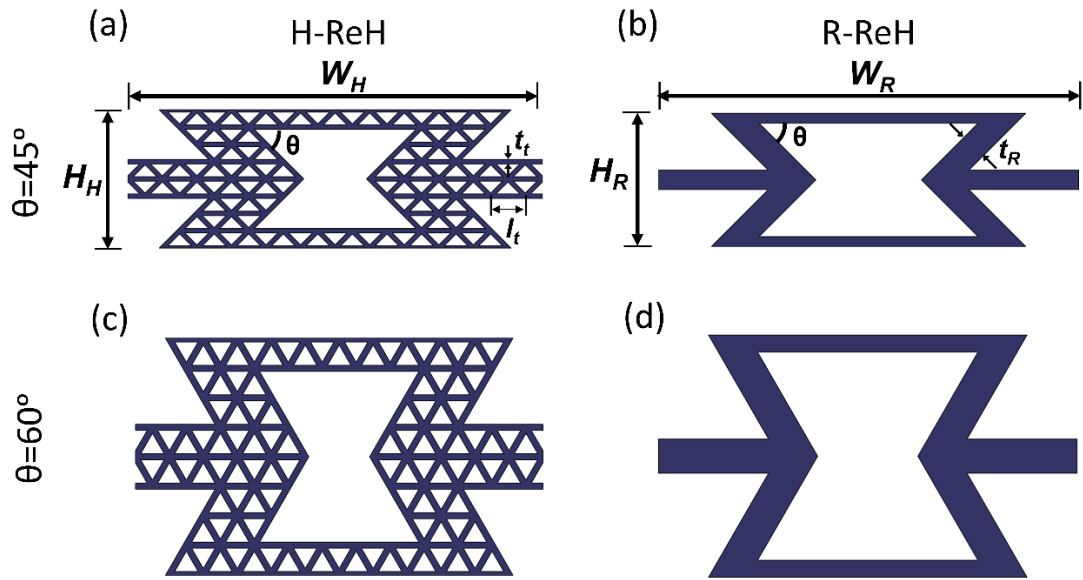


Figure 6.1. Design and configurations of H-ReHs and R-ReHs with  $\bar{\rho}=0.34$ . (a)  $45^\circ$  H-ReH, (b)  $45^\circ$  R-ReH, (c)  $60^\circ$  H-ReH, and (d)  $60^\circ$  R-ReH.

Table 6.1. The characteristics of designed H-ReHs and R-ReHs with different cell-wall angles.

	Angle	$W$ (mm)	$l$ (mm)	$T$ (mm)	$t_t$ (mm)	$l_t$ (mm)
H-ReH	$45^\circ$	47.82	8.09	15	0.52	2.73
	$60^\circ$	47.63	11.51	15	0.72	2.73
	Angle	$W$ (mm)	$l$ (mm)	$T$ (mm)	$t_R$ (mm)	
R-ReH	$45^\circ$	47.64	9.10	15	3.04	
	$60^\circ$	47.61	13.66	15	3.87	

To fabricate the designed H-ReHs and R-ReHs, Polyjet 3D printing technique were used (Objet Connex350, Stratasys). Two photopolymers were used for the printing, one is black, soft

material with good deformability (FLX4895, Stratasys), the other is white, rigid material (Rigur, Stratasys). The specimens fabricated by soft and rigid materials are shown in Figure 6.2 (a-b). It is observed that the printed specimens exhibit good surface quality. The dimensions of specimens are compatible with the 3D DIC measurement during the mechanical testing. The constitutive behaviors of the soft and rigid materials were characterized by ASTM D638-14 uniaxial tensile tests, and results are shown in Figure 6.2 (c-d). For the soft material, the tensile strength is 10.5 MPa, and the elongation at break is 100%. For the rigid material, the Young's modulus is 734.1 MPa, and the tensile strength is 43 MPa. The density of both soft and rigid materials is 1.2 g/cm<sup>3</sup>. During the printing process, the material droplets were jet onto the build tray, which were cured by UV light to solidify. For all specimens, the temperature of the printer extruder was set as 70 °C, while the printer build tray was kept at room temperature. After printing, all specimens were put in the atmosphere condition with room temperature for 9 days to fully cure before the testing.

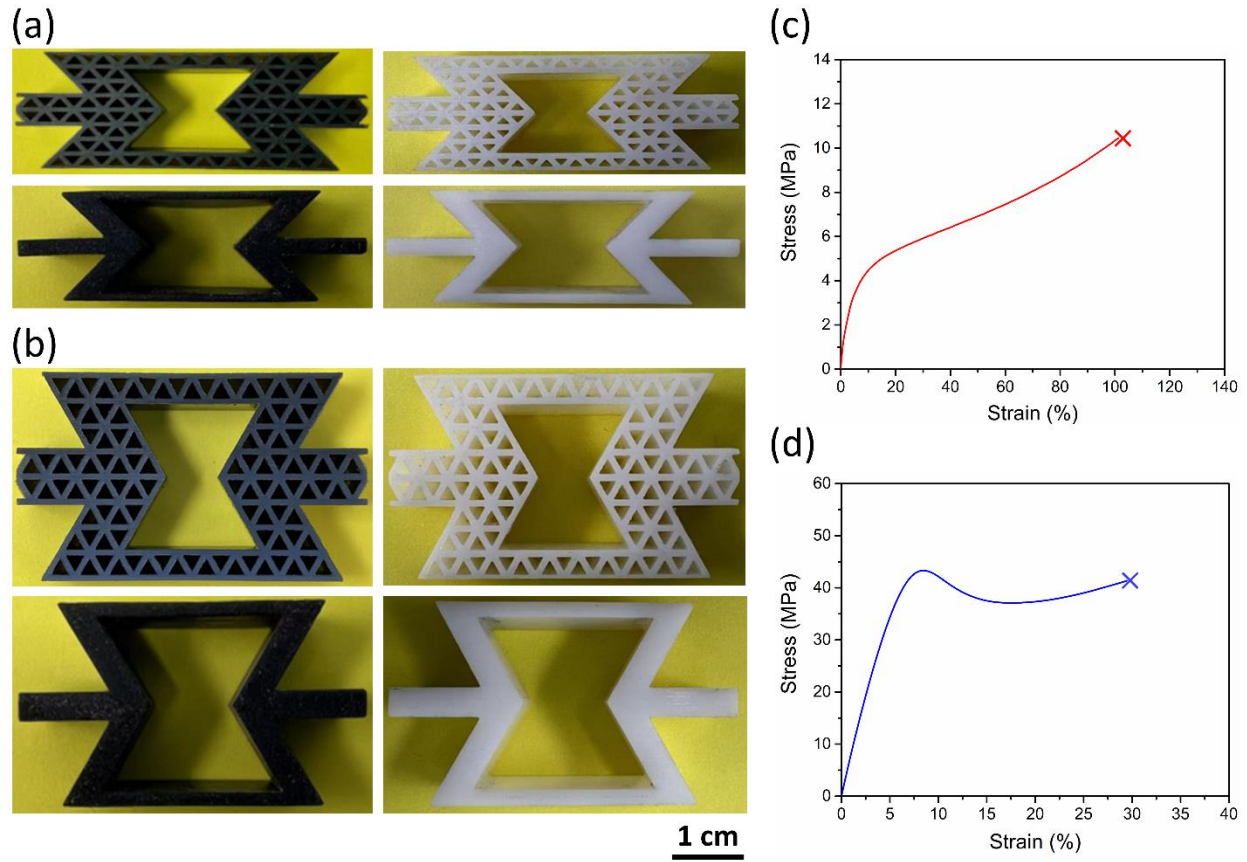


Figure 6.2. (a-b) 3D printed specimens with soft (black) and rigid (white) polymers: (a) Printed 45° H-ReH and 45° R-ReH with soft and rigid polymers. (b) Printed 60° H-ReH and 60° R-ReH with soft and rigid polymers. Constitutive behavior of the printing materials: (c) soft polymer (FLX4895), and (d) rigid polymer (Rigur).

## 6.2.2 Mechanical Testing and 3D-DIC

Quasi-static oblique and axial compressive tests were conducted to characterize H-ReHs and R-ReHs using a universal testing machine (Model 5982, Instron). The experimental setups for oblique loading and axial loading are shown in Figure 6.3. Two wedges with 15° angle are installed and fixed onto both top and bottom Instron platens with bolting, as shown in Figure 6.3 (a). The top and bottom wedges are set to be parallel to each other before the testing. For axial loading, two horizontal platens were used without wedges, as shown in Figure 6.3 (b). The moving speed of top

platen was set as 3 mm/min for both oblique loading and axial loading. In order to fix specimens onto the wedges and platens and avoid sliding during the testing, a strong adhesive tape (F9460PC, 3M) was applied between the wedge surface and the specimen surface. For each ReH design, at least three samples were prepared and tested.

During the quasi-static tests, a 3D digital image correlation (3D-DIC) system (Aramis V8, Trilion) was used to characterize the strain field evolution of specimens during the mechanical tests. Before the measurement, all specimens were speckled with 3 to 7 pixel size dots by using flat black/white spray paint with 50% coverage for DIC tracking purposes. During the measurement, the high-resolution deformation videos were recorded by the system at a rate of 1 fps, which will be analyzed and computed to generate high-precision deformation contours of specimens by using professional DIC software (GOM Correlate Pro, Zeiss).

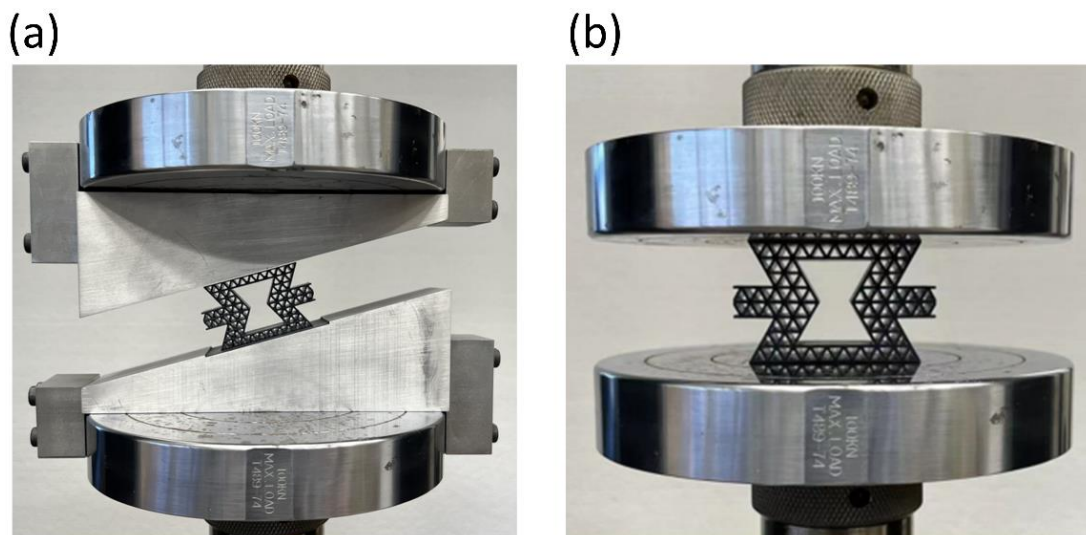


Figure 6.3. Setups for oblique compressive loading and axial loading. (a) Oblique loading with angle of  $15^\circ$ , and (b) axial loading with angle of  $0^\circ$ .

## 6.3 Results and Discussion

### 6.3.1 Constitutive Behavior of ReHs

The mechanical responses of 45° ReHs fabricated with soft and rigid materials under oblique loading and axial loading have been characterized and results are shown in Figure 6.4. As shown in Figure 6.4 (a), when ReHs are fabricated with soft material, it is observed that under oblique loading, both H-ReHs and R-ReHs exhibit a series of elastic region, post-buckling plateau, and densification behaviors, similar to the axial loading curves. For R-ReHs, oblique loading reduced the force response of R-ReHs in elastic and post-buckling regions, which is similar to the existing oblique loading results in current literatures [211]. However, for H-ReHs, the oblique loading uncommonly increased the force response compared with the axial loading condition. This is because of different deformation patterns of H-ReHs and R-ReHs fabricated with soft material under the oblique loading, which will be discussed in the following section. In addition, it is noted that force response in elastic and post-buckling region of R-ReHs unexpectedly outperforms H-ReHs, demonstrating that 2<sup>nd</sup> order hierarchy no longer effectively improves the force responses of R-ReHs. At last, when reaching the densification behavior, the H-ReHs shows much higher displacement value over R-ReHs. This is because the effective local deformation of the 2<sup>nd</sup> order triangular hierarchy in H-ReHs, which promotes the overall deformability of the structure.

By contrast, it is found that force responses of R-ReHs and H-ReHs are strongly dependent on the constitutive material. When the ReHs are fabricated by rigid material, distinctive force responses are observed. As shown in Figure 6.4 (b), the rigid H-ReHs under oblique loading exhibit enhanced force responses over the axial loading, while R-ReHs becomes weaker under the oblique

loading, similar to the soft ReHs cases. What's more, superior force responses of H-ReHs are observed over R-ReHs under both oblique and axial loadings. This demonstrates that the 2<sup>nd</sup> order hierarchy fabricated by rigid material can effectively improve the force response of R-ReHs, which is different from the soft 2<sup>nd</sup> order hierarchy case. In addition, the R-ReHs fractured early and no longer exhibit a densification behavior, while H-ReHs exhibit a densification behavior. This is associated with unique local densification behavior from rigid 2<sup>nd</sup> triangular order hierarchy in H-ReHs, which is in agreement with our previous work [107]. The different mechanical responses of ReHs under oblique loading with material dependent behaviors are associated with the deformation mechanisms.

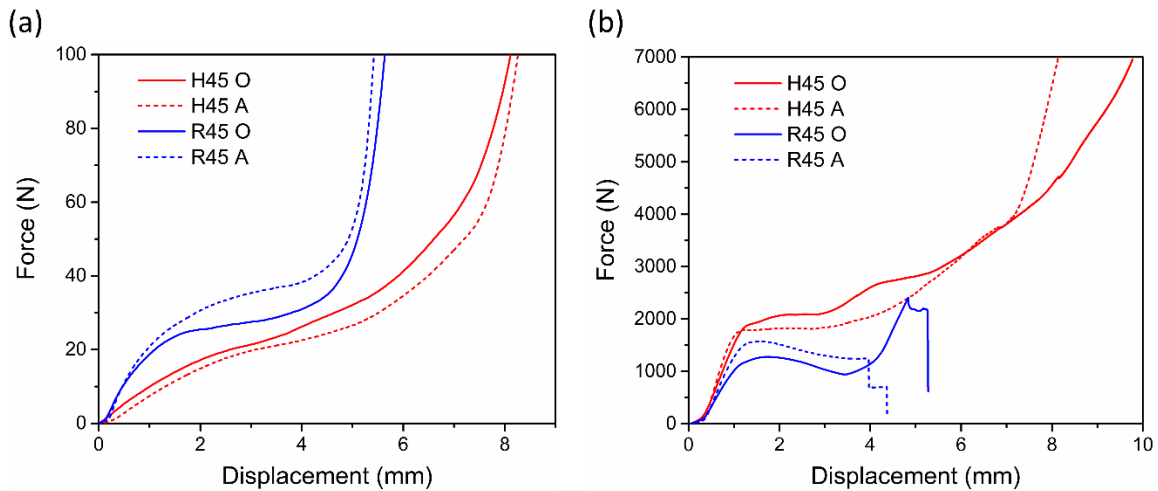


Figure 6.4. Load-displacement curves of 45° ReHs under oblique (15°) and axial (0°) loadings. (a) ReHs fabricated by soft materials (b) ReHs fabricated by rigid materials. (O denoted for oblique loading, and A denoted for axial loading).

The cell wall angle design also has effects on the oblique loading behavior of ReHs. The mechanical responses of 60° ReHs are shown in Figure 6.5. As shown in Figure 6.5 (a), for soft

material fabricated ReHs, it is observed 60° H-ReHs under oblique loading has inferior force response compared to axial loading, while 60° R-ReHs almost has identical force responses independent with loading angles. In addition, the H-ReHs always have higher force response over R-ReHs regardless of oblique loading or axial loading condition. On the other hand, when fabricated with rigid material, the post-buckling behavior changes. H-ReHs have fluctuations on the post-buckling plateaus followed by densification behavior, which is associated with the progressive local fracture and densification of 2<sup>nd</sup> order triangular hierarchy. By contrast, R-ReHs have global fractured and terminated at much lower displacement, due to the brittle nature of the rigid material. Therefore, post-buckling behavior of ReHs under oblique and axial loadings are correlated to the underlying deformation mechanism, which exhibit strong dependency with the constitutive material behavior.

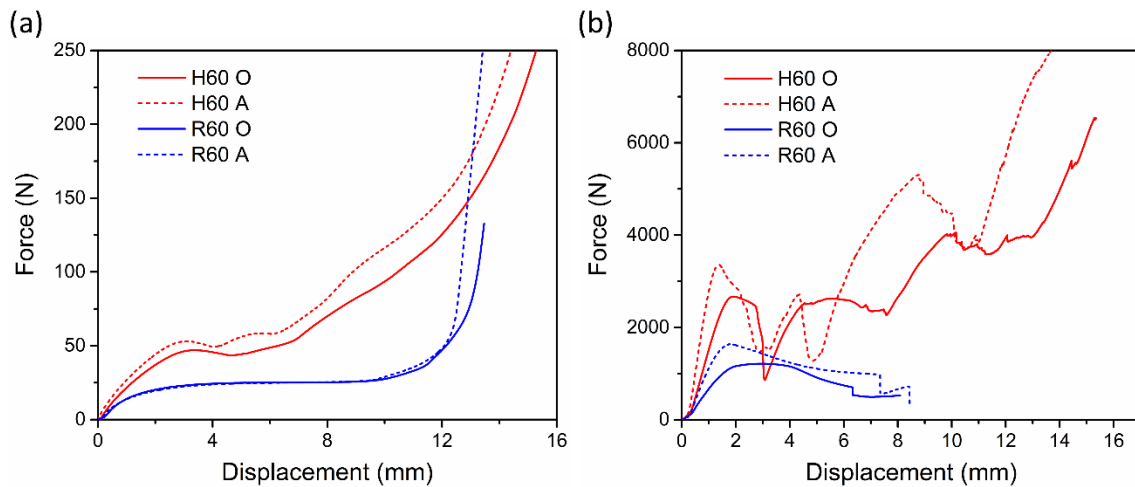


Figure 6.5. Load-displacement curves of 60° ReHs under oblique (15°) and axial (0°) loadings. (a) ReHs fabricated by soft materials (b) ReHs fabricated by rigid materials. (O denoted for oblique loading, and A denoted for axial loading).

### 6.3.2 Deformation Mechanism of ReHs under Oblique Loading

To investigate the deformation mechanism of ReHs under the oblique loading, the negative Poisson's ratio (NPR) effect of both H-ReHs and R-ReHs are characterized first. As shown in Figure 6.6 (a), for 45° ReHs, under the axial loading, R-ReH always exhibit a higher NPR effect than the H-ReH, which agrees with our previous research work [107]. By contrast, under the oblique loading, the NPR effect of R-ReHs are slightly increased compare to the axial ones, while H-ReH is almost insensitive to the loading direction. In addition, the soft R-ReH exhibit a higher NPR effect over the soft H-ReH, while the rigid R-ReH exhibit almost same NPR effect with rigid H-ReH. For 60° ReHs, the NPR effects are more significant than 45° ReHs. Under the axial loading, the R-ReH has an increasingly lower NPR value than the corresponding H-ReH, for both soft and rigid ReHs. By contrast, under the oblique loading, it is noted that while soft ReHs remain the same NPR values with the axial ones, the Rigid ReHs exhibit much reduced NPR values, which is associated with the serious rotation effect of ReHs under the oblique loading. The clear loading direction-dependent behavior and material-dependent behavior of ReHs under the oblique loading are associated with the different deformation mechanisms and will be discussed in the following contents.

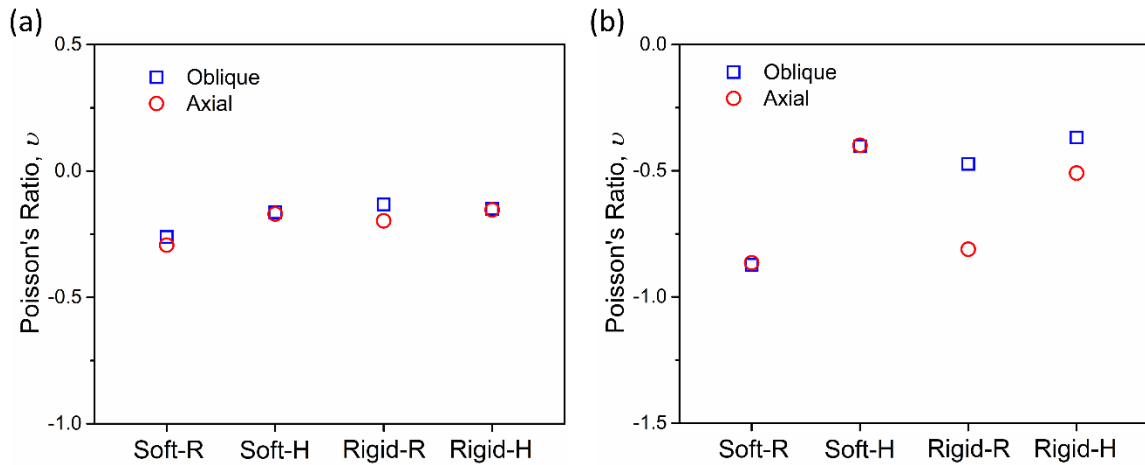


Figure 6.6. Poisson's ratio of H-ReHs and R-ReHs with different cell-wall angles and fabricated with different materials. (a) ReHs with 45° cell wall angle. (b) ReHs with 60° cell wall angle.

It is found that under oblique loading, the ReHs not only has NPR effect, but also has a rotation effect. This is because during the oblique loading, the position of both bottom surface and top surface of the specimen are fixed with the loading wedges, thus with the proceeds of the oblique compression, the off-axis loading will generate additional shear force on the specimen, leading to a rotation effect of the sample, as the left center tips moves upwards, while the right center tips moves downwards, as shown in Figure 6.7.

In order to investigate the rotation effect of ReHs under the oblique loading condition, the rotation effects of ReHs are evaluated by characterizing the center tip distance along the  $y_1$  direction of the specimen at certain compressive displacement. The rotation effects of ReHs fabricated with soft materials are shown in Figure 6.7. It is observed that at same overall compressive displacement, the R-ReH has a slightly smaller tip distance value compared with the H-ReH. This means that the rotation of soft R-ReH is slightly smaller than the H-ReH,

demonstrating that the soft 2<sup>nd</sup> order hierarchy doesn't play significant role on the rotation of the structure under the oblique loading. Thus, for soft ReHs the material effect is dominated, regardless of the structural design. However, when the ReHs are fabricated with rigid material, the ReHs exhibit completely different rotation effects. As shown in Figure 6.8, the R-ReH fabricated with rigid material exhibit much larger tip distance value, which is 3 times of the soft R-ReH shown in Figure 6.7. This is associated with the seriously increased counter rotation of center tips together with the connected inclined members of R-ReH. This demonstrates that switch the material from soft to rigid will significantly increase the rotation on the R-ReH. By contrast, for rigid H-ReH, the tip distance is much smaller than the corresponding rigid R-ReH, as shown in Figure 6.8 (b) and (d). The rotation effect is significantly decreased by 56% for rigid H-ReH compared with the corresponding R-ReH. This, on the other hand, demonstrates that the rigid 2<sup>nd</sup> order triangular hierarchy can effectively reduce the rotation of H-ReH and promote the structural stability under the oblique loading. In such case, the structural effect is dominated for the rigid ReHs. Therefore, the crushing behavior of ReHs under oblique loading are strongly dependent on both the constitutive behavior of the material and the structural effect.

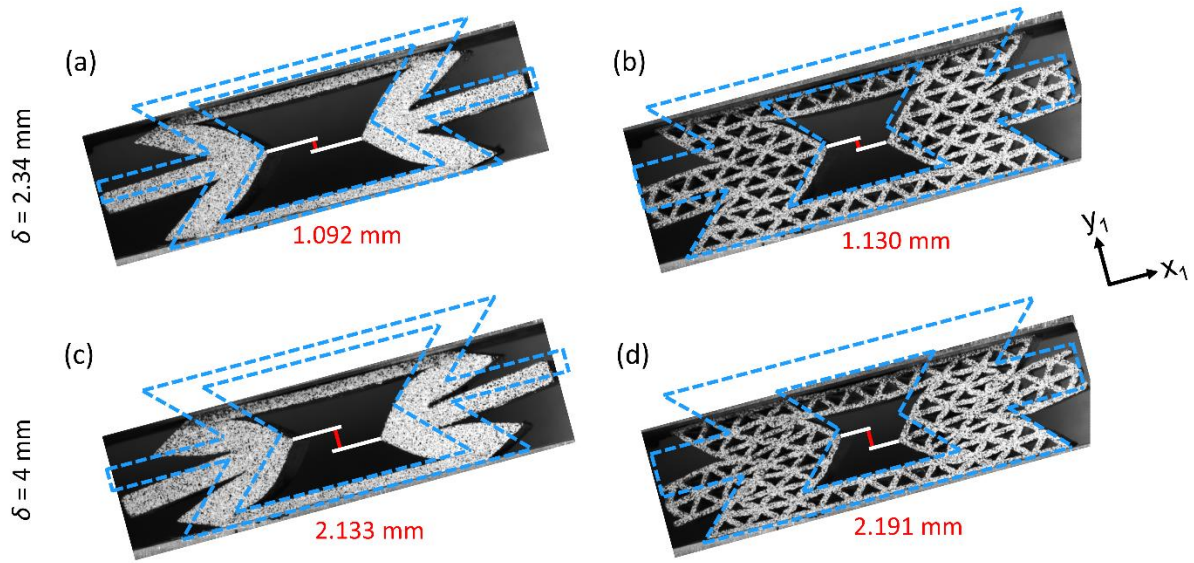


Figure 6.7. Rotation analyses of 45° R-ReH and H-ReH fabricated with soft material. (a) R-ReH and (b) H-ReH at displacement of 2.34 mm. (c) R-ReH and (d) H-ReH at displacement of 4 mm.

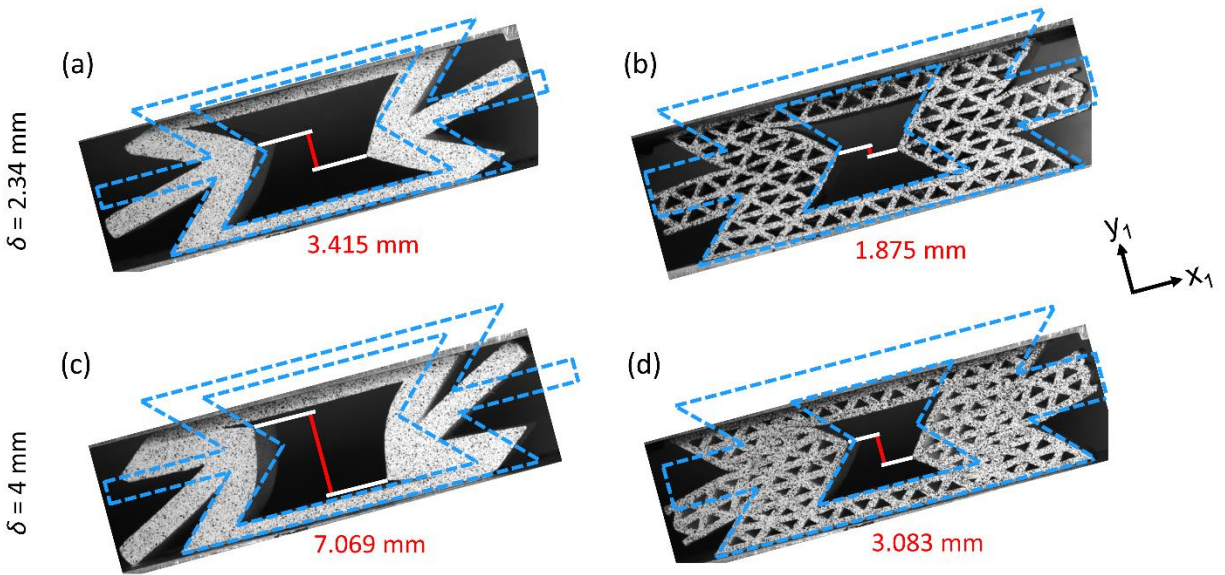


Figure 6.8. Rotation analyses of 45° R-ReH and H-ReH fabricated with rigid material. (a) R-ReH and (b) H-ReH at displacement of 2.34 mm. (c) R-ReH and (d) H-ReH at displacement of 4 mm.

The combined NPR and rotation effects would result in significant difference on the deformation mechanisms of ReHs under the oblique loading. In order to characterize that, the

strain field of H-ReH and R-ReH are characterized by DIC techniques. The strain field of soft ReH are shown in Figure 6.9. For R-ReH, it is clearly shown that the NPR effect leads to severe bending deformation on the inclined member, as one side are heavily stretched while across the neutral axis the other side are heavily compressed, as shown in Figure 6.9 (a). As further compressed, the rotation effect under the oblique loading becomes increasingly notable, which intensify the stretch of the inclined members. In comparison to R-ReH, the soft H-ReH appear to exhibit a different deformation pattern. As shown in Figure 6.9 (b), initially when the compressive displacement is low, the deformation are concentrates and localized on the local joints connecting the 2<sup>nd</sup> order struts in the inclined members. When further compressed, the compression of 2<sup>nd</sup> order struts is exacerbated, and the local struts are severely buckled. In addition, with the increased rotation effect, the 2<sup>nd</sup> order struts located in top-right and bottom-left corner of H-ReH are deformed heavily as well. As the soft material enhance the stretching of the inclined members in R-ReH, while diminished the 2<sup>nd</sup> order struts with an inferior buckling deformation in H-ReH, the R-ReH surprisingly exhibit a higher force response over the soft H-ReH (Figure 6.4 (a)), contradicting with the conventional advantages of the hierarchical structures. These deformation behaviors account for the higher NPR effect and lower rotation effect of R-ReH compared with H-ReH.

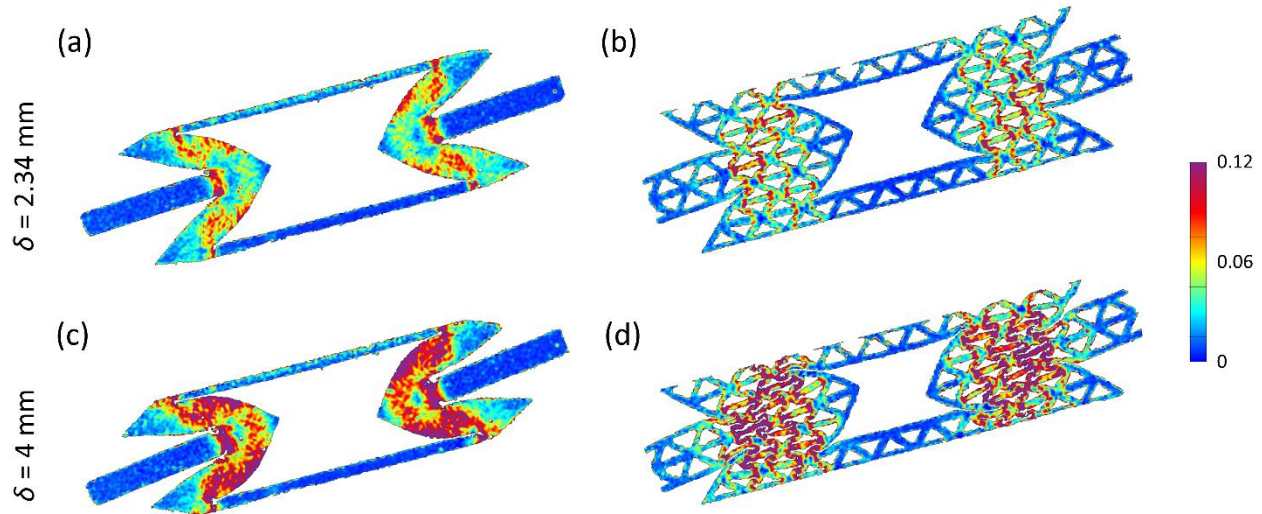


Figure 6.9. DIC strain fields (major strain) of 45° R-ReH and H-ReH fabricated with soft material. (a) R-ReH and (b) H-ReH at displacement of 2.34 mm. (c) R-ReH and (d) H-ReH at displacement of 4 mm.

On the other hand, the ReHs fabricated with rigid materials exhibit completely different deformation patterns under oblique loading. As shown in Figure 6.10 (a), for R-ReH, the deformation are localized in bottom-left and top-right inclined members, forming two plastic hinges rotating in counter-direction, leading to a much larger rotation compared with the soft R-ReH in Figure 6.9 (a). Upon further oblique compression, the plastic hinges deform and rotate more severely, followed by horizontal member fully contacting with the top-left and bottom-right inclined members, respectively. By contrast, the rigid H-ReH exhibit a different deformation pattern with much reduced rotation effect. As shown in Figure 6.10 (b), the 2<sup>nd</sup> order struts avoid the formation of plastic hinges on the inclined members. Instead, the 2<sup>nd</sup> order struts within the top-left and bottom-right members exhibit severe localized stretching deformation. When the oblique compression proceeds further, there are local fracture of 2<sup>nd</sup> order struts, and two shear

bands are formed in top-left and bottom-right part of the inclined member. Such deformation modes not only provide extra support to the H-ReH, but also effectively enhance the rotation resistance of the structure. Therefore, the force response of rigid H-ReH is superior to the rigid R-ReH (Figure 6.4 (b)). In general, the soft material restrains and eliminates the effectiveness of the 2<sup>nd</sup> order hierarchy in 45° H-ReH, leading to a material-dominated behavior of 45° ReHs. To the contrary, the rigid material promotes the effectiveness of the 2<sup>nd</sup> order hierarchy, leading to a structural-dominated behavior of 45° ReHs.

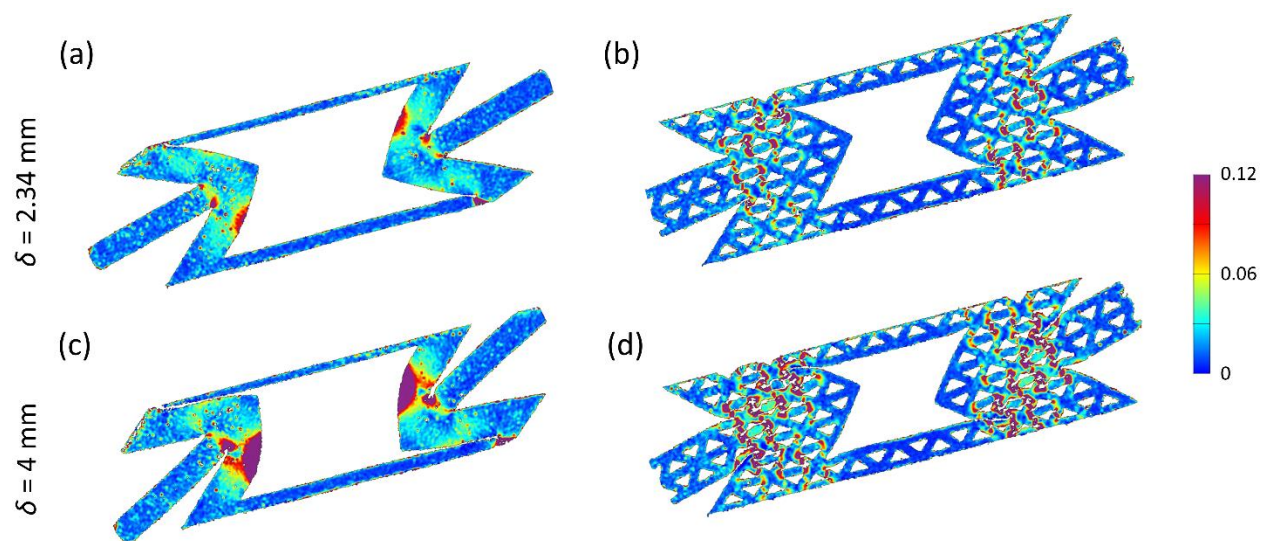


Figure 6.10. DIC strain fields (major strain) of 45° R-ReH and H-ReH fabricated with rigid material. (a) R-ReH and (b) H-ReH at displacement of 2.34 mm. (c) R-ReH and (d) H-ReH at displacement of 4 mm.

It is found that the above soft material-dominated effect is also dependent on the cell-wall angle design of ReHs. In order to characterized it, the ReHs with 60° cell-wall angles are characterized under the oblique loading as well. The rotation analyses of 60° ReHs are shown in

Figure 6.11. Initially at relatively small displacement, R-ReH exhibit a clear inward deformation with inclined members undergo bending deformation due to the NPR effect, as shown in Figure 6.11 (c). In the meantime, the center tip distance is small due to the rotation effect. Once the displacement is increased, inclined members are further bended and rotated, similar to the rotation behavior of soft 45° R-ReH (Figure 6.7 (c)). On the other hand, for 60° H-ReH, the local joints connecting inclined member and horizontal member start to twisted, leading to the connected 2<sup>nd</sup> order struts rotate in a compliant mode. With increased displacement, the local joints severely twisted, and 2<sup>nd</sup> order struts rotate heavily to densified with each other. With the joint twisting and struts rotation deformation mode, H-ReH exhibit slightly higher rotation effect over the R-ReH. However, the soft 60° H-ReH exhibit better force response over the corresponding R-ReH, as shown in Figure 6.5 (a). This means the soft material is not always restrain the effectiveness of 2<sup>nd</sup> order hierarchy, and the hierarchy angle design plays a significant role here.

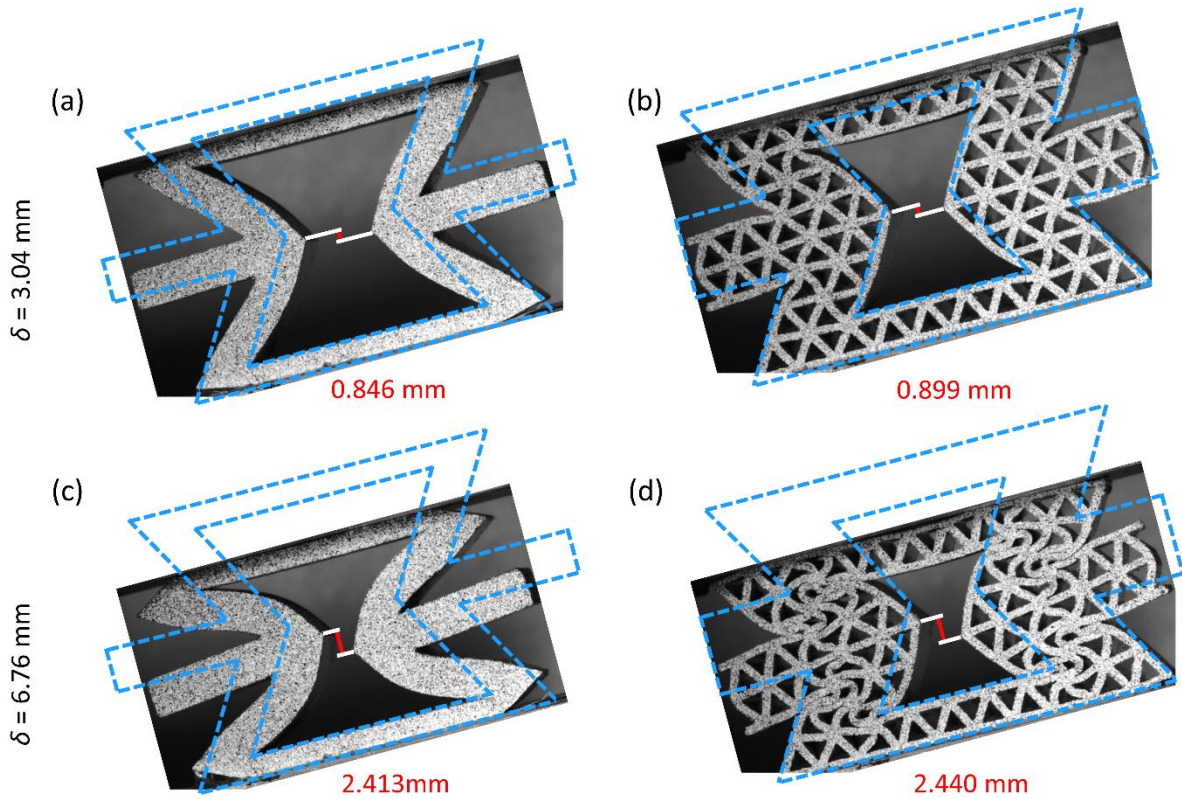


Figure 6.11. Rotation analyses of 60° R-ReH and H-ReH fabricated with soft material. (a) R-ReH and (b) H-ReH at displacement of 3.04 mm. (c) R-ReH and (d) H-ReH at displacement of 6.76 mm.

To further understand that, the strain field of soft 60° ReHs are characterized. As shown in Figure 6.12 (a), initially the inclined members in R-ReH have a bending deformation mode, with small region adjacent to the center tips stretched. As the compression increased, the bending deformation becomes increasingly notable, and much larger region of the inclined member are heavily stretched. This is similar with the 45° R-ReH as previous shown Figure 6.9 (c). As for H-ReH, the local joints connecting inclined member and horizontal member exhibit clear twisting, as shown in Figure 6.12 (b). In addition, deformation localizations are observed at the tips of the connected struts, due to the compliant rotation deformation mode of the struts. Upon further

compression, these struts are extensively rotated and stretched, so that they self-compacted to densified with each other.

It is noted that the localized behavior of 2<sup>nd</sup> order struts in 60° H-ReH is distinctive with the soft 45° H-ReH. As shown in Figure 6.13 (a), in soft 45° H-ReH, under the oblique loading, there is a combination of compression and rotation effect. Due to the softness of the material and smaller angle between inclined and horizontal struts, the 2<sup>nd</sup> order struts are more vulnerable to the compression rather than rotation, thus they are compressed and severely buckled under the oblique loading. Such inferior local deformation mode makes the 2<sup>nd</sup> order hierarchy easily to collapse, thus weaken the overall performance of 45° H-ReH. By contrast, when increases the cell-wall angle to 60°, the 2<sup>nd</sup> order struts exhibit an entirely different deformation mechanism. As shown in Figure 6.13 (b), the joints in inclined members exhibit significant twisting, and the connected 2<sup>nd</sup> order struts rotate in a compliant mode. As the angle between inclined and horizontal struts are higher, the 2<sup>nd</sup> order struts in 60° H-ReH have better resistance to compression but less resistance to the rotation. Therefore, the 2<sup>nd</sup> order struts follow the twisting of the joint and rotate in same direction, distinctive from the compression and buckling behaviors in 45° H-ReH. Considering the force response of both 45° and 60° H-ReHs (Figure 6.4 (a) and Figure 6.5 (a)), it is obvious that the joint twisting and struts compliant rotation mode retains the superiority of the 2<sup>nd</sup> order struts and provides better performance of H-ReH under the oblique loading condition.

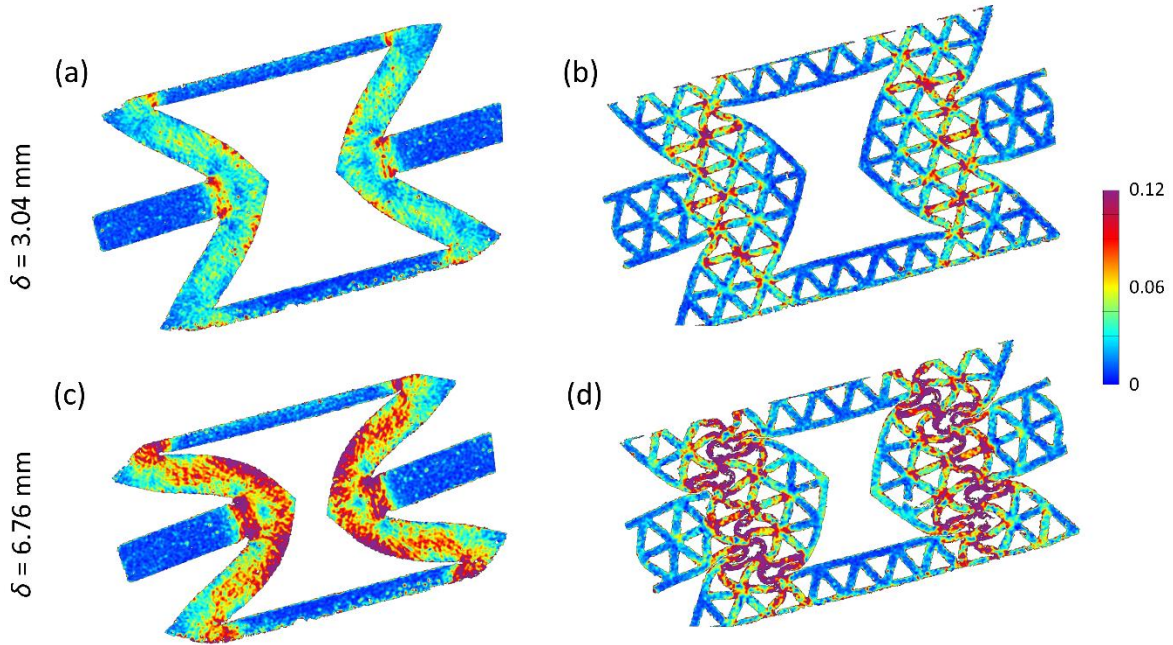


Figure 6.12. DIC strain fields (major strain) of  $60^\circ$  R-ReH and H-ReH fabricated with soft material. (a) R-ReH and (b) H-ReH at displacement of 3.04 mm. (c) R-ReH and (d) H-ReH at displacement of 6.76 mm.

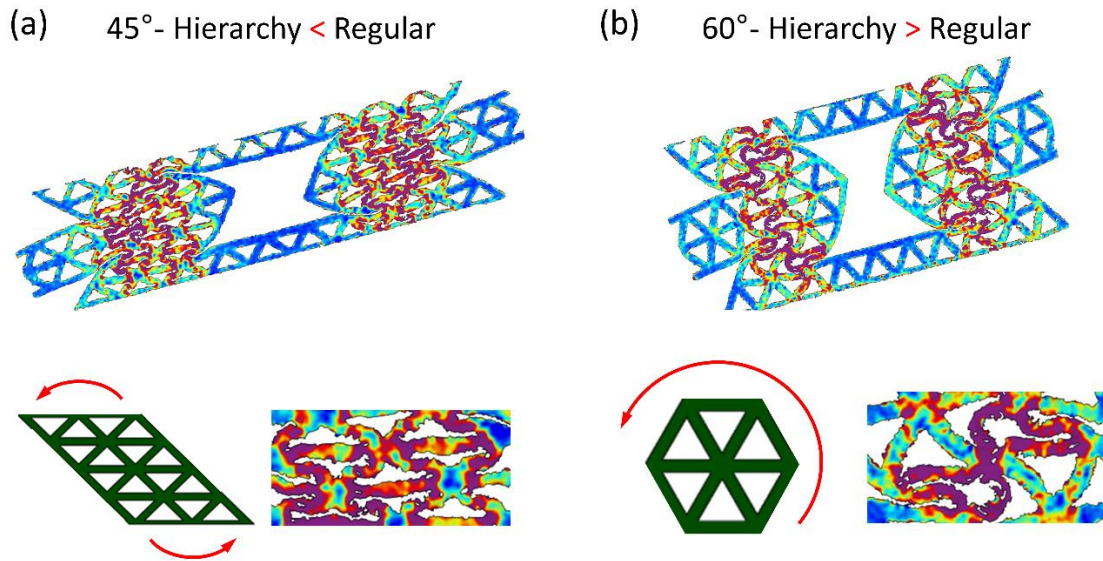


Figure 6.13. Local deformation mechanism of  $2^{\text{nd}}$  order struts under the oblique loading. (a) Soft  $45^\circ$  H-ReH, and (b) soft  $60^\circ$  H-ReH.

### 6.3.3 Energy Absorption of ReHs under Oblique Loading

To evaluate the oblique loading effect on energy absorption capacity of ReHs, the specific energy absorption capacity ( $E_s$ ) is calculated by Eqs (6.1):

$$E_s(\varepsilon) = \frac{\int F d\delta}{m} \quad (6.1)$$

where  $F$  is the crushing force,  $\delta$  is the crushing distance, and  $m$  is the mass of the ReHs. The maximum  $E_s$  values of each ReHs at their densification or failure displacement, i.e.  $E_s^{max}$ , are calculated and plotted in Figure 6.14. It is found that H-ReHs always have higher SEA over R-ReHs, confirming better structural performance of the 2<sup>nd</sup> order triangular hierarchy under the oblique loading condition. Specifically, as shown in Figure 6.14 (a), for soft 45° ReHs, it is observed that H-ReH has increased  $E_s^{max}$  under the oblique loading over the axial one, while R-ReH exhibit a reduced  $E_s^{max}$  under the oblique loading. The superiority of H-ReH under the oblique loading is due to the enhanced structural performance under the combined compressions and rotation effect endowed by the 45° 2<sup>nd</sup> order hierarchy, while R-ReH is vulnerable to the rotation effect thus weakened under the oblique loading due to its bending deformation mode. For rigid 45° ReHs, similar  $E_s^{max}$  enhancement of H-ReH under oblique loading is observed, as shown in Figure 6.14 (b). In addition, the rigid R-ReH shows slightly higher  $E_s^{max}$  values over axial one as well. This is due to the slightly higher fracture displacement of R-ReH under the oblique loading, as additional rotation effect slightly delays the global failure of the R-ReH from the complete fracture of rigid inclined members. When increases the cell-wall angle to 60°, the  $E_s^{max}$  of H-ReH under the oblique loading becomes lower than the axial ones, as shown in Figure 6.14 (c). This is because the additional rotation effect under the oblique loading leads to the

twisting of joints and compliant rotation of the 2<sup>nd</sup> order struts. By contrast, the R-ReH is almost independent with the loading direction. As shown in Figure 6.14 (d), when switches from soft material to rigid materials, similar behavior are observed for H-ReH, while R-ReH exhibits a lower  $E_s^{max}$  under the oblique loading due to the severe rotation effect.

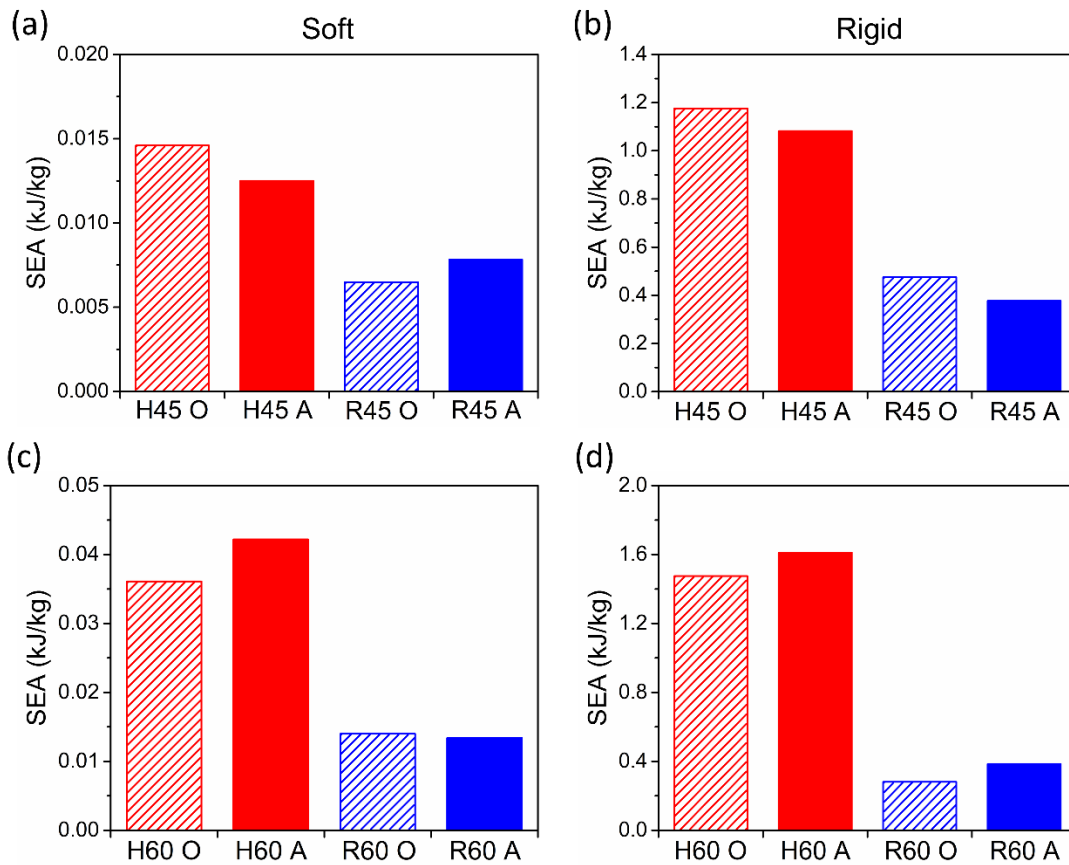


Figure 6.14. Specific energy absorption of H-ReHs and R-ReHs under oblique and axial loading: (a) soft 45° ReHs, (b) rigid 45° ReHs, (c) soft 60° ReHs, and (d) rigid 60° ReHs.

## 6.4 Conclusions

In this study, the oblique and axial crushing behaviors of ReHs are characterized under the

quasi-static compressions. The material effect is investigated by using soft and rigid materials for the ReHs fabrication, respectively, while the structural effect is explored by tuning the cell-wall angles of ReHs as well. The mechanical responses, deformation mechanisms, and energy absorptions of ReHs are investigated. The major findings are summarized as follows:

- (1) Oblique loading has significant effects on the mechanical responses of ReHs. For soft 45° ReHs, the oblique loading condition reduces the force response of R-ReH, but increases the force response of H-ReH. In addition, the constitutive behavior of the fabrication material is found to strongly affect the oblique crushing behaviors of ReHs as well. For soft 45° ReHs, the R-ReH unexpectedly exhibit higher force response over H-ReH under both oblique and axial loading condition. When switch to rigid material, the H-ReHs is reversely superior to the R-ReH. What's more, the cell-wall angle has obvious effect on the oblique crushing behaviors as well. When increases the cell-wall angle to 60°, the soft R-ReH becomes inferior to the H-ReH, on the contrary to the 45° cell-wall angle cases.
- (2) The oblique loading induces both NPR effect and rotation effect on the deformation of ReHs. Through DIC analyses, the oblique loading effect on the deformation mechanisms of ReHs are revealed. For R-ReHs, it is found that bending deformation modes on R-ReHs are material dependent. While soft R-ReH has severe stretching and distributed deformation on the inclined members, rigid R-ReH forms plastic hinges with much localized deformation and larger rotation. In addition, it is found that cell-wall angles have strong effects on the local deformation behavior of H-ReHs. While soft 45° H-ReH has

local struts undergo severe buckling behavior, soft  $60^\circ$  H-ReH has a distinctive joint twisting and compliant struts rotating behavior.

- (3) The specific energy absorption results of ReHs shows that H-ReHs will always have higher SEA over the corresponding R-ReH under the oblique loading. In addition,  $45^\circ$  H-ReHs will have higher SEA under oblique loading compared with axial loading, while for  $60^\circ$  H-ReHs the oblique loading will reduce the SEA. On the other hand, the SEA of R-ReHs under oblique loading is strongly dependent on the cell-wall angle design and the constitutive materials.

Overall, these findings provide new understandings on the oblique crushing behaviors of ReHs, which benefits the design of next generation lightweight robust materials for crashworthiness applications.

## CHAPTER 7. CONCLUSIONS AND FUTURE WORK

### 7.1 Conclusions

The research work presented in this dissertation focuses on the design, additive manufacturing, mechanical properties, and deformation mechanisms of hierarchical re-entrant honeycombs (H-ReHs). The overarching objective of this research is to provide in-depth understanding of the hierarchical structure design and the underlying deformation mechanisms of H-ReHs in various loading conditions, thus establishing the design principles of next-generation lightweight materials and structures with improved and tailorable mechanical properties for various engineering applications. The key scientific conclusions are summarized as follows:

- (1) **Developed a new type of lightweight cellular materials with unprecedented mechanical properties through the combination of structural hierarchy and negative Poisson's ratio effect.** A novel type of hierarchical re-entrant honeycombs (H-ReHs) have been successfully designed through combining the structural hierarchy and auxetic cellular configurations. Such complex geometries across multiple length scales are manufactured through powerful advanced 3D printing technique. We have illustrated, both experimentally and numerically, that the mechanical properties of H-ReHs are significantly enhanced (250% on SEA) in comparison to the R-ReHs, due to the stretching-dominated behavior and uniquely combined local deformation mechanisms. In addition, we have revealed the competition between the 1<sup>st</sup> order and the 2<sup>nd</sup> order hierarchy governed by the aspect ratio of the 2<sup>nd</sup> order triangular hierarchy, which strongly affect the local deformation mode and mechanical performance of H-ReHs. The mechanical properties of H-ReHs are

predictable by the scaling law and much improved at lower density region, which proves the H-ReHs are a type of advanced lightweight structure.

(2) **Demonstrated the effect of cell-wall angle design on the mechanical performance of**

**H-ReHs.** In H-ReHs, the adaptive and reconfigurable 2<sup>nd</sup> order triangular hierarchy governs the mechanical properties of the material. We have validated that the elastic modulus and strength of H-ReHs are strongly dependent on the cell-wall angles, while R-ReHs are inert to that angle change. In addition, the NPR behavior and local deformation mode of H-ReHs can be significantly altered by the cell-wall angle change to achieve targeted performance. In short, we have demonstrated that cell-wall angle is one of the key design parameters to directly tune and control the performance of H-ReHs.

(3) **Revealed the structural effect on the dynamic crushing behavior of H-ReHs.** The

dynamic crushing behavior of H-ReHs is distinct from the quasi-static one, due to the additional structural strain rate effect. We have found the H-ReHs exhibit different strain rate sensitivity in the elastic and plastic regions, owing to the exclusive structural micro-inertia effect and the localized deformation modes in contrast to the R-ReHs. In addition, we have proved the effectiveness of 2<sup>nd</sup> order hierarchy of H-ReHs on the SEA at various strain rates (enhancement of 260% and 480% under quasi-static and dynamic loading conditions, respectively).

(4) **Validated the improved crushing behaviors of H-ReHs under the oblique loading**

**condition.** We have demonstrated the superior mechanical performance of H-ReHs over R-ReHs under the oblique loading (up to 430% SEA enhancement). We have found that

the cell-wall angle significantly affects the oblique loading crushing behavior of H-ReHs. With specific 45° cell-wall angle design, H-ReHs exceptionally exhibit better mechanical performance under oblique condition over the axial loading condition. In addition, it is discovered that the rigidity of constitutive material strongly alters the oblique compressive behavior, due to two distinctive local deformation mechanisms governing the oblique crushing behavior of H-ReHs.

The research outcome of this study eliminates the design constraints of R-ReHs, elaborates the underlying deformation mechanisms governing the unprecedented mechanical performance of the H-ReHs, and provides a new paradigm for the future design of lightweight but robust cellular materials.

## **7.2 Future Work**

### **7.2.1 3D-Printed Hybrid Hierarchical Re-entrant Honeycomb**

Up to recently, the rational design of lightweight hierarchical re-entrant honeycombs (H-ReHs) are mainly focused on devising and optimizing geometric arrangements to achieve unusual mechanical properties. While another route, which is through the rational design of spatially distributing materials with different properties within the H-ReHs, is much less explored [217]. The future goal is to fabricate multi-material H-ReHs with rational assignment of hard and soft materials through advanced 3D printing technique, thus uncover broadened mechanical performance of H-ReHs with tunable properties. The proposed multi-material H-ReHs design is shown in Figure 7.1 (a), with one outer section and one inner section for different material

assignment, respectively. The preliminary results are shown in Figure 7.1 (b). It is found that the multi-material design in H-ReHs can effectively tailor the mechanical performance.

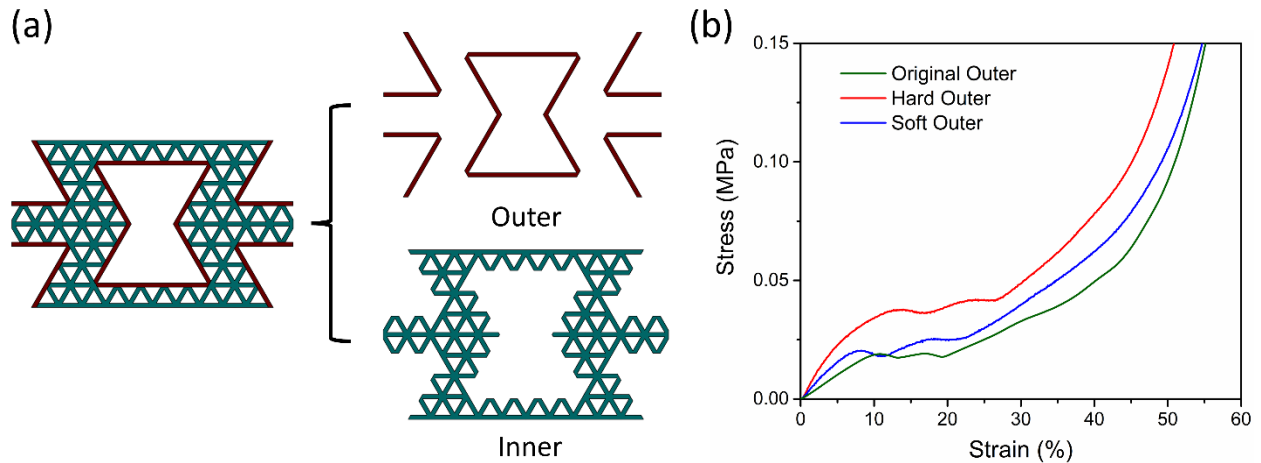


Figure 7.1. (a) Design of multi-material H-ReH divided into outer and inner sections for different material assignment. (b) Stress-strain responses of multi-material H-ReH with hard, original, and soft outer section.

## 7.2.2 Hierarchical Re-entrant Honeycomb Based Advanced Structures

With the current understandings on the design and fundamental deformation mechanisms of H-ReHs in this dissertation, the H-ReHs have great potential as a new core material to be integrated into advanced structures, such as sandwich panels, thin-walled shell structures, and two-phase composite materials, as shown in Figure 7.2. The material selection and geometric design of the H-ReHs will depend on the specific applications. For instance, for sandwich structures, the mechanical compatibility of the face sheets and the H-ReHs core is critical. The research on H-ReH as a new core material could potentially promote the design and performance of current advanced structures.

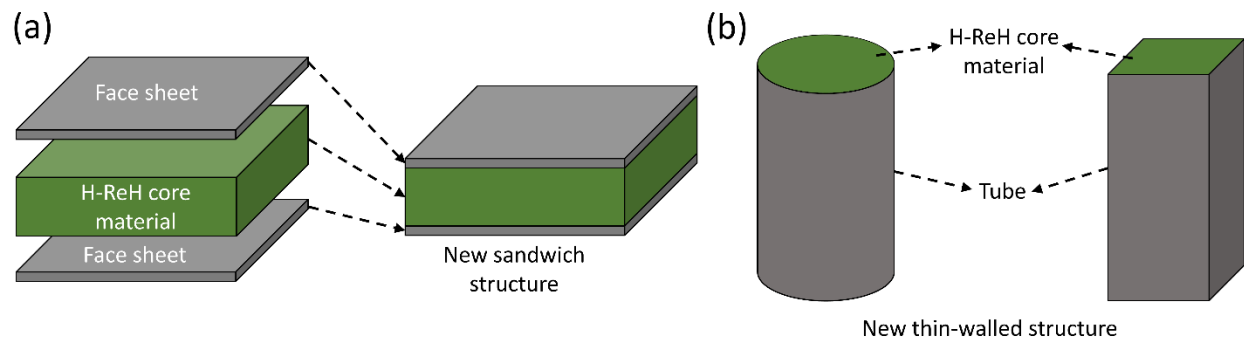


Figure 7.2. (a) Sandwich structure with H-ReH as new core material. (b) H-ReH filled tube as new thin-walled structure.

## BIBLIOGRAPHY

- [1] Taub, A. I., and Luo, A. A., 2015, "Advanced lightweight materials and manufacturing processes for automotive applications," *Mrs Bulletin*, 40(12), pp. 1045-1054.
- [2] Cantor, B., Assender, H., and Grant, P., 2015, *Aerospace materials*, CRC Press.
- [3] Shea, S. B., 2012, "54.5 MPG and Beyond: Materials Lighten the Load for Fuel Economy," U.S. Department of Energy.
- [4] L. Zhu, N. L., and P.R.N. Childs, 2019, "Lightweighting in Aerospace Component and System Design," *Tech Briefs Magazine*.
- [5] Energy Information Administration, 2022, "SHORT-TERM ENERGY OUTLOOK DATA BROWSER," U. S. Energy Information Administration.
- [6] Foreman, D., 2021, "Is The World About To See An Oil Shortage?," *American Petroleum Institute*.
- [7] nTopology, 2022, "Lightweighting Applications through Smart Engineering Design," *nTopology Blog*.
- [8] Droste, D. A., Röttger, J., and Dow, "Crash Performance Increase with Structural BETAFOAM."
- [9] 2013, "FAST (Flight Airworthiness Support Technology)—Special Edition A350XWB," *Airbus Technical Magazine*.
- [10] Fang, H., Bai, S.-L., and Wong, C. P., 2017, "Thermal, mechanical and dielectric properties of flexible BN foam and BN nanosheets reinforced polymer composites for electronic packaging application," *Composites Part A: Applied Science and Manufacturing*, 100, pp. 71-80.
- [11] Zhu, M., Ji, R., Li, Z., Wang, H., Liu, L., and Zhang, Z., 2016, "Preparation of glass ceramic foams for thermal insulation applications from coal fly ash and waste glass," *Construction and Building Materials*, 112, pp. 398-405.
- [12] Cui, L., Kiernan, S., and Gilchrist, M. D., 2009, "Designing the energy absorption capacity of functionally graded foam materials," *Materials Science and Engineering: A*, 507(1-2), pp. 215-225.
- [13] Bunn, P., and Mottram, J., 1993, "Manufacture and compression properties of syntactic

foams," *Composites*, 24(7), pp. 565-571.

[14] Gupta, N., 2007, "A functionally graded syntactic foam material for high energy absorption under compression," *Materials Letters*, 61(4-5), pp. 979-982.

[15] Zhan, C., and Jana, S. C., 2020, "Shrinkage reduced polyimide-graphene oxide composite aerogel for oil absorption," *Microporous and Mesoporous Materials*, 307, p. 110501.

[16] Meng, Y., Young, T. M., Liu, P., Contescu, C. I., Huang, B., and Wang, S., 2015, "Ultralight carbon aerogel from nanocellulose as a highly selective oil absorption material," *Cellulose*, 22(1), pp. 435-447.

[17] Baetens, R., Jelle, B. P., and Gustavsen, A., 2011, "Aerogel insulation for building applications: a state-of-the-art review," *Energy and Buildings*, 43(4), pp. 761-769.

[18] Chandrasekaran, S., Liebig, W. V., Mecklenburg, M., Fiedler, B., Smazna, D., Adelung, R., and Schulte, K., 2016, "Fracture, failure and compression behaviour of a 3D interconnected carbon aerogel (Aerographite) epoxy composite," *Composites science and technology*, 122, pp. 50-58.

[19] Wu, J.-W., Sung, W.-F., and Chu, H.-S., 1999, "Thermal conductivity of polyurethane foams," *International journal of heat and mass transfer*, 42(12), pp. 2211-2217.

[20] Lu, X., Arduini-Schuster, M., Kuhn, J., Nilsson, O., Fricke, J., and Pekala, R., 1992, "Thermal conductivity of monolithic organic aerogels," *Science*, 255(5047), pp. 971-972.

[21] Deshpande, V., Ashby, M., and Fleck, N., 2001, "Foam topology: bending versus stretching dominated architectures," *Acta materialia*, 49(6), pp. 1035-1040.

[22] Isopa, 2015, "The Benefits and history of polyurethane flexible foam," *European Diisocyanate and Polyol Producers Association*.

[23] Growth, N., 2011, "Futuristic Cellular Structure Architecture," *Natural Growth*.

[24] Brinker, C. J., "What is Aerogel?," [AEROGEL.ORG](http://AEROGEL.ORG).

[25] Zhan, C., 2018, "Towards Development of Porous Polymeric Materials for Oil Absorption and Energy Storage Devices," *University of Akron*.

[26] Yeo, S. J., Oh, M. J., and Yoo, P. J., 2019, "Structurally controlled cellular architectures for high - performance ultra - lightweight materials," *Advanced Materials*, 31(34), p. 1803670.

- [27] Schaedler, T. A., and Carter, W. B., 2016, "Architected cellular materials," *Annual Review of Materials Research*, 46, pp. 187-210.
- [28] Bassett, J. D., Williams, A. J., Murphy, E., Boyde, A., Howell, P. G., Swinhoe, R., Archanco, M., Flamant, F., Samarut, J., and Costagliola, S., 2008, "A lack of thyroid hormones rather than excess thyrotropin causes abnormal skeletal development in hypothyroidism," *Molecular endocrinology*, 22(2), pp. 501-512.
- [29] Vukusic, P., and Sambles, J. R., 2003, "Photonic structures in biology," *Nature*, 424(6950), pp. 852-855.
- [30] marigranula, "First stone wheel," 123RF LLC.
- [31] Complete Custom Wheel, 2022, "CCW CORSAIR C10 MONOBLOCK FORGED RACING WHEELS," MW Company LLC.
- [32] Gallery, S., 2020, "Rediscovering ancient Egypt: What's inside the Great Pyramid?," Sadigh Gallery.
- [33] Omondi, S., 2017, "How Tall Is The Eiffel Tower?," WorldAtlas.
- [34] Wadley, H. N., 2006, "Multifunctional periodic cellular metals," *Philosophical Transactions of the Royal Society A: Mathematical, Physical and Engineering Sciences*, 364(1838), pp. 31-68.
- [35] Foo, C. C., Chai, G. B., and Seah, L. K., 2007, "Mechanical properties of Nomex material and Nomex honeycomb structure," *Composite structures*, 80(4), pp. 588-594.
- [36] Zhang, Q., Yang, X., Li, P., Huang, G., Feng, S., Shen, C., Han, B., Zhang, X., Jin, F., and Xu, F., 2015, "Bioinspired engineering of honeycomb structure—Using nature to inspire human innovation," *Progress in Materials Science*, 74, pp. 332-400.
- [37] Bitzer, T., 1997, *Honeycomb technology: materials, design, manufacturing, applications and testing*, Springer Science & Business Media.
- [38] Gu, S., Lu, T., and Evans, A., 2001, "On the design of two-dimensional cellular metals for combined heat dissipation and structural load capacity," *International Journal of Heat and Mass Transfer*, 44(11), pp. 2163-2175.
- [39] Wang, Z., Liu, J., and Hui, D., 2017, "Mechanical behaviors of inclined cell honeycomb structure subjected to compression," *Composites Part B: Engineering*, 110, pp. 307-314.

- [40] Yap, Y., and Yeong, W., 2015, "Shape recovery effect of 3D printed polymeric honeycomb: This paper studies the elastic behaviour of different honeycomb structures produced by PolyJet technology," *Virtual and Physical Prototyping*, 10(2), pp. 91-99.
- [41] Nazir, A., Abate, K. M., Kumar, A., and Jeng, J.-Y., 2019, "A state-of-the-art review on types, design, optimization, and additive manufacturing of cellular structures," *The International Journal of Advanced Manufacturing Technology*, 104(9), pp. 3489-3510.
- [42] Gibson, L. J., 2003, "Cellular solids," *Mrs Bulletin*, 28(4), pp. 270-274.
- [43] Gibson, I., and Ashby, M. F., 1982, "The mechanics of three-dimensional cellular materials," *Proceedings of the royal society of London. A. Mathematical and physical sciences*, 382(1782), pp. 43-59.
- [44] Ashby, M. F., and Medalist, R. M., 1983, "The mechanical properties of cellular solids," *Metallurgical Transactions A*, 14(9), pp. 1755-1769.
- [45] Rho, J.-Y., Kuhn-Spearing, L., and Zioupos, P., 1998, "Mechanical properties and the hierarchical structure of bone," *Medical engineering & physics*, 20(2), pp. 92-102.
- [46] Meyers, M. A., McKittrick, J., and Chen, P.-Y., 2013, "Structural biological materials: critical mechanics-materials connections," *science*, 339(6121), pp. 773-779.
- [47] Lakes, R., 1993, "Materials with structural hierarchy," *Nature*, 361(6412), pp. 511-515.
- [48] Zheng, X., Smith, W., Jackson, J., Moran, B., Cui, H., Chen, D., Ye, J., Fang, N., Rodriguez, N., and Weisgraber, T., 2016, "Multiscale metallic metamaterials," *Nature materials*, 15(10), pp. 1100-1106.
- [49] Müller, R., 2009, "Hierarchical microimaging of bone structure and function," *Nature Reviews Rheumatology*, 5(7), pp. 373-381.
- [50] Tampieri, A., Sprio, S., Ruffini, A., Celotti, G., Lesci, I. G., and Roveri, N., 2009, "From wood to bone: multi-step process to convert wood hierarchical structures into biomimetic hydroxyapatite scaffolds for bone tissue engineering," *Journal of Materials Chemistry*, 19(28), pp. 4973-4980.
- [51] Koch, K., and Barthlott, W., 2009, "Superhydrophobic and superhydrophilic plant surfaces: an inspiration for biomimetic materials," *Philosophical Transactions of the Royal Society A: Mathematical, Physical and Engineering Sciences*, 367(1893), pp. 1487-1509.
- [52] Libonati, F., and Buehler, M. J., 2017, "Advanced structural materials by bioinspiration,"

Advanced Engineering Materials, 19(5), p. 1600787.

[53] Fratzl, P., and Weinkamer, R., 2007, "Nature's hierarchical materials," *Progress in materials Science*, 52(8), pp. 1263-1334.

[54] Jia, Z., Yu, Y., Hou, S., and Wang, L., 2019, "Biomimetic architected materials with improved dynamic performance," *Journal of the Mechanics and Physics of Solids*, 125, pp. 178-197.

[55] Shi, S., Li, Y., Ngo-Dinh, B.-N., Markmann, J., and Weissmüller, J., 2021, "Scaling behavior of stiffness and strength of hierarchical network nanomaterials," *Science*, 371(6533), pp. 1026-1033.

[56] Sha, Y., Jiani, L., Haoyu, C., Ritchie, R. O., and Jun, X., 2018, "Design and strengthening mechanisms in hierarchical architected materials processed using additive manufacturing," *International Journal of Mechanical Sciences*, 149, pp. 150-163.

[57] Moestopo, W. P., Mateos, A. J., Fuller, R. M., Greer, J. R., and Portela, C. M., 2020, "Pushing and pulling on ropes: hierarchical woven materials," *Advanced Science*, 7(20), p. 2001271.

[58] Dong, L., 2019, "Mechanical response of Ti-6Al-4V hierarchical architected metamaterials," *Acta Materialia*, 175, pp. 90-106.

[59] Meza, L. R., Zelhofer, A. J., Clarke, N., Mateos, A. J., Kochmann, D. M., and Greer, J. R., 2015, "Resilient 3D hierarchical architected metamaterials," *Proceedings of the National Academy of Sciences*, 112(37), pp. 11502-11507.

[60] Meza, L. R., Das, S., and Greer, J. R., 2014, "Strong, lightweight, and recoverable three-dimensional ceramic nanolattices," *Science*, 345(6202), pp. 1322-1326.

[61] Schaedler, T. A., Jacobsen, A. J., Torrents, A., Sorensen, A. E., Lian, J., Greer, J. R., Valdevit, L., and Carter, W. B., 2011, "Ultralight metallic microlattices," *Science*, 334(6058), pp. 962-965.

[62] Baughman, R. H., Shacklette, J. M., Zakhidov, A. A., and Stafström, S., 1998, "Negative Poisson's ratios as a common feature of cubic metals," *Nature*, 392(6674), pp. 362-365.

[63] Grima, J. N., Jackson, R., Alderson, A., and Evans, K. E., 2000, "Do zeolites have negative Poisson's ratios?," *Advanced Materials*, 12(24), pp. 1912-1918.

[64] Lakes, R., 1987, "Foam structures with a negative Poisson's ratio," *Science*, 235, pp. 1038-1041.

- [65] Song, F., Zhou, J., Xu, X., Xu, Y., and Bai, Y., 2008, "Effect of a negative Poisson ratio in the tension of ceramics," *Physical review letters*, 100(24), p. 245502.
- [66] Grima, J. N., Winczewski, S., Mizzi, L., Grech, M. C., Cauchi, R., Gatt, R., Attard, D., Wojciechowski, K. W., and Rybicki, J., 2015, "Tailoring graphene to achieve negative Poisson's ratio properties," *Advanced materials*, 27(8), pp. 1455-1459.
- [67] Alderson, A., and Alderson, K., 2007, "Auxetic materials," *Proceedings of the Institution of Mechanical Engineers, Part G: Journal of Aerospace Engineering*, 221(4), pp. 565-575.
- [68] Mohsenizadeh, S., Alipour, R., Rad, M. S., Nejad, A. F., and Ahmad, Z., 2015, "Crashworthiness assessment of auxetic foam-filled tube under quasi-static axial loading," *Materials & Design*, 88, pp. 258-268.
- [69] Lakes, R., and Elms, K., 1993, "Indentability of conventional and negative Poisson's ratio foams," *Journal of Composite Materials*, 27(12), pp. 1193-1202.
- [70] Choi, J., and Lakes, R., 1996, "Fracture toughness of re-entrant foam materials with a negative Poisson's ratio: experiment and analysis," *International Journal of fracture*, 80(1), pp. 73-83.
- [71] Wang, Z., and Hu, H., 2014, "Auxetic materials and their potential applications in textiles," *Textile Research Journal*, 84(15), pp. 1600-1611.
- [72] Liu, Y., Hu, H., Lam, J. K., and Liu, S., 2010, "Negative Poisson's ratio weft-knitted fabrics," *Textile Research Journal*, 80(9), pp. 856-863.
- [73] Hu, H., Wang, Z., and Liu, S., 2011, "Development of auxetic fabrics using flat knitting technology," *Textile research journal*, 81(14), pp. 1493-1502.
- [74] Wang, Y., Wang, L., Ma, Z.-d., and Wang, T., 2016, "A negative Poisson's ratio suspension jounce bumper," *Materials & Design*, 103, pp. 90-99.
- [75] Liu, Q., 2006, "Literature review: materials with negative Poisson's ratios and potential applications to aerospace and defence."
- [76] Scarpa, F., 2008, "Auxetic materials for bioprotheses [In the Spotlight]," *IEEE Signal Processing Magazine*, 25(5), pp. 128-126.
- [77] Mardling, P., Alderson, A., Jordan-Mahy, N., and Le Maitre, C. L., 2020, "The use of auxetic materials in tissue engineering," *Biomaterials science*, 8(8), pp. 2074-2083.

- [78] Wang, H., Lu, Z., Yang, Z., and Li, X., 2019, "A novel re-entrant auxetic honeycomb with enhanced in-plane impact resistance," *Composite Structures*, 208, pp. 758-770.
- [79] Qiao, J., and Chen, C., 2015, "Impact resistance of uniform and functionally graded auxetic double arrowhead honeycombs," *International Journal of Impact Engineering*, 83, pp. 47-58.
- [80] Alderson, A., Alderson, K. L., Attard, D., Evans, K. E., Gatt, R., Grima, J. N., Miller, W., Ravirala, N., Smith, C., and Zied, K., 2010, "Elastic constants of 3-, 4- and 6-connected chiral and anti-chiral honeycombs subject to uniaxial in-plane loading," *Composites Science and Technology*, 70(7), pp. 1042-1048.
- [81] Prall, D., and Lakes, R., 1997, "Properties of a chiral honeycomb with a Poisson's ratio of—1," *International Journal of Mechanical Sciences*, 39(3), pp. 305-314.
- [82] Jiang, Y., and Li, Y., 2017, "3D printed chiral cellular solids with amplified auxetic effects due to elevated internal rotation," *Advanced Engineering Materials*, 19(2), p. 1600609.
- [83] Spadoni, A., and Ruzzene, M., 2012, "Elasto-static micropolar behavior of a chiral auxetic lattice," *Journal of the Mechanics and Physics of Solids*, 60(1), pp. 156-171.
- [84] Yasuda, H., and Yang, J., 2015, "Reentrant origami-based metamaterials with negative Poisson's ratio and bistability," *Physical review letters*, 114(18), p. 185502.
- [85] Lv, C., Krishnaraju, D., Konjevod, G., Yu, H., and Jiang, H., 2014, "Origami based mechanical metamaterials," *Scientific reports*, 4(1), pp. 1-6.
- [86] He, Y., Zhang, P., You, Z., Li, Z., Wang, Z., and Shu, X., 2020, "Programming mechanical metamaterials using origami tessellations," *Composites Science and Technology*, 189, p. 108015.
- [87] Hou, Y., Neville, R., Scarpa, F., Remillat, C., Gu, B., and Ruzzene, M., 2014, "Graded conventional-auxetic Kirigami sandwich structures: Flatwise compression and edgewise loading," *Composites Part B: Engineering*, 59, pp. 33-42.
- [88] Tang, Y., and Yin, J., 2017, "Design of cut unit geometry in hierarchical kirigami-based auxetic metamaterials for high stretchability and compressibility," *Extreme Mechanics Letters*, 12, pp. 77-85.
- [89] Tang, Y., Lin, G., Han, L., Qiu, S., Yang, S., and Yin, J., 2015, "Design of hierarchically cut hinges for highly stretchable and reconfigurable metamaterials with enhanced strength," *Advanced materials*, 27(44), pp. 7181-7190.

- [90] Cho, Y., Shin, J.-H., Costa, A., Kim, T. A., Kunin, V., Li, J., Lee, S. Y., Yang, S., Han, H. N., and Choi, I.-S., 2014, "Engineering the shape and structure of materials by fractal cut," *Proceedings of the National Academy of Sciences*, 111(49), pp. 17390-17395.
- [91] Milton, G. W., 2013, "Complete characterization of the macroscopic deformations of periodic unimode metamaterials of rigid bars and pivots," *Journal of the Mechanics and Physics of Solids*, 61(7), pp. 1543-1560.
- [92] Grima, J. N., Alderson, A., and Evans, K., 2005, "Auxetic behaviour from rotating rigid units," *Physica status solidi (b)*, 242(3), pp. 561-575.
- [93] Grima, J. N., and Evans, K. E., 2006, "Auxetic behavior from rotating triangles," *Journal of materials science*, 41(10), pp. 3193-3196.
- [94] Pozniak, A., and Wojciechowski, K., 2014, "Poisson's ratio of rectangular anti - chiral structures with size dispersion of circular nodes," *physica status solidi (b)*, 251(2), pp. 367-374.
- [95] Liu, W., Wang, N., Luo, T., and Lin, Z., 2016, "In-plane dynamic crushing of re-entrant auxetic cellular structure," *Materials & Design*, 100, pp. 84-91.
- [96] Yang, L., Harrysson, O., West, H., and Cormier, D., 2015, "Mechanical properties of 3D re-entrant honeycomb auxetic structures realized via additive manufacturing," *International Journal of Solids and Structures*, 69, pp. 475-490.
- [97] Scarpa, F., and Tomlin, P., 2000, "On the transverse shear modulus of negative Poisson's ratio honeycomb structures," *Fatigue & Fracture of Engineering Materials & Structures*, 23(8), pp. 717-720.
- [98] Scarpa, F., and Tomlinson, G., 2000, "Theoretical characteristics of the vibration of sandwich plates with in-plane negative Poisson's ratio values," *Journal of Sound and Vibration*, 230(1), pp. 45-67.
- [99] Hu, L., Zhou, M. Z., and Deng, H., 2019, "Dynamic indentation of auxetic and non-auxetic honeycombs under large deformation," *Compos. Struct.*, 207, pp. 323-330.
- [100] Qi, C., Remennikov, A., Pei, L.-Z., Yang, S., Yu, Z.-H., and Ngo, T. D., 2017, "Impact and close-in blast response of auxetic honeycomb-cored sandwich panels: experimental tests and numerical simulations," *Compos. Struct.*, 180, pp. 161-178.
- [101] Smith, F., Scarpa, F., and Chambers, B., 2000, "The electromagnetic properties of re-entrant dielectric honeycombs," *IEEE Microwave and Guided Wave Letters*, 10(11), pp. 451-453.

- [102] Shen, L., Wang, Z., Wang, X., and Wei, K., 2021, "Negative Poisson's ratio and effective Young's modulus of a vertex-based hierarchical re-entrant honeycomb structure," *International Journal of Mechanical Sciences*, 206, p. 106611.
- [103] Li, D., Yin, J., Dong, L., and Lakes, R. S., 2016, "Numerical analysis on mechanical behaviors of hierarchical cellular structures with negative Poisson's ratio," *Smart Materials and Structures*, 26(2), p. 025014.
- [104] Zhang, W., Zhao, S., Sun, R., Scarpa, F., and Wang, J., 2019, "In-plane mechanical behavior of a new star-re-entrant hierarchical metamaterial," *Polymers*, 11(7), p. 1132.
- [105] An, M.-R., Wang, L., Liu, H.-T., and Ren, F.-G., 2022, "In-plane crushing response of a novel bidirectional re-entrant honeycomb with two plateau stress regions," *Thin-Walled Structures*, 170, p. 108530.
- [106] Tan, H., He, Z., Li, K., Li, E., Cheng, A., and Xu, B., 2019, "In-plane crashworthiness of re-entrant hierarchical honeycombs with negative Poisson's ratio," *Composite Structures*, 229, p. 111415.
- [107] Zhan, C., Li, M., McCoy, R., Zhao, L., and Lu, W., 2022, "3D printed hierarchical re-entrant honeycombs: Enhanced mechanical properties and the underlying deformation mechanisms," *Composite Structures*, 290, p. 115550.
- [108] Tan, H., He, Z., Li, E., Tan, X., Cheng, A., and Li, Q., 2020, "Energy absorption characteristics of three-layered sandwich panels with graded re-entrant hierarchical honeycomb cores," *Aerospace Science and Technology*, 106, p. 106073.
- [109] Ngo, T. D., Kashani, A., Imbalzano, G., Nguyen, K. T., and Hui, D., 2018, "Additive manufacturing (3D printing): A review of materials, methods, applications and challenges," *Composites Part B: Engineering*, 143, pp. 172-196.
- [110] Rayna, T., and Striukova, L., 2016, "From rapid prototyping to home fabrication: How 3D printing is changing business model innovation," *Technological Forecasting and Social Change*, 102, pp. 214-224.
- [111] Chua, C. K., and Leong, K. F., 2014, *3D Printing and additive manufacturing: Principles and applications (with companion media pack)-of rapid prototyping*, World Scientific Publishing Company.
- [112] Tay, Y. W. D., Panda, B., Paul, S. C., Noor Mohamed, N. A., Tan, M. J., and Leong, K. F.,

2017, "3D printing trends in building and construction industry: a review," *Virtual and Physical Prototyping*, 12(3), pp. 261-276.

[113] Yu, C., Schimelman, J., Wang, P., Miller, K. L., Ma, X., You, S., Guan, J., Sun, B., Zhu, W., and Chen, S., 2020, "Photopolymerizable biomaterials and light-based 3D printing strategies for biomedical applications," *Chemical reviews*, 120(19), pp. 10695-10743.

[114] Li, J., Wu, C., Chu, P. K., and Gelinsky, M., 2020, "3D printing of hydrogels: Rational design strategies and emerging biomedical applications," *Materials Science and Engineering: R: Reports*, 140, p. 100543.

[115] Shahrudin, N., Lee, T. C., and Ramlan, R., 2019, "An overview on 3D printing technology: Technological, materials, and applications," *Procedia Manufacturing*, 35, pp. 1286-1296.

[116] Chen, Y., Li, T., Jia, Z., Scarpa, F., Yao, C.-W., and Wang, L., 2018, "3D printed hierarchical honeycombs with shape integrity under large compressive deformations," *Materials & Design*, 137, pp. 226-234.

[117] Peng, M., Wen, Z., Xie, L., Cheng, J., Jia, Z., Shi, D., Zeng, H., Zhao, B., Liang, Z., and Li, T., 2019, "3D printing of ultralight biomimetic hierarchical graphene materials with exceptional stiffness and resilience," *Advanced Materials*, 31(35), p. 1902930.

[118] Wang, X., Jiang, M., Zhou, Z., Gou, J., and Hui, D., 2017, "3D printing of polymer matrix composites: A review and prospective," *Composites Part B: Engineering*, 110, pp. 442-458.

[119] Singh, S., Ramakrishna, S., and Berto, F., 2020, "3D Printing of polymer composites: A short review," *Material Design & Processing Communications*, 2(2), p. e97.

[120] Parandoush, P., and Lin, D., 2017, "A review on additive manufacturing of polymer-fiber composites," *Composite Structures*, 182, pp. 36-53.

[121] Ibrahim, D., Broilo, T. L., Heitz, C., de Oliveira, M. G., de Oliveira, H. W., Nobre, S. M. W., dos Santos Filho, J. H. G., and Silva, D. N., 2009, "Dimensional error of selective laser sintering, three-dimensional printing and PolyJet™ models in the reproduction of mandibular anatomy," *Journal of Cranio-Maxillofacial Surgery*, 37(3), pp. 167-173.

[122] Khoo, Z. X., Teoh, J. E. M., Liu, Y., Chua, C. K., Yang, S., An, J., Leong, K. F., and Yeong, W. Y., 2015, "3D printing of smart materials: A review on recent progresses in 4D printing," *Virtual and Physical Prototyping*, 10(3), pp. 103-122.

[123] Lee, J., Kim, H.-C., Choi, J.-W., and Lee, I. H., 2017, "A review on 3D printed smart devices

for 4D printing," *International Journal of Precision Engineering and Manufacturing-Green Technology*, 4(3), pp. 373-383.

[124] Konta, A. A., García-Piña, M., and Serrano, D. R., 2017, "Personalised 3D printed medicines: which techniques and polymers are more successful?," *Bioengineering*, 4(4), p. 79.

[125] Xometry Europe, 2021, "Polyjet 3D Printing: Technology Overview," Xometry Europe GmbH.

[126] Zhan, C., Li, M., McCoy, R., Zhao, L., and Lu, W., "3D-Printed Hierarchical Re-Entrant Honeycomb With Improved Structural Stability Under Quasi-Static Compressive Loading," *Proc. ASME International Mechanical Engineering Congress and Exposition, American Society of Mechanical Engineers*, p. V003T003A053.

[127] Pan, B., Qian, K., Xie, H., and Asundi, A., 2009, "Two-dimensional digital image correlation for in-plane displacement and strain measurement: a review," *Measurement science and technology*, 20(6), p. 062001.

[128] McCormick, N., and Lord, J., 2010, "Digital image correlation," *Materials today*, 13(12), pp. 52-54.

[129] Pan, B., 2011, "Recent progress in digital image correlation," *Experimental mechanics*, 51(7), pp. 1223-1235.

[130] Kalubadanage, D., Remennikov, A., Ngo, T., and Qi, C., 2021, "Close-in blast resistance of large-scale auxetic re-entrant honeycomb sandwich panels," *Journal of Sandwich Structures & Materials*, 23(8), pp. 4016-4053.

[131] Betts, D., Sadeghian, P., and Fam, A., 2021, "Experiments and nonlinear analysis of the impact behaviour of sandwich panels constructed with flax fibre-reinforced polymer faces and foam cores," *Journal of Sandwich Structures & Materials*, 23(7), pp. 3139-3163.

[132] Simpson, J., and Kazancı, Z., 2020, "Crushing investigation of crash boxes filled with honeycomb and re-entrant (auxetic) lattices," *Thin-Walled Struct*, 150, p. 106676.

[133] Wang, T., Li, Z., Wang, L., and Hulbert, G. M., 2020, "Crashworthiness analysis and collaborative optimization design for a novel crash-box with re-entrant auxetic core," *Struct Multidiscipl Optim*, 62(4), pp. 2167-2179.

[134] Li, T., Chen, Y., Hu, X., Li, Y., and Wang, L., 2018, "Exploiting negative Poisson's ratio to design 3D-printed composites with enhanced mechanical properties," *Mater Des*, 142, pp. 247-

258.

[135] López - Valdeolivas, M., Liu, D., Broer, D. J., and Sánchez - Somolinos, C., 2018, "4D printed actuators with soft - robotic functions," *Macromol Rapid Commun*, 39(5), p. 1700710.

[136] Kang, S., Hong, S. Y., Kim, N., Oh, J., Park, M., Chung, K. Y., Lee, S.-S., Lee, J., and Son, J. G., 2020, "Stretchable lithium-ion battery based on re-entrant micro-honeycomb electrodes and cross-linked gel electrolyte," *ACS nano*, 14(3), pp. 3660-3668.

[137] Neville, R. M., Chen, J., Guo, X., Zhang, F., Wang, W., Dobah, Y., Scarpa, F., Leng, J., and Peng, H.-X., 2017, "A Kirigami shape memory polymer honeycomb concept for deployment," *Smart Mater Struct*, 26(5), p. 05LT03.

[138] Mizzi, L., Attard, D., Casha, A., Grima, J. N., and Gatt, R., 2014, "On the suitability of hexagonal honeycombs as stent geometries," *Phys. Status Solidi B*, 251(2), pp. 328-337.

[139] Alam, F., Shukla, V. R., Varadarajan, K., and Kumar, S., 2020, "Microarchitected 3D printed polylactic acid (PLA) nanocomposite scaffolds for biomedical applications," *J Mech Behav Biomed Mater*, 103, p. 103576.

[140] Ouisse, M., Collet, M., and Scarpa, F., 2016, "A piezo-shunted kirigami auxetic lattice for adaptive elastic wave filtering," *Smart Mater Struct*, 25(11), p. 115016.

[141] Li, P., Zhang, X., Zhang, Z., and Wen, Q., 2021, "Application of Re-Entrant Honeycomb Auxetic Structure in Force Measurements," *IEEE Sens J*, 21(21), pp. 24202-24208.

[142] Larsen, U. D., Signund, O., and Bouwsta, S., 1997, "Design and fabrication of compliant micromechanisms and structures with negative Poisson's ratio," *J Microelectromech Syst*, 6(2), pp. 99-106.

[143] Levy, O., Krylov, S., and Goldfarb, I., 2006, "Design considerations for negative Poisson ratio structures under large deflection for MEMS applications," *Smart Mater Struct*, 15(5), p. 1459.

[144] Cole, G., and Sherman, A., 1995, "Light weight materials for automotive applications," *Materials characterization*, 35(1), pp. 3-9.

[145] Immarigeon, J., Holt, R., Koul, A., Zhao, L., Wallace, W., and Beddoes, J., 1995, "Lightweight materials for aircraft applications," *Materials characterization*, 35(1), pp. 41-67.

[146] Lu, G., and Yu, T., 2003, *Energy absorption of structures and materials*, Elsevier.

- [147] Sun, M.-H., Huang, S.-Z., Chen, L.-H., Li, Y., Yang, X.-Y., Yuan, Z.-Y., and Su, B.-L., 2016, "Applications of hierarchically structured porous materials from energy storage and conversion, catalysis, photocatalysis, adsorption, separation, and sensing to biomedicine," *Chem Soc Rev*, 45(12), pp. 3479-3563.
- [148] Li, Y., Fu, Z. Y., and Su, B. L., 2012, "Hierarchically structured porous materials for energy conversion and storage," *Adv Funct Mater*, 22(22), pp. 4634-4667.
- [149] Wadley, H. N., Fleck, N. A., and Evans, A. G., 2003, "Fabrication and structural performance of periodic cellular metal sandwich structures," *Compos Sci Technol*, 63(16), pp. 2331-2343.
- [150] Zheng, L., Wu, D., Zhou, A., Pan, B., Wang, Y., and Wang, J., 2014, "Experimental and numerical study on heat transfer characteristics of metallic honeycomb core structure in transient thermal shock environments," *Int J Thermophys*, 35(8), pp. 1557-1576.
- [151] Zhang, X.-C., An, L.-Q., Ding, H.-M., Zhu, X.-Y., and El-Rich, M., 2015, "The influence of cell micro-structure on the in-plane dynamic crushing of honeycombs with negative Poisson's ratio," *J. Sandw. Struct. Mater.*, 17(1), pp. 26-55.
- [152] Mukhopadhyay, T., and Adhikari, S., 2016, "Effective in-plane elastic properties of auxetic honeycombs with spatial irregularity," *Mech Mater*, 95, pp. 204-222.
- [153] Dong, Z., Li, Y., Zhao, T., Wu, W., Xiao, D., and Liang, J., 2019, "Experimental and numerical studies on the compressive mechanical properties of the metallic auxetic reentrant honeycomb," *Mater. Des.*, 182, p. 108036.
- [154] Xiao, D., Dong, Z., Li, Y., Wu, W., and Fang, D., 2019, "Compression behavior of the graded metallic auxetic reentrant honeycomb: experiment and finite element analysis," *Mater Sci Eng A*, 758, pp. 163-171.
- [155] Choudhry, N. K., Panda, B., and Kumar, S., 2022, "In-plane energy absorption characteristics of a modified re-entrant auxetic structure fabricated via 3D printing," *Compos. B. Eng.*, 228, p. 109437.
- [156] Liu, H.-T., and Wang, L., 2022, "Design 3D improved star-shaped honeycomb with different tip angles from 2D analytical star-shaped model," *Compos Struct*, 283, p. 115154.
- [157] Zhang, X., Hao, H., Tian, R., Xue, Q., Guan, H., and Yang, X., 2022, "Quasi-static compression and dynamic crushing behaviors of novel hybrid re-entrant auxetic metamaterials with enhanced energy-absorption," *Compos Struct*, p. 115399.

- [158] Fan, H., Jin, F., and Fang, D., 2008, "Mechanical properties of hierarchical cellular materials. Part I: Analysis," *Compos Sci Technol*, 68(15-16), pp. 3380-3387.
- [159] Ajdari, A., Jahromi, B. H., Papadopoulos, J., Nayeb-Hashemi, H., and Vaziri, A., 2012, "Hierarchical honeycombs with tailorable properties," *Int J Solids Struct*, 49(11-12), pp. 1413-1419.
- [160] Taylor, C. M., Smith, C. W., Miller, W., and Evans, K., 2011, "The effects of hierarchy on the in-plane elastic properties of honeycombs," *International Journal of Solids and Structures*, 48(9), pp. 1330-1339.
- [161] Chen, Q., and Pugno, N. M., 2012, "In-plane elastic buckling of hierarchical honeycomb materials," *Eur J Mech A Solids*, 34, pp. 120-129.
- [162] Zhang, Y., Lu, M., Wang, C. H., Sun, G., and Li, G., 2016, "Out-of-plane crashworthiness of bio-inspired self-similar regular hierarchical honeycombs," *Compos Struct*, 144, pp. 1-13.
- [163] Fang, J., Sun, G., Qiu, N., Pang, T., Li, S., and Li, Q., 2018, "On hierarchical honeycombs under out-of-plane crushing," *Int J Solids Struct*, 135, pp. 1-13.
- [164] Yin, H., Huang, X., Scarpa, F., Wen, G., Chen, Y., and Zhang, C., 2018, "In-plane crashworthiness of bio-inspired hierarchical honeycombs," *Compos Struct*, 192, pp. 516-527.
- [165] Xu, X., Zhang, Y., Wang, J., Jiang, F., and Wang, C. H., 2018, "Crashworthiness design of novel hierarchical hexagonal columns," *Compos Struct*, 194, pp. 36-48.
- [166] Qiao, J., and Chen, C., 2016, "In-plane crushing of a hierarchical honeycomb," *International Journal of Solids and Structures*, 85, pp. 57-66.
- [167] Hou, J., Li, D., and Dong, L., 2018, "Mechanical behaviors of hierarchical cellular structures with negative Poisson's ratio," *J. Mater. Sci.*, 53(14), pp. 10209-10216.
- [168] Lv, W., Li, D., and Dong, L., 2020, "Study on mechanical properties of a hierarchical octet-truss structure," *Compos Struct*, 249, p. 112640.
- [169] Shen, J., Lu, G., and Ruan, D., 2010, "Compressive behaviour of closed-cell aluminium foams at high strain rates," *Composites Part B: Engineering*, 41(8), pp. 678-685.
- [170] Yuan, S., Chua, C. K., and Zhou, K. J. A. M. T., 2019, "3D - printed mechanical metamaterials with high energy absorption," *Adv Mater Technol*, 4(3), p. 1800419.

- [171] Yang, W., Yue, Z., and Xu, B., 2016, "A hybrid elastomeric foam-core/solid-shell spherical structure for enhanced energy absorption performance," *Int J Solids Struct*, 92, pp. 17-28.
- [172] Yang, W., Mao, S., Yang, J., Shang, T., Song, H., Mabon, J., Swiech, W., Vance, J. R., Yue, Z., and Dillon, S. J., 2016, "Large-deformation and high-strength amorphous porous carbon nanospheres," *Sci Rep*, 6(1), pp. 1-9.
- [173] Gibson, L. J., Ashby, M. F., and Harley, B. A., 2010, *Cellular materials in nature and medicine*, Cambridge University Press.
- [174] Bauer, J., Hengsbach, S., Tesari, I., Schwaiger, R., and Kraft, O., 2014, "High-strength cellular ceramic composites with 3D microarchitecture," *Proc Natl Acad Sci U.S.A.*, 111(7), pp. 2453-2458.
- [175] Hensleigh, R. M., Cui, H., Oakdale, J. S., Jianchao, C. Y., Campbell, P. G., Duoss, E. B., Spadaccini, C. M., Zheng, X., and Worsley, M. A., 2018, "Additive manufacturing of complex micro-architected graphene aerogels," *Mater Horiz*, 5(6), pp. 1035-1041.
- [176] Zhu, L., Li, N., and Childs, P., 2018, "Light-weighting in aerospace component and system design," *Propuls. Power Res.*, 7(2), pp. 103-119.
- [177] Farley, G. L., 1983, "Energy absorption of composite materials," *J. Compos. Mater.*, 17(3), pp. 267-279.
- [178] Teoh, S. H., 2004, *Engineering materials for biomedical applications*, World scientific.
- [179] Wang, C., Ma, S., Li, D., Zhao, J., Zhou, H., Wang, D., Zhou, D., Gan, T., Wang, D., and Liu, C., 2021, "3D Printing of Lightweight Polyimide Honeycombs with the High Specific Strength and Temperature Resistance," *ACS Appl. Mater. Interfaces*, 13(13), pp. 15690-15700.
- [180] Khan, M., Baig, T., and Mirza, S., 2012, "Experimental investigation of in-plane and out-of-plane crushing of aluminum honeycomb," *Mater. Sci. Eng. A*, 539, pp. 135-142.
- [181] Prawoto, Y., 2012, "Seeing auxetic materials from the mechanics point of view: a structural review on the negative Poisson's ratio," *Comput. Mater. Sci.*, 58, pp. 140-153.
- [182] Zhang, X.-c., Ding, H.-m., An, L.-q., and Wang, X.-l., 2015, "Numerical investigation on dynamic crushing behavior of auxetic honeycombs with various cell-wall angles," *Adv. Mech. Eng.*, 7(2), p. 679678.
- [183] Zhang, X., and Yang, D., 2016, "Mechanical properties of auxetic cellular material consisting

of re-entrant hexagonal honeycombs," *Materials*, 9(11), p. 900.

[184] Rafsanjani, A., Derome, D., Guyer, R. A., and Carmeliet, J., 2013, "Swelling of cellular solids: from conventional to re-entrant honeycombs," *Appl. Phys. Lett.*, 102(21), p. 211907.

[185] Hu, L., and Deng, H., 2015, "Indentation resistance of the re-entrant hexagonal honeycombs with negative poisson's ratio," *Mater. Res. Innov.*, 19(sup1), pp. S1-442-S441-445.

[186] Wu, X., Su, Y., and Shi, J., 2020, "In-plane impact resistance enhancement with a graded cell-wall angle design for auxetic metamaterials," *Compos. Struct.*, 247, p. 112451.

[187] Gu, L., Xu, Q., and Du, Z., 2021, "Analysis of tensile behaviour of hyperelastic auxetic cellular materials with re-entrant hexagonal cells," *J. Text. Inst.*, 112(2), pp. 173-186.

[188] Reznikov, N., Bilton, M., Lari, L., Stevens, M. M., and Kröger, R., 2018, "Fractal-like hierarchical organization of bone begins at the nanoscale," *Science*, 360(6388).

[189] Giorgio, I., Spagnuolo, M., Andraus, U., Scerrato, D., and Bersani, A. M., 2021, "In-depth gaze at the astonishing mechanical behavior of bone: A review for designing bio-inspired hierarchical metamaterials," *Math. Mech. Solids*, 26(7), pp. 1074-1103.

[190] Toumpanaki, E., Shah, D. U., and Eichhorn, S. J., 2021, "Beyond what meets the eye: Imaging and imagining wood mechanical–structural properties," *Adv. Mater.*, 33(28), p. 2001613.

[191] Barclift, M. W., and Williams, C. B., "Examining variability in the mechanical properties of parts manufactured via polyjet direct 3D printing," *Proc. International Solid Freeform Fabrication Symposium, University of Texas at Austin Austin, Texas*, pp. 6-8.

[192] Williams, J. C., and Starke Jr, E. A., 2003, "Progress in structural materials for aerospace systems," *Acta materialia*, 51(19), pp. 5775-5799.

[193] Sun, Y., and Li, Q., 2018, "Dynamic compressive behaviour of cellular materials: A review of phenomenon, mechanism and modelling," *Int. J. Impact Eng.*, 112, pp. 74-115.

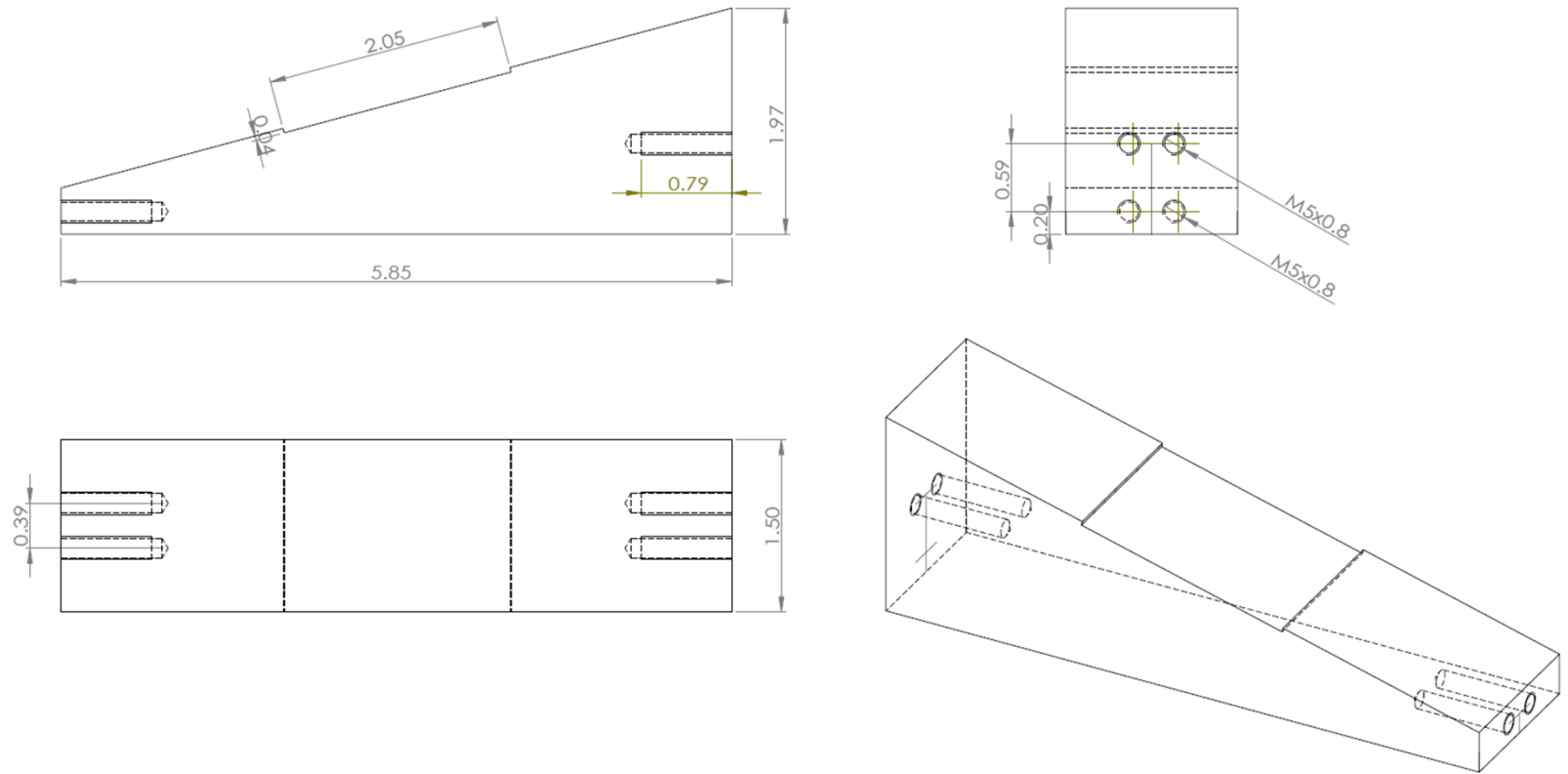
[194] Kader, M., Islam, M., Saadatfar, M., Hazell, P., Brown, A., Ahmed, S., and Escobedo, J., 2017, "Macro and micro collapse mechanisms of closed-cell aluminium foams during quasi-static compression," *Mater. Des.*, 118, pp. 11-21.

[195] Zou, Z., Reid, S., Tan, P., Li, S., and Harrigan, J., 2009, "Dynamic crushing of honeycombs and features of shock fronts," *Int. J. Impact Eng.*, 36(1), pp. 165-176.

- [196] Tan, P. J., Reid, S. R., Harrigan, J. J., Zou, Z., and Li, S., 2005, "Dynamic compressive strength properties of aluminium foams. Part I—experimental data and observations," *J. Mech. Phys. Solids.*, 53(10), pp. 2174-2205.
- [197] Hönl, A., and Stronge, W., 2002, "In-plane dynamic crushing of honeycomb. Part I: crush band initiation and wave trapping," *Int. J. Mech. Sci.*, 44(8), pp. 1665-1696.
- [198] Qiu, X., Zhang, J., and Yu, T., 2009, "Collapse of periodic planar lattices under uniaxial compression, part II: dynamic crushing based on finite element simulation," *Int. J. Impact Eng.*, 36(10-11), pp. 1231-1241.
- [199] Ashby, M. F., Evans, T., Fleck, N. A., Hutchinson, J., Wadley, H., and Gibson, L., 2000, *Metal foams: a design guide*, Elsevier.
- [200] Evans, K. E., and Alderson, K., 2000, "Auxetic materials: the positive side of being negative," *Engineering Science and Education Journal*, 9(4), pp. 148-154.
- [201] Li, M., He, B., Barbat, S., Gu, S., and Lu, W., "Rate Dependent Reinforcement of Liquid Nanofoam on Thin-Walled Tubes," *Proc. ASME International Mechanical Engineering Congress and Exposition*, American Society of Mechanical Engineers, p. V014T011A007.
- [202] Wang, Z., Shen, J., Lu, G., and Zhao, L., 2011, "Compressive behavior of closed-cell aluminum alloy foams at medium strain rates," *Mater. Sci. Eng. A*, 528(6), pp. 2326-2330.
- [203] Ganilova, O. A., and Low, J. J., 2018, "Application of smart honeycomb structures for automotive passive safety," *Proceedings of the Institution of Mechanical Engineers, Part D: Journal of Automobile Engineering*, 232(6), pp. 797-811.
- [204] Hassan, M., Scarpa, F., Ruzzene, M., and Mohammed, N., 2008, "Smart shape memory alloy chiral honeycomb," *Materials Science and Engineering: A*, 481, pp. 654-657.
- [205] Hazizan, M. A., and Cantwell, W., 2003, "The low velocity impact response of an aluminium honeycomb sandwich structure," *Composites Part B: Engineering*, 34(8), pp. 679-687.
- [206] Papka, S. D., and Kyriakides, S., 1998, "Experiments and full-scale numerical simulations of in-plane crushing of a honeycomb," *Acta materialia*, 46(8), pp. 2765-2776.
- [207] Sun, G., Li, S., Li, G., and Li, Q., 2018, "On crashing behaviors of aluminium/CFRP tubes subjected to axial and oblique loading: an experimental study," *Composites Part B: Engineering*, 145, pp. 47-56.

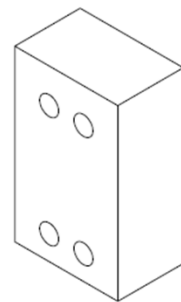
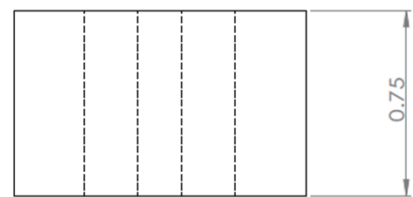
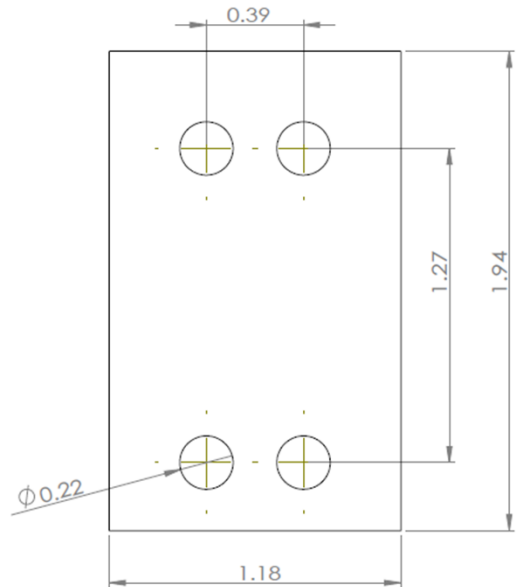
- [208] Reyes, A., Langseth, M., and Hopperstad, O. S., 2002, "Crashworthiness of aluminum extrusions subjected to oblique loading: experiments and numerical analyses," *International Journal of Mechanical Sciences*, 44(9), pp. 1965-1984.
- [209] Djamaluddin, F., Abdullah, S., Ariffin, A., and Nopiah, Z., 2015, "Optimization of foam-filled double circular tubes under axial and oblique impact loading conditions," *Thin-walled structures*, 87, pp. 1-11.
- [210] Hong, S.-T., Pan, J., Tyan, T., and Prasad, P., 2008, "Dynamic crush behaviors of aluminum honeycomb specimens under compression dominant inclined loads," *International Journal of Plasticity*, 24(1), pp. 89-117.
- [211] Wang, Z., Lu, Z., Yao, S., Zhang, Y., Hui, D., and Feo, L., 2016, "Deformation mode evolutionary mechanism of honeycomb structure when undergoing a shallow inclined load," *Composite Structures*, 147, pp. 211-219.
- [212] Zhu, G., Li, S., Sun, G., Li, G., and Li, Q., 2016, "On design of graded honeycomb filler and tubal wall thickness for multiple load cases," *Thin-Walled Structures*, 109, pp. 377-389.
- [213] Abayazid, F. F., Carpanen, D., and Ghajari, M., 2022, "New viscoelastic circular cell honeycombs for controlling shear and compressive responses in oblique impacts," *International Journal of Mechanical Sciences*, 222, p. 107262.
- [214] Zarei, H., and Kröger, M., 2008, "Optimum honeycomb filled crash absorber design," *Materials & Design*, 29(1), pp. 193-204.
- [215] Dhari, R. S., Javanbakht, Z., and Hall, W., 2021, "On the inclined static loading of honeycomb re-entrant auxetics," *Composite Structures*, 273, p. 114289.
- [216] Ma, F., Liang, H., Pu, Y., Wang, Q., and Zhao, Y., 2021, "Crashworthiness analysis and multi-objective optimization for honeycomb structures under oblique impact loading," *International Journal of Crashworthiness*, pp. 1-12.
- [217] Mirzaali, M., Caracciolo, A., Pahlavani, H., Janbaz, S., Vergani, L., and Zadpoor, A., 2018, "Multi-material 3D printed mechanical metamaterials: Rational design of elastic properties through spatial distribution of hard and soft phases," *Applied Physics Letters*, 113(24), p. 241903.

## APPENDIX



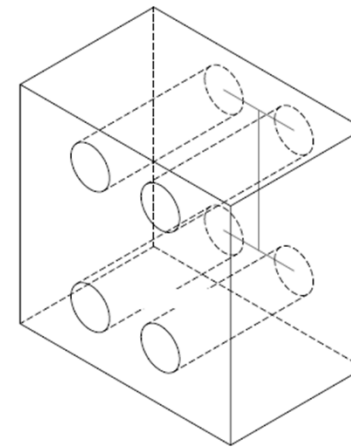
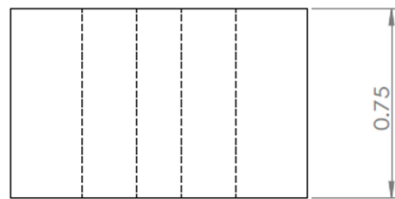
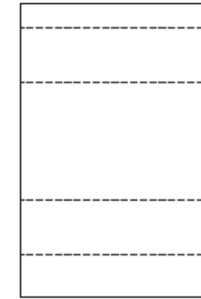
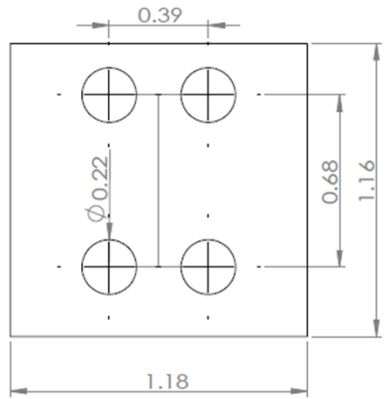
Michigan State University	15° Oblique Loading Wedge	Unit	Inch	Materials	Aluminum
Department of Civil & Environmental Engineering		Quantity	2	Designed by Chi Zhan	
Note: The threaded holes should be compatible with the testing machine.					

Figure A-1. 15° Wedge design for oblique loading tests.



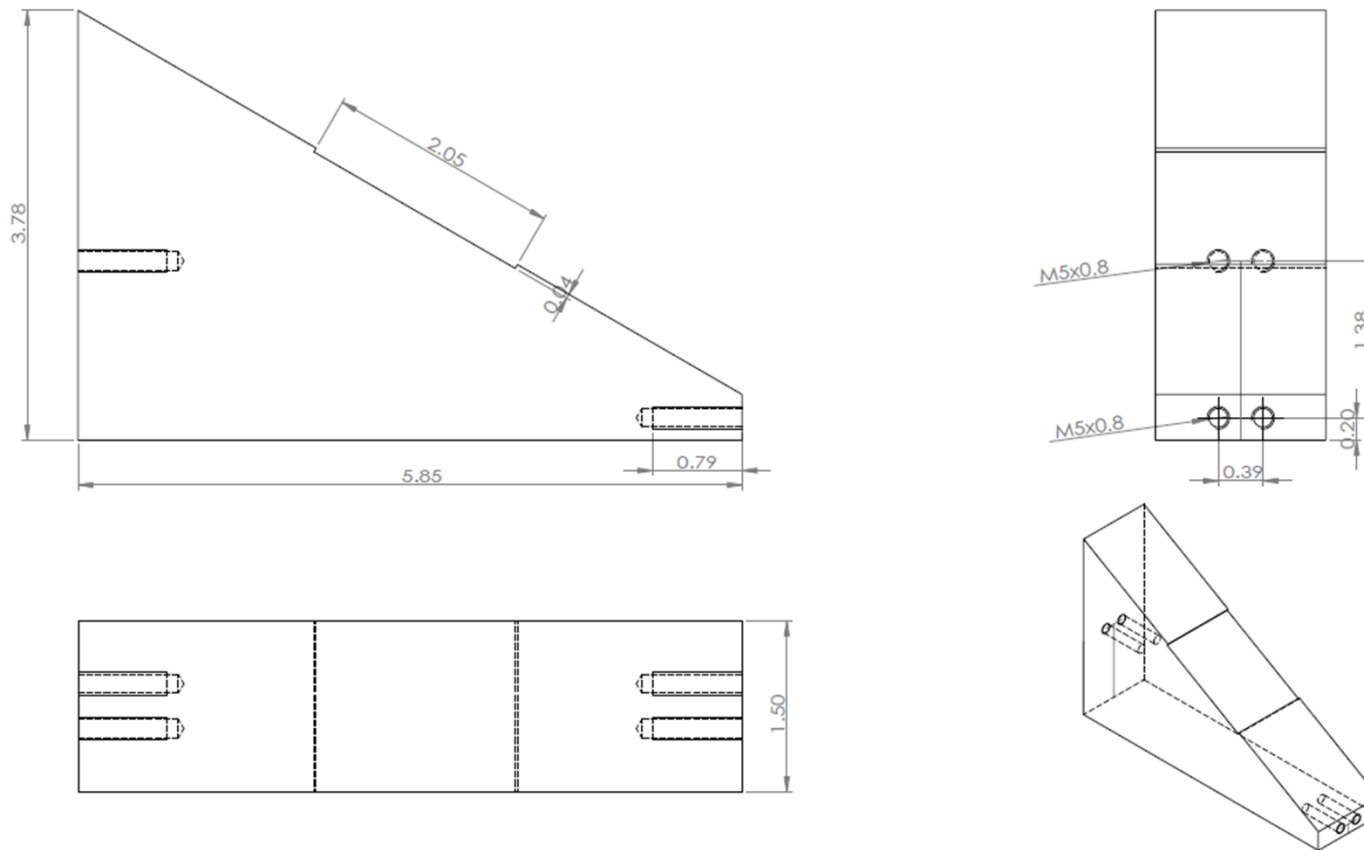
Michigan State University	15° Oblique Loading Wedge Long Cap	Unit	Inch	Materials	Aluminum
Department of Civil & Environmental Engineering		Quantity	4	Designed by Chi Zhan	
Note: The threaded holes should be compatible with the wedges and the testing machine.					

Figure A-2. Long cap design of the 15° wedge for oblique loading tests.



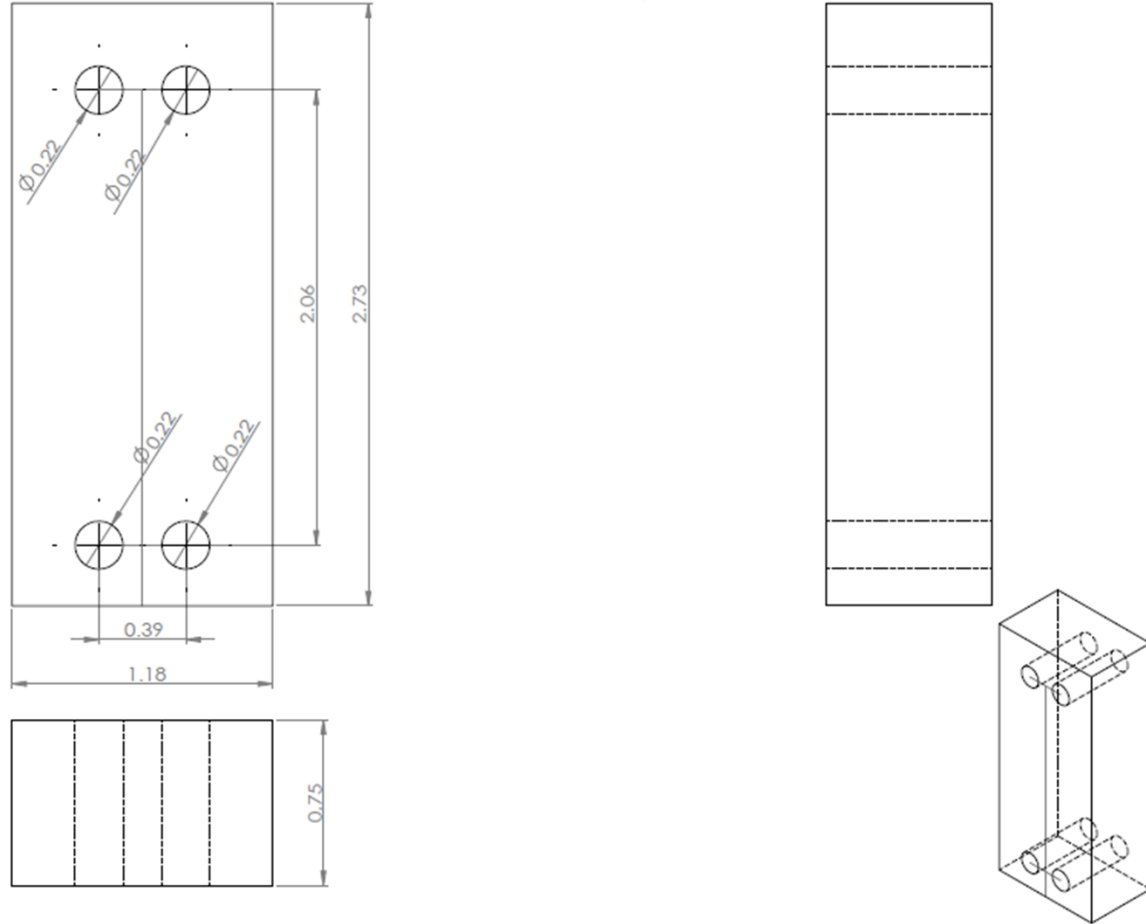
Michigan State University	15° Oblique Loading Wedge Short Cap	Unit	Inch	Materials	Aluminum
Department of Civil & Environmental Engineering		Quantity	4	Designed by Chi Zhan	
Note: The threaded holes should be compatible with the wedges and the testing machine.					

Figure A-3. Short cap design of the 15° wedge for oblique loading tests.



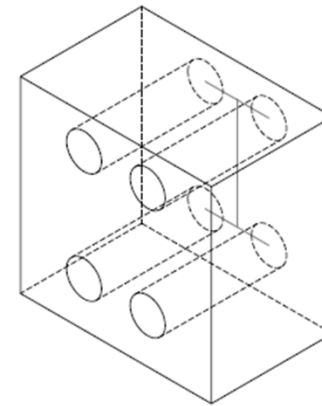
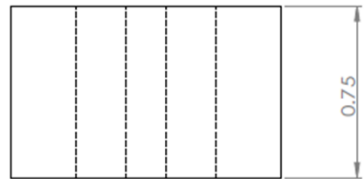
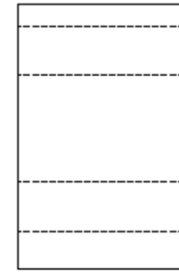
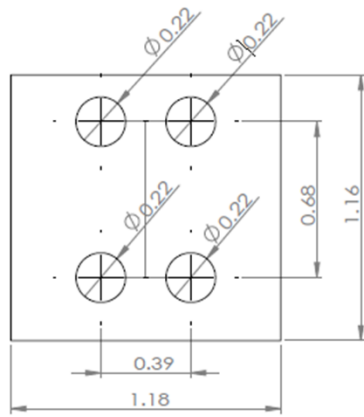
Michigan State University	30° Oblique Loading Wedge	Unit	Inch	Materials	Aluminum
Department of Civil & Environmental Engineering		Quantity	2	Designed by Chi Zhan	
Note: The threaded holes should be compatible with the testing machine.					

Figure A-4. 30° Wedge design for oblique loading tests.



Michigan State University	30° Oblique Loading Wedge Long Cap	Unit	Inch	Materials	Aluminum
Department of Civil & Environmental Engineering		Quantity	4	Designed by Chi Zhan	
Note: The threaded holes should be compatible with the wedges and the testing machine.					

Figure A-5. Long cap design of the 30° wedge for oblique loading tests.



Michigan State University	30° Oblique Loading Wedge Short Cap	Unit	Inch	Materials	Aluminum
Department of Civil & Environmental Engineering		Quantity	4	Designed by Chi Zhan	
Note: The threaded holes should be compatible with the wedges and the testing machine.					

Figure A-6. Short cap design of the 30° wedge for oblique loading tests.